

KAFKAS UNIVERSITY
GRADUATE SCHOOL OF SCIENCES
DEPARTMENT OF PHYSICS



MEASUREMENT OF THE DIFFERENTIAL INCLUSIVE JET CROSS
SECTION AT 7 TEV IN THE CMS DETECTOR

Özlem KAYA
DOCTOR OF PHILOSOPHY THESIS

SUPERVISOR
Prof. Dr. Mevlüt KARABULUT
COSUPERVISOR
Asst. Prof. Mikko VOUTILAINEN

September - 2015
KARS

The undersigned hereby certify that they have read and recommend to the Faculty of Physics Science for acceptance a thesis entitled MEASUREMENT OF THE DIFFERENTIAL INCLUSIVE JET CROSS SECTION AT 7 TEV IN THE CMS DETECTOR by Ozlem KAYA in partial fulfillment of the requirements for the degree of PhD of Physics Science.

Dated: September, 2015

Research Supervisor:

Prof. Dr. Mevlüt KARABULUT

Research CoSupervisor:

Asst. Prof. Mikko VOUTILAINEN

Examining Committee:

Prof. Dr. Erhan GÜLMEZ

Prof. Dr. İsmail ÇAKMAK

Prof. Dr. Mithat KAYA

Asst. Prof. Gülçin CENGİZ

Acceptance of this thesis has been confirmed by the committee of the Institute of Science at the date/....../2015 and/..... numbered decision.

Institutional Representative:

Prof. Dr. Hidayet Metin ERDOĞAN

ACKNOWLEDGEMENTS

This thesis is the end result of my participation in QCD group at Cern in Switzerland. First of all, I would like to express my gratitude to my group at Cern. I specially would like to thank Dr. Konstantinos Kousouris who lead me through whole my analysis. I also would like to thank our finding agency Turkish Atomic Energy Agency (TAEK) for their continues supports.

Surely to my colleagues at Department of Physics, Kafkas University in Kars, Turkey. I wish to thank Prof. Dr. Mevlüt Karabulut, the head of our department, for encouraging my work at Cern with the assignments and also for reviewing the final version of this thesis.

And my dear colleagues, more precisely my friends, I feel so fortunate to have you. I know that I, from time to time, hindered my responsibilities at the department due to my assignments at Cern, so I want to thank you all for all the work that you did there during my absence.

I am pleased to extend my gratitude to Prof. Dr. Erhan Gülmez at Physics Department, Boğaziçi University in Istanbul, Turkey, as he has always supported my research at Cern both financially and intellectually through a series of research grants and his insightful ideas, feedback and emotional support.

I also would like to thank my dad who is always with me in spirit to light my lifes path, and my mom and my sister, no matter how far they are in distance, they remain close to me at heart.

My deepest appreciation, certainly goes to my supervisors; Dr. Mikko Voutilainen who has shown endless kindness and patience with me during the completion of this thesis and doing research, gracefully and always given much appreciated advice which helped me clarify my vision for this thesis. He made this dissertation possible by helping me unconditionally in all matters. He has continuously impressed and inspired me with his practicality, knowledge and supervision.

At both personal and academic level, Mithat Kaya, my dear husband, I am particularly grateful to you for being so caring and generous with your never-ending support. You have been with me every step of the way, in good and bad times, especially at times when I completely get lost. I know it for sure, more than me, today, you are the happiest person as I could complete my doctoral thesis.

Finally, I wish to thank my daughter, Nisan Su, for being the brightest light in my life ever simply with her presence: always enthusiastic about life and always alive. Canım kızım, thanks to your support and understanding, I could manage to finish this thesis. I have no idea how it feels for you to go through this period with me and, at this very early age, to know what it means to write a PhD thesis. During this stressful process, I know I stole a lot from the time I could spend for you and I apologize for this. I wish you could be here today at my defense, to share my success and happiness since you deserve it more than I do. Which is why I dedicate this thesis to you, my one and only beloved daughter.

TABLE OF CONTENTS

ACKNOWLEDGEMENTS	iii
LIST OF TABLES	vii
LIST OF FIGURES	viii
LIST OF ABBREVIATIONS	xiv
ABSTRACT	xviii
ÖZET	xix
Chapter 1 INTRODUCTION	1
Chapter 2 THE DETECTOR SYSTEM	3
2.1 LEP-LHC Machine	3
2.2 The CMS Detector	4
2.2.1 Superconducting Magnet	8
2.2.2 Inner Tracking System	8
2.2.3 Electromagnetic Calorimeter (ECAL)	10
2.2.4 Hadron Calorimeter (HCAL)	12
2.2.4.1 Hadronic Barrel (HB)	13
2.2.4.2 Hadronic Endcap, (HE)	14
2.2.4.3 Hadronic Outer (HO)	16
2.2.4.4 Forward Hadron Calorimeter (HF)	17
2.2.5 Muon Detector System	19
2.2.5.1 Drift Tubes (DT)	19
2.2.5.2 Cathode Strip Chambers (CSC)	21
2.2.5.3 Resistive Plate Chambers (RPC)	21
Chapter 3 THEORY	23

3.1	Standard Model	23
3.1.1	Fundamental Interactions and Forces	25
3.1.2	Fundamental Particles	27
3.2	Quantum Chromodynamics QCD	29
3.2.1	Perturbative Quantum Chromodynamics pQCD	30
3.2.2	Numerical Measurements of NLO	32
3.3	Non-Perturbative QCD (NP)	32
3.3.1	Hadronization	33
3.3.2	Multiple Parton Interaction, (MPI)	33
3.3.3	Non-Perturbative Corrections	34
3.4	Theoretical Uncertainty Correlations	35
Chapter 4	JET RECONSTRUCTION	37
4.1	Jet Clustering Algorithm	38
4.2	Particle Flow Jets (PFJets)	42
4.3	Jet Energy Correction in The CMS Detector	47
4.3.1	Offset Correction	48
4.3.2	Relative Correction	49
4.3.3	Absolute Correction	49
4.4	Jet Energy Resolution (JER)	50
Chapter 5	DATA ANALYSIS	52
5.1	Trigger Selection	52
5.2	Event Selection	54
5.2.1	Missing Energy	54
5.2.2	Vertex Quality Cut	56
5.2.3	Good Run Selection	60
5.3	Jet Identification	63
5.3.1	Jet Identification (Jet ID) Efficiency	72
5.3.2	Normalized Rate	73
5.4	Cross Section Normalization by Luminosity	77
5.5	Cross Section Unfolding	79
5.6	Systematic Uncertainties	87
5.6.1	Jet Energy Scale Uncertainty	87
5.6.2	Unfolding Uncertainty	89
5.6.3	Luminosity Uncertainty	90
5.6.4	Other Uncertainties	90
5.6.5	Experimental Uncertainty Correlations	91
Chapter 6	RESULTS AND CONCLUSIONS	93
Bibliography	96

LIST OF TABLES

3.1	The forces and interactions.	26
3.2	Example of baryons.	28
3.3	Example of mesons.	28
5.1	The integrated luminosity for each trigger paths.	52
5.2	HLT jet triggers and corresponding L1SingleJet trigger for the 2011 data sets.	52
5.3	HLT jet trigger thresholds.	53

LIST OF FIGURES

2.1	CMS detector structure and coordinate system.	6
2.2	Representation of CMS and its different parts: the silicon tracker (blue), the electromagnetic calorimeter (green-blue), the hadronic calorimeter (orange), the magnet (purple), and the muon chambers (white)[11].	7
2.3	CMS integrated luminosity at 7 TeV in 2011.	7
2.4	Superconducting magnet.	8
2.5	Pixel modules (left), barrel pixel (middle), forward pixel (right).	9
2.6	The pixel detectors[13].	10
2.7	PbWO ₄ crystals. Upper face is unpolished barrel crystal with its two APDs (left). Polished an endcap crystal attached with VPT (right).	11
2.8	ECAL layout showing location of the crystals and modules (left). Front view of ECAL barrel super module equipped with crystals (right).	11
2.9	Endcap dee equipped with a 5x5 supercrystals.	12
2.10	Longitudinal view of the CMS detector showing the locations of the HB, HE, HO and HF calorimeters (left). HCAL tower segmentation in the r,z plane (right). 1/4 of the HB, HE, and HO detector towers shown.	13
2.11	Assembled HCAL half-barrel in SX5, the under ground assembly hall (left). Pictures of 20° HB wedges (middle) and each wedge is segmented into four azimuthal angle ($\Delta\phi=50^\circ$) (right).	14
2.12	Installation of a central megatile.	14

2.13	Wave length shift fiber is placed in a groove in each scintillator tile (leftmost). ODU (second from the left). 16 fibers from each layer (HB), (second from the right). Fibers on HPD face. 19 pixel HPD (16 η + 2 depths) (rightmost).	15
2.14	A half barrel is made of 18 wedges each subtending 20° in azimuth ϕ (left) and corresponding towers (middle). Located in the CMS detector (right).	15
2.15	A diagram of a quarter section of the CMS showing location of HO (left). An HO scintillator tile with embedded wavelength shifting fibers. The tile size is chosen to match projective towers in the HB (right).	17
2.16	Fiber view and ROBOX of HF wedges.	18
2.17	Fiber view of HF wedges.	18
2.18	Completed HF.	19
2.19	Muon track in the muon chambers.	20
2.20	Drift chambers in the CMS.	20
2.21	Cathod strip chambers in the CMS.	21
2.22	Resistive plate chambers in CMS.	22
3.1	Fundamental particles of the standard model.	24
3.2	Residual strong force binding the nucleons.	26
3.3	Free neutron decays to proton via mediator W boson.	26
3.4	The bosons, fermions and hadrons.	27
3.5	The visualization of the Feynman diagram for hadron collions.	31
3.6	NP correction factor from PYTHIA6 (tune Z2) and HERWIG++ 2.4.2 for different rapidity region.	34
3.7	The theoretical uncertainties on theoretical inclusive jet p_T cross section measurements in five rapidity region for NNPDF2.1 PDF set.	36
4.1	Jet production at the p-p collision.	38
4.2	Collinear safety (left two shapes) and infrared safety (right three shapes) algorithms.	39

4.3	Distribution of the component fraction for JetHLT60 trigger with threshold $p_T > 114$ GeV in five eta region between DATA and MC inclusive PF_{jet}	44
4.4	Distribution of the component fraction for JetHLT110 trigger with threshold $p_T > 196$ GeV.	44
4.5	Distribution of the component fraction for JetHLT190 trigger with threshold $p_T > 300$ GeV.	45
4.6	Distribution of the component fraction for JetHLT240 trigger with threshold $p_T > 362$ GeV.	45
4.7	Distribution of the component fraction for JetHLT370 trigger with threshold $p_T > 507$ GeV.	46
4.8	The illustration of the factorized jet energy corrections steps in the CMS detector. The jet energy correction factors are applied into reconstructed jets to obtain calibrated jets.	48
4.9	PF jet p_T resolution in $ \eta < 0.5$ [55].	51
5.1	HLT single jet trigger efficiency.	53
5.2	Distribution of $\cancel{E}_T/\Sigma E_T$ for both the data and MC simulations with leading Jet $p_T > 510$ GeV. Red points represent data events and filled area with camel color represents the MC simulation events.	55
5.3	Average energy fraction vs number of vertex for JetHLT60 trigger for different rapidity bin region for $p_T > 114$ GeV in five η region. The red full circles represent charge hadron fraction, blue full squares represent neutral hadron fractions, and green full triangles represent photon hadronic fractions distributions.	57
5.4	Average energy fraction vs number of vertex for JetHLT110 trigger for different rapidity bin regions for $p_T > 196$ GeV.	57
5.5	Average energy fraction vs number of vertex for JetHLT190 trigger for different rapidity bin regions for $p_T > 300$ GeV.	58
5.6	Average energy fraction vs number of vertex for JetHLT240 trigger for different rapidity bin regions for $p_T > 362$ GeV.	58
5.7	Average energy fraction vs number of vertex for JetHLT370 trigger for different rapidity bin regions for $p_T > 507$ GeV.	59

5.8	Distribution of the jet component fractions versus run numbers for JetHLT60 trigger with threshold $p_T > 114$ GeV in five rapidity bins. Here the red circles, green triangle and, blue square represent charged hadronic fraction, photon fraction and, neutral hadronic fraction respectively.	60
5.9	Distribution of the jet component fractions versus run numbers for JetHLT110 trigger with threshold $p_T > 196$ GeV in five rapidity bins.	61
5.10	Distribution of the jet component fractions versus run numbers for JetHLT190 trigger with threshold $p_T > 300$ GeV in five rapidity bins.	61
5.11	Distribution of the jet component fractions versus run numbers for JetHLT240 trigger with threshold $p_T > 362$ GeV in five rapidity bins.	62
5.12	Distribution of the jet component fractions versus run numbers for JetHLT370 trigger with threshold $p_T > 507$ GeV in five rapidity bins.	62
5.13	Comparison of the charged hadron energy fraction for JetHLT60 trigger with threshold $p_T > 114$ GeV in five rapidity bins between DATA and MC inclusive jet events. Red points represent data events and filled area with camel color represents the MC simulation events.	64
5.14	Comparison of the charged hadron energy fraction for JetHLT110 trigger with threshold $p_T > 196$ GeV in five rapidity bins between DATA and MC inclusive jet events.	65
5.15	Comparison of the charged hadron energy fraction for JetHLT190 trigger with threshold $p_T > 300$ GeV in five rapidity bins between DATA and MC inclusive jet events.	65
5.16	Comparison of the charged hadron energy fraction for JetHLT240 trigger with threshold $p_T > 362$ GeV in five rapidity bins between DATA and MC inclusive jet events.	66
5.17	Comparison of the charged hadron energy fraction for JetHLT370 trigger with threshold $p_T > 507$ GeV in five rapidity bins between DATA and MC inclusive jet events.	66
5.18	Comparison of the neutral hadron energy fraction for JetHLT60 trigger with threshold $p_T > 114$ GeV in five rapidity bins between DATA and MC inclusive jet events.	67

5.19	Comparison of the neutral hadron energy fraction for JetHLT110 trigger with threshold $p_T > 196$ GeV in five rapidity bins between DATA and MC inclusive jet events.	67
5.20	Comparison of the neutral hadron energy fraction for JetHLT190 trigger with threshold $p_T > 300$ GeV in five rapidity bins between DATA and MC inclusive jet events.	68
5.21	Comparison of the neutral hadron energy fraction for JetHLT240 trigger with threshold $p_T > 362$ GeV in five rapidity bins between DATA and MC inclusive jet events.	68
5.22	Comparison of the neutral hadron energy fraction for JetHLT370 trigger with threshold $p_T > 507$ GeV in five rapidity bins between DATA and MC inclusive jet events.	69
5.23	Comparison of the neutral electromagnetic (photon) energy fraction for JetHLT60 trigger with threshold $p_T > 114$ GeV in five rapidity bins between DATA and MC inclusive jet events. . . .	69
5.24	Comparison of the neutral electromagnetic (photon) energy fraction for JetHLT110 trigger with threshold $p_T > 196$ GeV in five rapidity bins between DATA and MC inclusive jet events. . . .	70
5.25	Comparison of the neutral electromagnetic (photon) energy fraction for JetHLT190 trigger with threshold $p_T > 300$ GeV in five rapidity bins between DATA and MC inclusive jet events. . . .	70
5.26	Comparison of the neutral electromagnetic (photon) energy fraction for JetHLT240 trigger with threshold $p_T > 362$ GeV in five rapidity bins between DATA and MC inclusive jet events. . . .	71
5.27	Comparison of the neutral electromagnetic (photon) energy fraction for JetHLT370 trigger with threshold $p_T > 507$ GeV in five rapidity bins between DATA and MC inclusive jet events. . . .	71
5.28	The distribution of the jet ID efficiency versus probe jet p_T in five rapidity regions. Each color represents different trigger range with different p_T threshold.	72
5.29	The normalized rate distribution of JetHLT60 trigger jet p_T for five rapidity regions.	74
5.30	The normalized rate distribution of JetHLT110 trigger jet p_T for five rapidity regions.	75
5.31	The normalized rate distribution of JetHLT190 trigger jet p_T for five rapidity regions.	75

5.32	The normalized rate distribution of JetHLT240 trigger jet p_T for five rapidity regions.	76
5.33	The normalized rate distribution of JetHLT370 trigger jet p_T for five rapidity regions.	76
5.34	The distribution of the jet p_T yields vs number of events for five rapidity regions. Each color represents different trigger range with different p_T threshold.	77
5.35	The spectrum construction from individual trigger paths for inclusive jet p_T spectrum in five rapidity regions[46].	78
5.36	The Bayes's response matrices for inclusive jet p_T in five rapidity region.	82
5.37	Different unfolding measurements calculated by using RooUnfoldPackage in five rapidity regions.	85
5.38	The ratio of the unfolding measurements to forward smearing in five rapidity regions.	86
5.39	The JES uncertainties on inclusive jet p_T measurement in five rapidity regions.	88
5.40	Unfolding uncertainty effect on jet p_T resolution.	89
5.41	Unfolding uncertainty effect on the inclusive jet p_T spectrum.	90
5.42	The Experimental uncertainties on inclusive jet p_T	92
6.1	The comparison of the double differential inclusive jet p_T cross section measurements with theoretical prediction in five rapidity regions at 7 TeV. The left side represents inclusive jet cross section with anti- $k_T = 0.7$ cone size for approximately 5 fb^{-1} luminosity while the right side represents inclusive jet cross section with anti- $k_T = 0.5$ cone size for 34 pb^{-1} luminosity from previous results.	94
6.2	Comparison of inclusive jet p_T cross section measurements to theory for different PDF sets in five rapidity region.	95

LIST OF ABBREVIATIONS

ALICE	A Large Ion Collider Experiment
APDs	Avalanche PhotoDiodes
ATLAS	A Toroidal LHC ApparatuS
CALOJets	CALOrimetric Jets
CHF	Charge Hadron Fraction
CMS	Compact Muon Solenoid
CMSSW	Compact Muon Solenoid SoftWare
CSC	Cathode Strip Chambers
DT	Drift Tubes
ECAL	Electromagnetic CALorimeter
EM	ElectroMagnetic
E_{miss}	Missing Energy
E_T	Transverse Energy
EWT	ElectroWeak Theory
GeV	Giga electron Volt
HAD	HADronic
HCAL	Hadronic CALorimeter

HE	Hadronic Endcap
HF	Hadronic Forward
HLT	High Level Trigger
HO	Hadronic Outer
HPD	Hybrid PhotoDiode
IP	Interaction Point
IRC	Collinear Safety Cone
IRS	InfraRed Safe
JEC	Jet Energy Calibration
JER	Jet Energy Resolution
Jet ID	Jet IDentification
JPTJets	Jet Plus Tracks Jets
L1	Level-1 trigger
LED	Light Emitting Diode
LEP	Large Electron Positron Collider
LHC	Large Hadron Collider
LHCb	Large Hadron Collider beauty
LO	Leading Order
MC	MonteCarlo
MPF	Missing transverse energy Projection Fraction
MPI	Multiple Parton Interaction
NEF	Neutral Electromagnetic Fraction

NHF	Neutral Hadron Fraction
NLO	Next to Leading Order
NNLO	Next-Next to Leading Order
NP	Non Perturbative
ODU	Optical Decoding Unit
PbWO4	Lead Tungstate
PDF	Parton Distribution Function
PFJets	Particle Flow Jets
PMT	Photo Multiplier Tube
pQCD	perturbative Quantum Chromo Dynamics
PV	Primary Vertex
QCD	Quantum Chromo Dynamics
QED	Quantum Electro Dynamic
RMS	Root Mean Square
ROBOX	ReadOut BOXes
ROCs	Read Out Chips
RPC	Resistive Plate Chambers
SCs	Super Crystals
SISCone	Seedless Infrared-Safe Cone
SM	Standard Model
SUSY	SUper SYmmetry
SVD	Singular Value Decomposition

TeV	Tera electron Volt
TOTEM	TOTAL Elastic and diffractive cross section Measurement
VPTs	Vacuum PhotoTriodes
WLS	WaveLength Shifting fibers



ABSTRACT

In this thesis, measurement of inclusive jet cross section is presented. Data from LHC proton-proton collisions at $\sqrt{s}=7$ TeV, corresponding to approximately 5.0 fb^{-1} of integrated luminosity, have been collected by the CMS detector. Particle Flow jets with cone radius parameter $R = 0.7$ are reconstructed up to rapidity bin 2.5 and transverse momentum 2000 GeV using the anti- k_T clustering algorithm. The measured cross sections are corrected for detector effects and compared to perturbative QCD predictions at next-to-leading order, using five sets of parton distribution functions corrected by non-perturbative effects. Measured inclusive jet cross sections and theoretical predictions are shown to be in a good agreement. We also measured the cross sections with cone size 0.7 in 2011 and compared the data with the cross sections data with cone size 0.5 collected in 2010. We found that the spectra are in good agreement despite the differences in their radii and jet energy scale uncertainties.

2015, 101 pages

Key Words: LHC, CMS, QCD, Jet, Inclusive Jet Cross Section

ÖZET

Bu tezde kapsamlı jet tesir kesiti ölçümü sunuldu. 2011 yılı boyunca, Büyük Hadron Çarpıştırıcısı'nda yaklaşık toplam 5.0 fb^{-1} ışıklılığa karşılık gelen $\sqrt{s}= 7 \text{ TeV}$ enerjili proton-proton çarpışmalarından gelen veriler, CMS dedektörü tarafından toplandı. $R=0.7$ koni yarıçapına sahip parçacık akısı jetleri, anti- k_T algoritması kullanılarak rapiditi 2.5 ve momentum 2000 GeV' ye kadar yeniden yapılandırıldı. Ölçülen tesir kesitleri üzerindeki dedektör etkisi düzeltilerek, non-perturbative faktör ile düzeltilen beş farklı parton dağılım fonksiyonu seti kullanılarak next-to-leading order seviyesinde perturbative QCD öngörülleri ile karşılaştırıldı. Ölçülen kapsamlı jet tesir kesitlerinin teorik öngörülerle uyum içinde oldukları gösterildi. Ayrıca 2011 yılında 0.7 koni yarıçapı ile ölçülen tesir kesiti, 2010 yılında toplanmış ve koni yarıçapı 0.5 olan ölçümler ile karşılaştırıldı. Farklı jet yarıçaplarına ve farklı jet enerji skalası belirsizliklerine sahip olmalarına rağmen, her iki spektrumun birbirleri ile uyum içinde oldukları bulundu.

2015, 101 sayfa

Anahtar Kelimeler: LHC, CMS, QCD, Jet, Kapsamlı Jet Tesir Kesiti

1. INTRODUCTION

Compact Muon Solenoid (CMS) is the one of the biggest experiment located on the Large Hadron Collider (LHC) in CERN. it has been collecting data since 2008 to study physics. CMS uses a world wide grid computer structure to store its data and to let users to analyze them over this computers. CMS detector is designed a cylindrical shape that use cylindrical coordinate system to trace the particles. It has a 4 Tesla Magnetic field solenoid magnet that covers the tracker, pixels and calorimeter system. Muon detector systems divided in three pieces are located at the far side of the CMS experiment.

In this thesis inclusive jet cross section was measured using 2011 data set from the CMS. Total integrated luminosity was around 5.0 fb^{-1} which was almost 2 orders of magnitude larger than the published LHC results from the 2010 run[1, 2, 3]. The jets that have high transverse momentum from the proton-proton collisions are defined by the Quantum Chromodynamics (QCD) in terms of parton-parton scattering that produces a hadronic jets. Double differential inclusive jet ($p+p \rightarrow \text{jet}+X$) cross-section as a function of jet p_T was measured at the $\sqrt{s} = 7 \text{ TeV}$ from the proton-proton collision. This cross section will exploit to test the predictions of perturbative QCD, constrain parton distribution functions (PDFs) of the proton, differentiate among PDF sets, and look for possible deviations from the standard model. Jets are reconstructed up to rapidity bin 2.5, and transverse momentum 2000 GeV. The measured cross sections are corrected for detector effects and compared to the next-to-leading-order QCD predictions.

LHC and CMS experiments are explained in chapter 2. The Theory, Standard Model

is given in chapter 3. Jet Reconstructions are discussed in chapter 4. Data Analysis, Results and Conclusions are given by chapter 5 and 6, respectively.



2. THE DETECTOR SYSTEM

2.1 LEP-LHC Machine

Current LHC tunnel was originally built for LEP (Large Electron Positron) experiment during the 1984-1989[4]. It was started in 1989 and completed in 2000. During this period CERN council and non-member states negotiated to construct a new machine with a center of mass energy of 14 TeV. Eventually in December 1996 the CERN Council approved construction of the 14 TeV machine in a single stage. LHC machine is located between French and Swiss borders 100 m under the ground with a 26.7 km circumference. In the LHC tunnel there are five experimental halls dedicated for CMS[5], ATLAS[6], LHCb[7], TOTEM[8] and ALICE[9] experiments. CMS and ATLAS experiments are high luminosity experiments with a goal of reaching a peak luminosity of $L= 10^{34}\text{cm}^2\text{s}^{-1}$ for proton-proton collisions. LHCb mainly concentrates on B physics, aiming at a peak luminosity of $L= 10^{32}\text{cm}^2\text{s}^{-1}$. TOTEM experiment aiming at a peak luminosity of $L= 10^{29}\text{cm}^2\text{s}^{-1}$ with 156 bunches and it mainly concentrates on measuring total cross section, elastic scattering and diffractive processes. Besides proton-proton beam, in LHC, the heavy ion beam is used for a new physics as well. ALICE experiment is the heavy ion experiment which aims at a peak luminosity of $L= 10^{27}\text{cm}^2\text{s}^{-1}$ for nominal lead-lead ion beam collisions.

The number of events generated from LHC machine is given by Eq. (2.1).

$$N_{\text{event}} = L\sigma_{\text{event}} \quad (2.1)$$

where L is the machine luminosity, σ_{event} is the cross section for the event. Luminosity

depends on the beam parameters which is given by Eq. (2.2).

$$L = \frac{N_b^2 n_b f_{\text{rev}} \gamma_r}{4\pi \epsilon_n \beta^*} F \quad (2.2)$$

where N_b is the number of particles per bunch, n_b the number of bunches per beam, f_{rev} the revolution frequency, γ_r the relativistic gamma factor, ϵ_n the normalized transverse beam emittance, β^* the beta function at the collision point, and F the geometric luminosity reduction factor due to the crossing angle at the interaction point (IP) by Eq. (3.1).

$$F = \left(1 + \left(\frac{\theta_c \sigma_z}{2\sigma^*} \right)^2 \right)^{-1/2} \quad (2.3)$$

where θ_c is the full crossing angle at the interaction point, σ_z the RMS bunch length, and σ^* the transverse RMS beam size at the IP.

Proton-proton collider beam requires opposite magnetic dipole fields in both rings. Therefore LHC is designed to use separate magnetic fields and vacuum chambers in the main arcs and with common sections only at the insertion regions where the experimental detectors are located. It uses superconducting magnet technology that reaches 8.33 T dipole magnetic field at 7 TeV energy[10].

2.2 The CMS Detector

The CMS is the one of the biggest experiments located on the LHC beam line. Its location is on the Cessy, French side. It is a cylindrical shape that consists of many layers of different detectors to detect different type of particles. The biggest solenoid magnet ever built is located at the heart of the CMS to measure the momentum of the charged particles. The CMS is aiming to search for new physics such as origin of mass, unification of the fundamental forces, beyond the standard model, super symmetry, black holes, dark energy, gravitational field and so on. In order to discover new

physics CMS uses several different types of detector systems. The CMS collaboration accomplished to build such a huge detector to push the limits of both the electronics and measurement speed that are very important to measure particles coming from the proton-proton collision.

The CMS detector system is designed to search wide range of physics such as higgs boson, supersymmetric particles, new massive vector bosons, extra dimensions, heavy-ion physics and many more. The detector requirements for the CMS to achieve physics program are following:

- Good muon identification and momentum resolution over a wide range of momenta and angles, good dimuon mass resolution (1% at 100 GeV), and the ability to determine unambiguously the charge of muons with $p < 1$ TeV;
- Good charged-particle momentum resolution and reconstruction efficiency in the inner tracker. Efficient triggering and offline tagging of τ s and b-jets, requiring pixel detectors close to the interaction region;
- Good electromagnetic energy resolution, good diphoton and dielectron mass resolution (1% at 100GeV), wide geometric coverage, π^0 rejection, and efficient photon and lepton isolation at high luminosities;
- Good missing-transverse-energy and dijet-mass resolution, requiring hadron calorimeters with a large hermetic geometric coverage and with fine lateral segmentation.

The CMS detector design fulfills above conditions as described below. The milestone feature of the CMS is to have the high field solenoid magnet, full silicon based inner tracking system, and a homogenous scintillating crystal based electromagnetic calorimeter.

CMS uses cylindrical coordinate system in terms of (θ, ϕ, z) . The origin is located at the interaction point inside the experiment. z-axis lays along the beam direction, y-axis pointing vertically upward, and x-axis pointing horizontally towards the center of LHC. z, y and x-axis are orthogonal to each other. The azimuthal angle ϕ is measured from the x axis in the x-y plane and the radial coordinate in this plane is denoted by r. The polar angle θ is measured from the z-axis. Pseudorapidity is defined as

$\eta = -\ln \tan(\theta/2)$ and the rapidity is defined as $y = \frac{1}{2} \ln \frac{E+p_z}{E-p_z}$. Thus, the momentum and energy transverse to the beam direction, denoted by p_T and E_T , respectively, are computed from the x and y components. The imbalance of energy measured in the transverse plane is denoted by E_{miss} . Coordinate systems and CMS detector structure are given in Fig. 2.1 and 2.2.

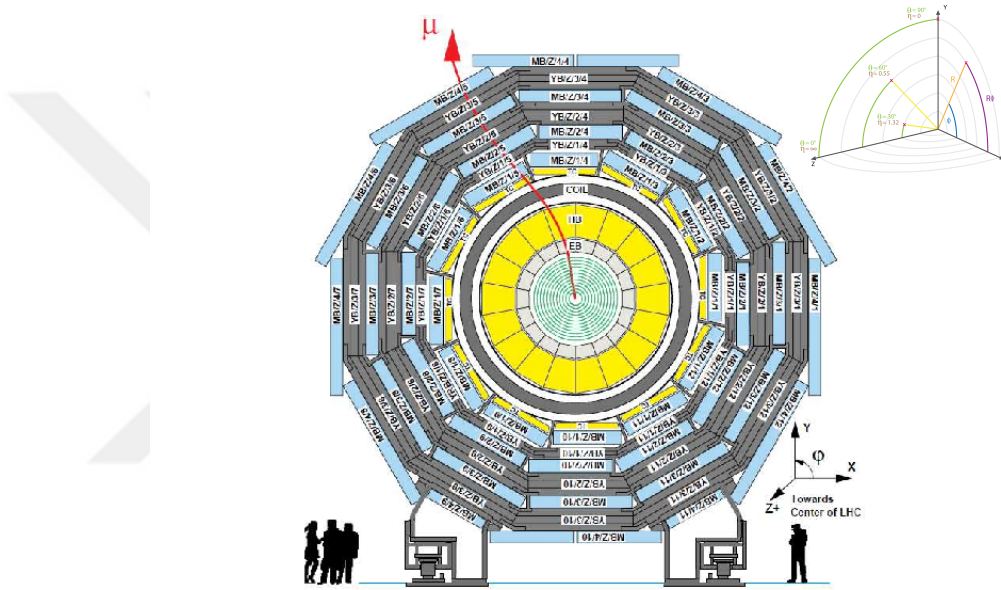


Figure 2.1: CMS detector structure and coordinate system.

The overall dimensions of the CMS detector are a length of 21.6 m, a diameter of 14.6 m and a total weight of 12500 tons. The thickness of the detector in radiation lengths is greater than $25 X_0$ for the ECAL, and the thickness in interaction lengths varies from $7-11 \lambda_I$ for HCAL depending on η [12].

More than 90 percent of the CMS detector system is completed and lowered to the underground in 2008. In 2009 rest of the detector is finished and lowered. The whole system was ready for the October 2009 beam collision. At the beginning, the CMS was collecting data from the cosmic particles, mostly muons, this data were used mostly for the background study and detector calibration. Since 2009, LHC increased its luminosity and center of mass collision energy gradually. In 2011, it reached 7 TeV collision energy and the recorded luminosity was $3.3 \times 10^{33} \text{ cm}^{-2} \text{ s}^{-1}$ with an integrated luminosity 5.5 fb^{-1} as can be seen in Fig. 2.3.

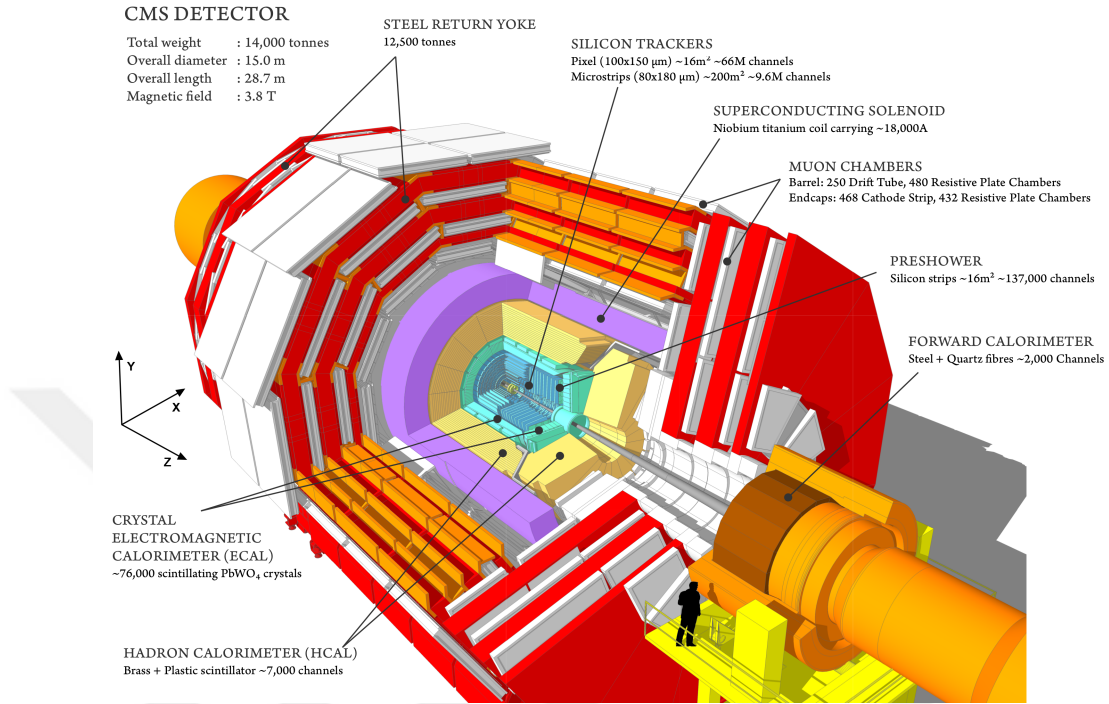


Figure 2.2: Representation of CMS and its different parts: the silicon tracker (blue), the electromagnetic calorimeter (green-blue), the hadronic calorimeter (orange), the magnet (purple), and the muon chambers (white)[11].

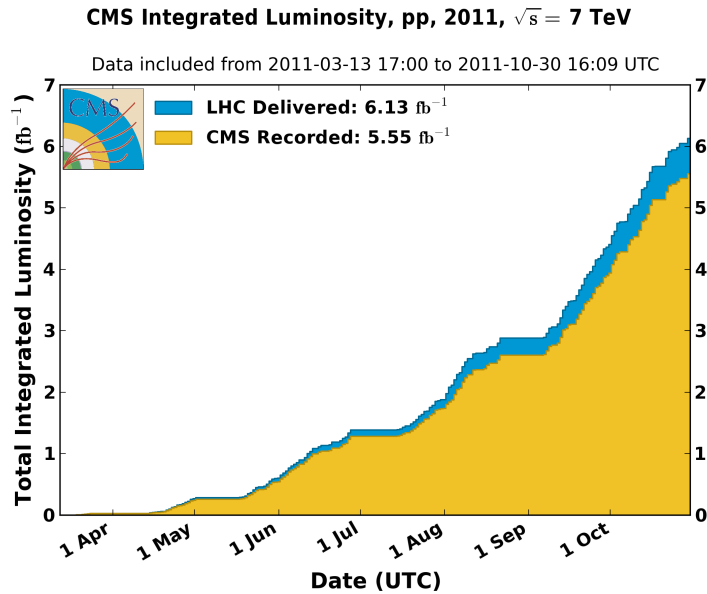


Figure 2.3: CMS integrated luminosity at 7 TeV in 2011.

The CMS detector is organized into specialized sub divisions that are magnet, muon system, electromagnetic calorimeter, hadron calorimeter and inner tracking system.

2.2.1 Superconducting Magnet

One of the main purposes of the CMS detector is to measure the momentum of the high energy particles and muons for the new discoveries. This can be possible with the highest magnetic field at the core region to bend the charged particles to trace their path with a help of good tracking system. Therefore the CMS decided to build a solenoid superconducting magnet around the detector system. This magnet is designed to reach up to 4 T field to get the precision measurement at the vertex region. For some safety purpose the CMS uses 3.8 T instead. As can be seen from Fig. 2.4 the superconducting magnet mainly composed of three parts: a superconducting coil, a vacuum tank, and the magnet yoke. Superconducting coil is made of a four-layer-winding wire to achieve 4T magnetic field. The windings are cooled with a liquid helium flow. A vacuum tank that is made of stainless steel contains superconducting coil. The inner shell of vacuum tank supports all the barrel detector systems. The magnet yoke is composed of six endcap disks and five barrel wheels. The central wheel includes the coil and its cryostat.

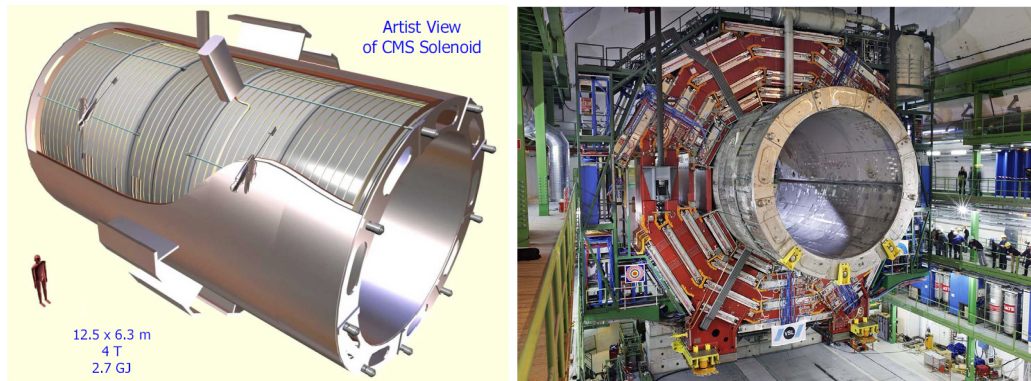


Figure 2.4: Superconducting magnet.

2.2.2 Inner Tracking System

Momentum of particles plays an important role for the particle identification; when the charged particles enter the magnetic field, Lorentz force bend their trajectories. High momentum particles bend more; low momentum particles make bigger curves. One method to find the momentum of particles is to trace these bend trajectories in

the detector. Therefore for the high momentum particles we need a good detector resolution to see the small curvetures.

The CMS tracking system is the most peculiar tracking system ever built. It is located at the center of the CMS detector system. It is designed to get precise measurement of the particles momentum and good secondary vertices. The CMS tracker structured totally with the silicone. It has three cylindrical layers of hybrid pixel detector and two disks of pixel modules (Fig. 2.5 left) located each side. It consists of 13 layers in central region and 14 layers in the endcap region.

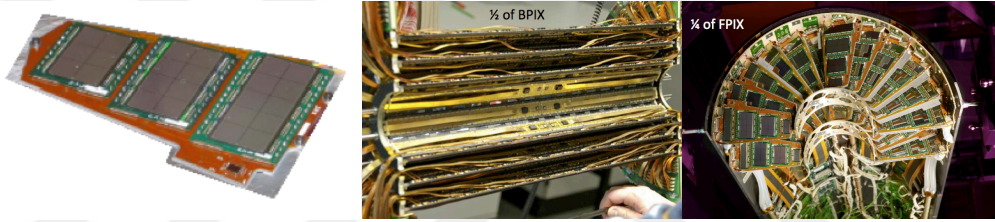


Figure 2.5: Pixel modules (left), barrel pixel (middle), forward pixel (right).

Pixel detector, also called vertex detector, is located in the central region close to the interaction point. It consists of three-barrel layers (Fig. 2.5 middle) extended between 4.4 cm and 10.2 cm and ten-silicon strip tracker extended up to 1.1 m. Barrel pixels consists of a total of 768 modules with a 48 million pixels and 11520 read out chips (ROCs). Forward pixels (Fig. 2.5 right) consists of four disks at 34.5 and 46.5 cm from the interaction point and a total of 672 modules with 18 million pixels and 4320 ROCs. The pixel detectors consist of $100 \times 150 \mu\text{m}^2$ pixels, 66 million in total (Fig. 2.6). It is the innermost detector that is designed to measure the tracking points in $r-\phi$ and z precisely. Therefore it has a small impact parameter resolution that is important for a good secondary vertex reconstruction.

Endcap region consists of 2 disks in the pixel detector and 3 plus 9 disks in the strip tracker on each side of the barrel, extending the acceptance of the tracker up to a pseudorapidity of $|\eta| < 2.5$.

CMS tracker system consists of a total of 1440 pixel and 15148 strip detector modules.

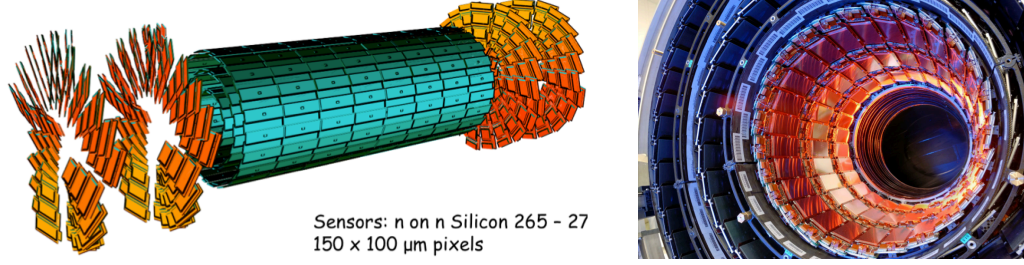


Figure 2.6: The pixel detectors[13].

2.2.3 Electromagnetic Calorimeter (ECAL)

ECAL is designed to measure mainly electron and photon coming from the collision of two protons. Especially it is important to measure two photon that carries a signature of Higgs particle. Since it is located in a very high magnetic field and high radiation area it has to be very rigid and radiation hard to last a longtime. That is why it is made of primarily metal, heavier than stainless steel with a touch of oxygen for a good transparency and scintillates when photon and electron enters the detector.

The ECAL is constructed with the lead tungstate (PbWO_4) crystals, extremely dense and optically clear material. The dimension of the crystals are the $22 \times 22 \times 230 \text{ mm}^3$. The high density (8.28 g/cm^3), short radiation length (0.89 cm) and small Moliere radius (2.2 cm) make this crystals a very fast and compact detector. ECAL has one barrel that covers the pseudorapidity range $|\eta| < 1.479$, two endcaps and one preshower detectors located between tracker and hadron calorimeter (HCAL). The cylindrical barrel consists of 36 super models (Fig. 2.8) that contains 1700 crystals for each (61,200 crystal in total) and the flat endcaps consists of a further 15,000 crystals. Figure 2.7 shows the crystals for both barrel and endcap region.

When the electron and photon penetrates in these crystals they scintillate in the wavelength of 420-430 nm. The energy of the particle that is deposited in these crystals is proportional to the amount of light collected. The scintillating lights are handled by photodetectors that converts light into electrical signals. These photodetectors are avalanche photodiodes (APDs) used for the barrel and vacuum phototriodes (VPTs) for the endcaps[14]. APDs are Hamamatsu type S8148 reverse structure avalanche photodiodes specially developed for the CMS ECAL[15]. Each APD has $5 \times 5 \text{ mm}^2$

active area and a pair is mounted on each crystal. VPTs are vacuum phototriodes type PMT188 from National Research Institute Electron in St. Petersburg specially designed for the CMS[16]. VPTs have a special design for the 4 T magnetic field resistance, it has a single gain stage and an anode of very fine copper mesh (10 μm pitch).

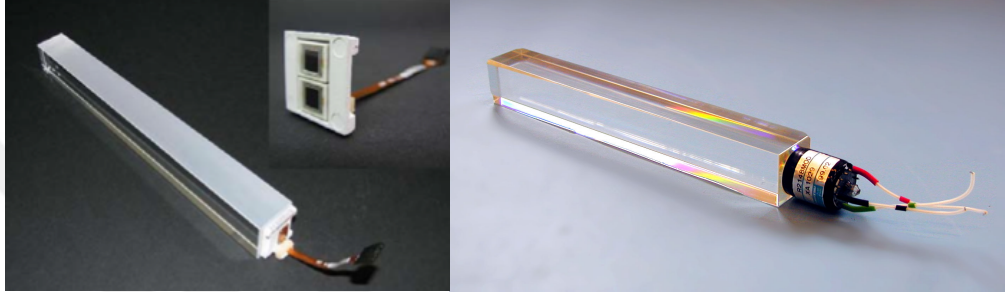


Figure 2.7: PbWO_4 crystals. Upper face is unpolished barrel crystal with its two APDs (left). Polished an endcap crystal attached with VPT (right).

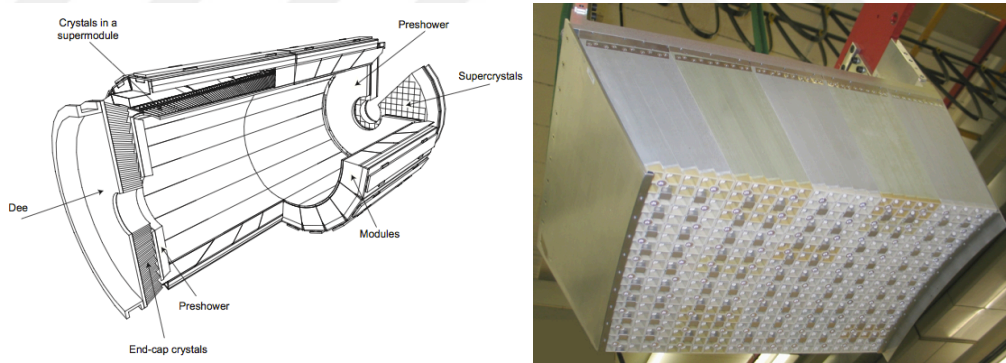


Figure 2.8: ECAL layout showing location of the crystals and modules (left). Front view of ECAL barrel super module equipped with crystals (right).

The Endcap consists of two halves or dees that consists of 3662 crystals. These dees are equipped with an identically shaped crystals that are grouped into 5x5 crystals (supercrystals, SCs) in a mechanical structure (Fig. 2.9).

Preshower detectors are located in front of the ECAL endcap modules, it is designed to identify neutral pions in the endcap within the eta region of $1.653 < |\eta| < 2.6$. It also helps to improve position determination of electrons and photons with a high precision. Preshower detectors consist of two layers: one is the lead radiator that produce electromagnetic shower from the incoming electrons and photons, the other



Figure 2.9: Endcap dee equipped with a 5x5 supercrystals.

is a silicon strip sensor that measures deposited energy and transverse shower profiles. Silicon strip sensors are placed after each radiator.

2.2.4 Hadron Calorimeter (HCAL)

Hadron calorimeter is designed to measure the energy and position of the hadrons such as protons, neutrons, pions, kaons and so on. Moreover it looks at the non-interacting particles such as neutrinos using the momentum conservation in the hermitic structure of the detector. HCAL is the most important calorimeter to discover the higgs and new particles. It also measures the timing and energy of hadronic showers, as well as their angle and position, needed for the generation of level-1 trigger primitives, the high level trigger, and offline reconstruction of jets and missing transverse energy[17, 18, 19].

As you can see from Fig. 2.2 the HCAL is located inside the superconducting magnet and surrounds the ECAL and tracker. It consists of hadronic barrel (HB), hadronic endcap (HE), hadronic outer (HO) and hadronic forward (HF). Longitudinal view and segmentations of these detectors are shown on Fig. 2.10 left and right, respectively.

It consists of 11 separate physical pieces. The positive and negative barrels : HB+ and HB-. The positive and negative endcaps: HE+ and HE-. The positive and negative forward calorimeters: HF+ and HF-. The five rings of the outer HCAL: HO2-, HO1-, HO0, HO1+, and HO2+. The HB, HO and HE calorimeters have similar structures. They are all made of C26000 cartridge brass (70% Cu and 30% Zn) as passive material and plastic scintillator (3.7 mm SCSN81 from Kuraray and

1.0 cm BC408 from Bicron) tiles as active regions. Light emission from the tiles is in the blue violet, with wavelength in the range $\lambda = 410\text{-}425$ nm. This light is absorbed by the wave length shifting fibers which fluoresce in the green at $\lambda = 490$ nm. The green, wave-shifted light is conveyed via clear fiber waveguides to photodetectors. The individual tiles of scintillator are machined to a size of $\Delta\eta\times\Delta\phi=0.087\times0.087$ and instrumented with a single wave length shifting fibers[6]. The HF calorimeters are made of quartz fibers embedded into steel plates.

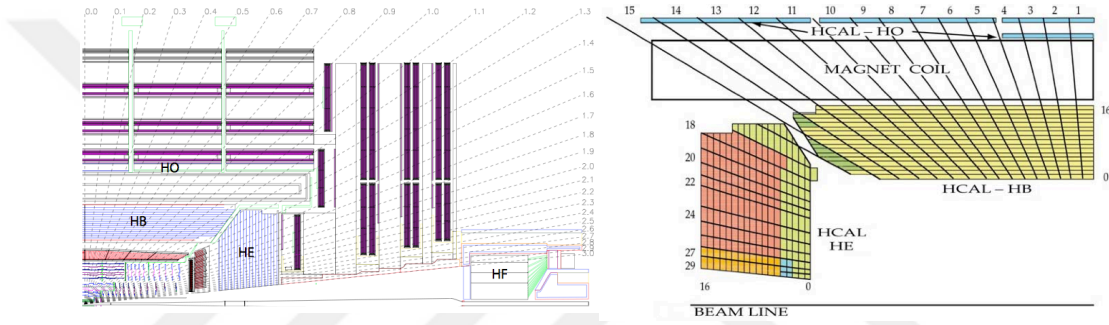


Figure 2.10: Longitudinal view of the CMS detector showing the locations of the HB, HE, HO and HF calorimeters (left). HCAL tower segmentation in the r,z plane (right). 1/4 of the HB, HE, and HO detector towers shown.

2.2.4.1 Hadronic Barrel (HB)

The HB is a sampling calorimeter (Fig. 2.11 (left)) covering the pseudorapidity range of $0 < |\eta| < 1.3$. As mentioned above it is divided into two half barrels, HB+ and HB-. Each half consists of 18 identical azimuthal wedges ($\Delta\phi = 20^\circ$), (see Fig. 2.11 (middle)) and each wedge that weighs 26 tones is segmented into four azimuthal angle ($\Delta\phi = 50$) sectors (see Fig. 2.11 (right)).

The wedges composed of flat brass alloy absorber plates that are known as C26000 cartridge brass (70% Cu, 30% Zn, $\rho=8.53$ g/cm³, $X_0=1.49$ cm and $\lambda_0=16.42$ cm) parallel to the beam axis. The innermost and outermost absorbers are made of stainless steel for structural strength. 17 active plastic scintillator tiles and wavelength shifting fibers called Megatiles are inserted between the steel and brass absorber plates to get the light out (Fig. 2.12)[20].

After exiting the scintillator, the wavelength shifting fibers WLS, (Fig. 2.13 left most)

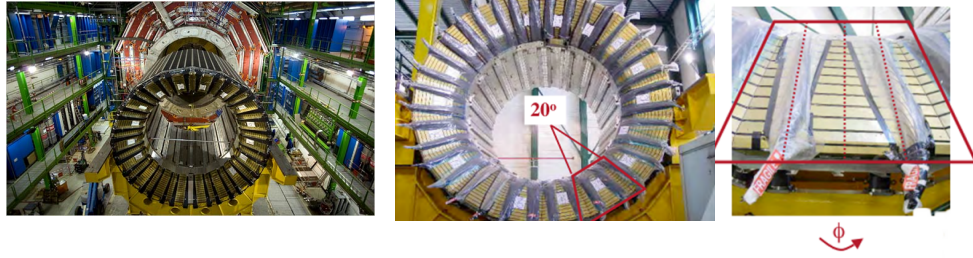


Figure 2.11: Assembled HCAL half-barrel in SX5, the under ground assembly hall (left). Pictures of 20° HB wedges (middle) and each wedge is segmented into four azimuthal angle ($\Delta\phi=50$) (right).



Figure 2.12: Installation of a central megatile.

are spliced to clear fibers (Kuraray double-clad). The clear fibre goes to an optical connector at the end of the tray. An optical cable takes the light to an optical decoding unit, (ODU) (Fig. 2.13 left). The ODU arranges the fibers into read-out towers and brings the light to a hybrid photodiode, (HPD) (Fig. 2.13 right and rightmost)[21]. An additional fibre enters each HPD for direct injection of light using either the laser or a light emitting diode, (LED).

2.2.4.2 Hadronic Endcap, (HE)

Hadronic endcaps are located at the two ends of superconducting magnet. Because of the strong magnetic field in this area this detector has to be made with a non magnetic material. endcaps are also made of similar material that hadronic barrel is

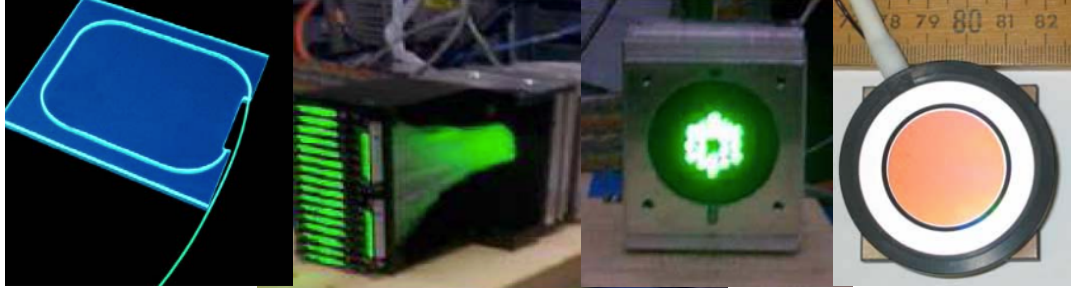


Figure 2.13: Wave length shift fiber is placed in a groove in each scintillator tile (leftmost). ODU (second from the left). 16 fibers from each layer (HB), (second from the right). Fibers on HPD face. 19 pixel HPD (16 η + 2 depths) (rightmost).

made of: C26000 cartridge brass (70% Cu and 30% Zn) that are 79 mm thick with 9 mm gaps to insert the scintillator tiles. Trapezoidal-shaped scintillators are 4.0 mm thick SCSN81 or 9 mm thick bicorn BC408 for Layer-0, and have grooves in which the WLS fibers are inserted. The scintillation light is collected by 0.94 mm WLS fibers and sent to photodetectors which are the hybrid photodiodes[22].

The total number of tiles and trays for both HE calorimeter is 20916 and 1368, respectively. The Megatiles are large sheets of plastic scintillators which are subdivided into component scintillator tiles to provide for reconstruction of hadronic showers. Each HE of HCAL consists of 14 η towers with 5 ϕ segmentation (Fig. 2.14). For the 5 outermost towers (at smaller η) the ϕ segmentation is 5 and the η segmentation is 0.087. For the 8 innermost towers the ϕ segmentation is 10, whilst the η segmentation varies from 0.09 to 0.35 at the highest η . The total number of HE towers is 2304. More details of the HE can be found elsewhere[23].

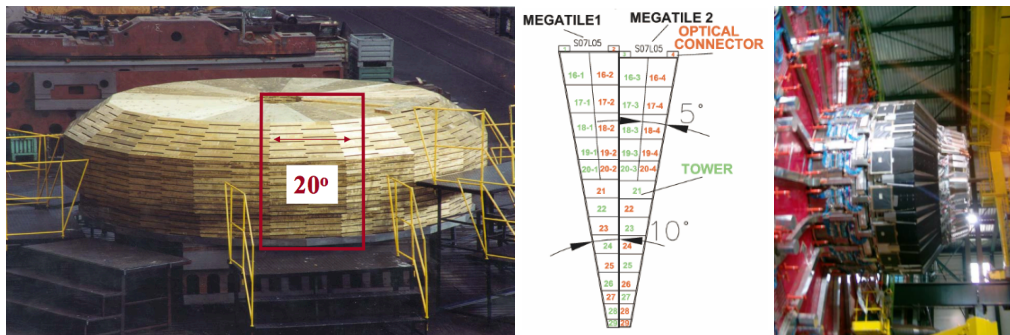


Figure 2.14: A half barrel is made of 18 wedges each subtending 20° in azimuth ϕ (left) and corresponding towers (middle). Located in the CMS detector (right).

2.2.4.3 Hadronic Outer (HO)

The HCAL outer calorimeter (HO) is located just behind the magnet coil inside the magnet flux return yoke (Fig. 2.15 (left)). It provides an additional calorimeter coverage of about 3λ thickness. HO, which functions as a tail-catcher for hadronic showers, is designed to measure the leakage of energy that lead to large fluctuation on an event by event basis and cannot be corrected offline. HO provides a net improvement energy of undetected particles at LHC energies. Information from HO will also be used for the muon trigger in the CMS. HO uses the same active material (scintillator) and WLS fiber (Fig. 2.15 (right)) as the HB and HE calorimeters but uses the steel return yoke and magnet material of the CMS as absorber[24]. The scintillation light is collected with wavelength shifting fibers and transmitted over clear fibers to front end electronics placed close to the layers. The HB, HE, and HO calorimeters are all originally used HPD as photo-sensors.

Any amount of energy that escapes observation will increase the background, making data analysis harder. HO has been designed to reduce the unobserved energy background. QCD events also have missing E_T due to the production of neutrinos. The cross section of QCD events, where at least one particle has E_T above 500 GeV, is estimated to be several pb. Clearly these events will be affected due to leakage of energy in the hadron calorimeter, and the HO would help decrease the background and improve the energy measurement.

HO is physically divided into 5 rings numbered -2, -1, 0, +1 and +2 with increasing η . Each ring of the HO is divided into 12 identical ϕ sectors that each has 6 slices in ϕ . The smallest scintillator unit is called “tile”. The scintillator tiles in each ϕ sector belong to a plane. Perpendicular distance of this plane from the z-axis is 3.82 m for layer 0 and 4.07 m for layer 1. The tiles in each ϕ slice of a ring are mechanically held together in the form of a tray.

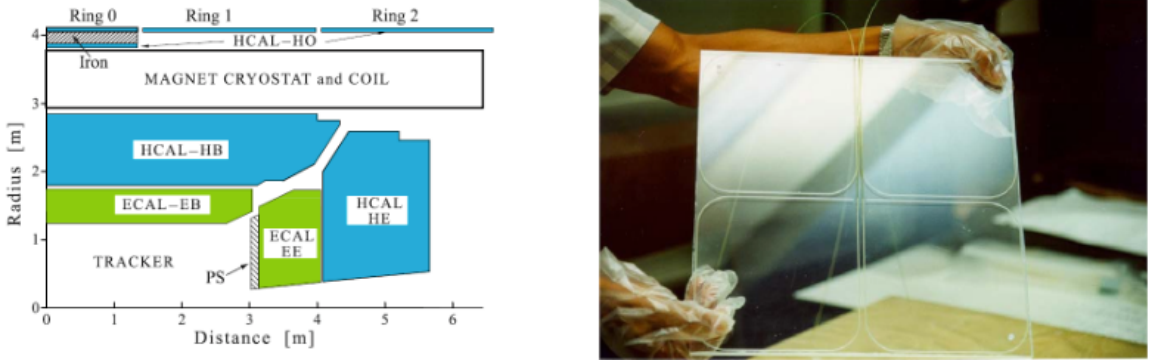


Figure 2.15: A diagram of a quarter section of the CMS showing location of HO (left). An HO scintillator tile with embedded wavelength shifting fibers. The tile size is chosen to match projective towers in the HB (right).

2.2.4.4 Forward Hadron Calorimeter (HF)

HF covers a large pseudorapidity range, $3 < |\eta| < 5$, and thus significantly improve jet detection and the missing transverse energy resolution which are essential in Standard Model Higgs boson, all SUSY particle searches, and top quark production studies. Higgs boson production through weak boson fusion as a potential Higgs discovery channel requires identification of high energy quark jets by the forward calorimeters. HF is also an optical device, but a Cherenkov light device, sitting in a very high radiation environment. The Cherenkov light is produced and transmitted via quartz fibers to photomultipliers. The entire electronics and calibration chain for HF is similar to that of the HB. The HF calorimeter is based on steel absorber with embedded fused-silica-core and polymer hard-clad optical fibers. The fiber diameter is roughly 0.6 mm and the wire spacing is 5 mm. Half a million of fiber are read out by 1728 phototubes (PMT). HF+ and HF- are located at each end of the CMS detector and they consist of a total of 36 wedges. As seen from Fig. 2.16, each wedge contains two readout boxes (ROBOX) that have 24 PMTs each.

The front face is located at 11.2 m from the interaction point. HF consists of two different fiber length, electromagnetic (EM) 165 cm long and hadronic (HAD) 143 cm long. Light is generated by Cherenkov effect in quartz fibers by relativistic charged particles such as electrons. Amount of collected light depends on the angle between the particle path and the fiber axis. Figure 2.17 shows the internal structure of the

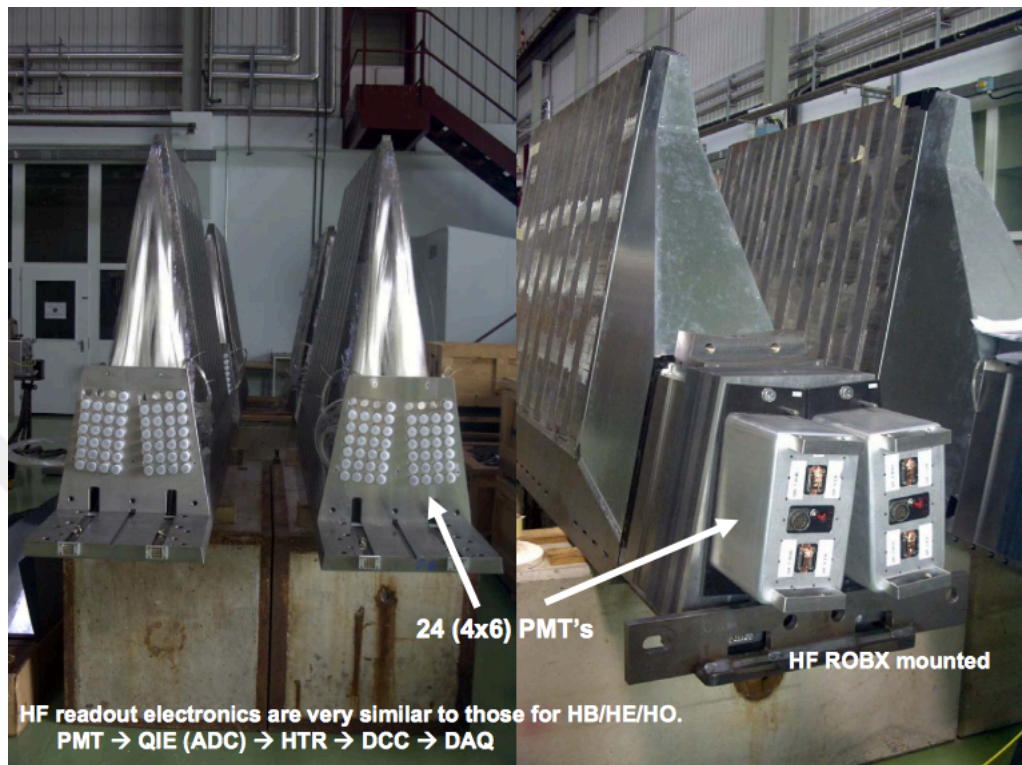


Figure 2.16: Fiber view and ROBOX of HF wedges.

HF wedges and Fig. 2.18 shows the completed form of the HF calorimeters.



Figure 2.17: Fiber view of HF wedges.

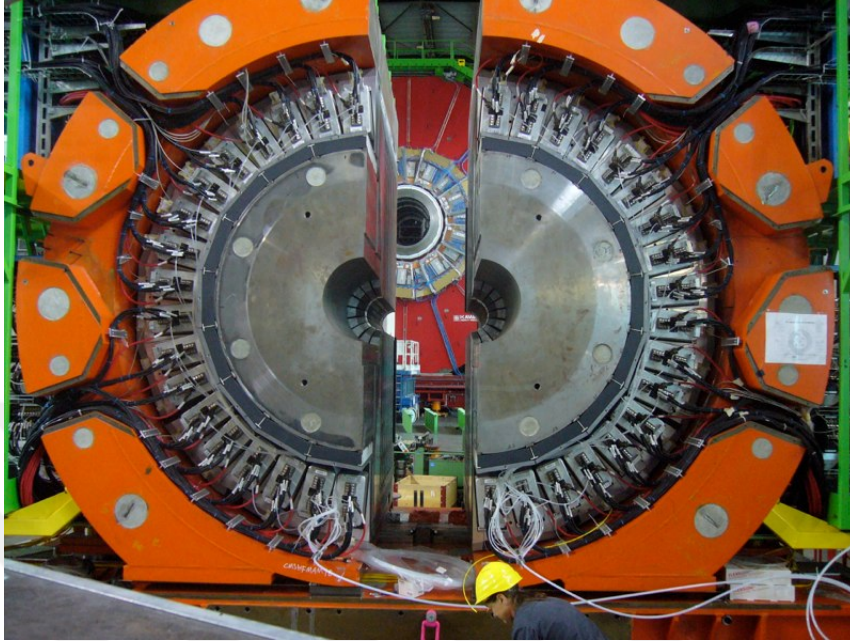


Figure 2.18: Completed HF.

2.2.5 Muon Detector System

Muons are fundamental particles with a charge of -1 as leptons. They are minimum ionizing particles that penetrate several meters of iron without interacting, so that muon chambers are placed in outer region to register only muons. The other particles are stopped before reaching the muon chambers. Figure 2.19 shows a clear trace of the muons registered by the muon chambers. Muons are the clear signature of new particles in CMS such as Higgs which decays to 4 muon.

Muon spectrometer uses three types of gas detectors with trigger capabilities to detect the muons. These are the drift tubes (DT) in the barrel region, cathode strip chambers (CSC) in the endcap region, and resistive plate chambers (RPC) in both the barrel and endcap region[26].

2.2.5.1 Drift Tubes (DT)

Drift tubes are used to track the muon particles, and are made of that 4 cm wide tubes contain wires inside a gas (Ar/CO_2 (85%/15%)). Mainly DT measures muon

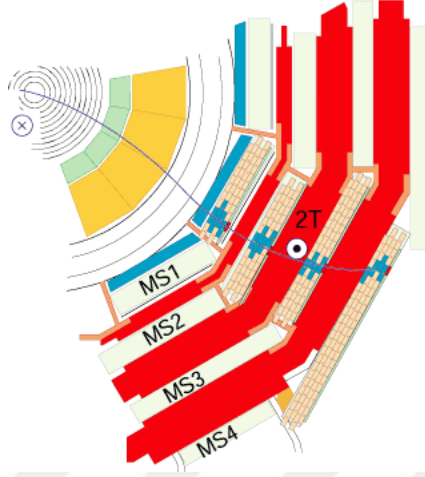


Figure 2.19: Muon track in the muon chambers.

position in the barrel region. It gives two coordinates for the muon positions. Each DT consists of 12 aluminum layers with 60 tubes in the range of $|\eta| < 1.2$ (central coverage) Fig. 2.20 shows the placement of the DTs in the CMS iron yoke.

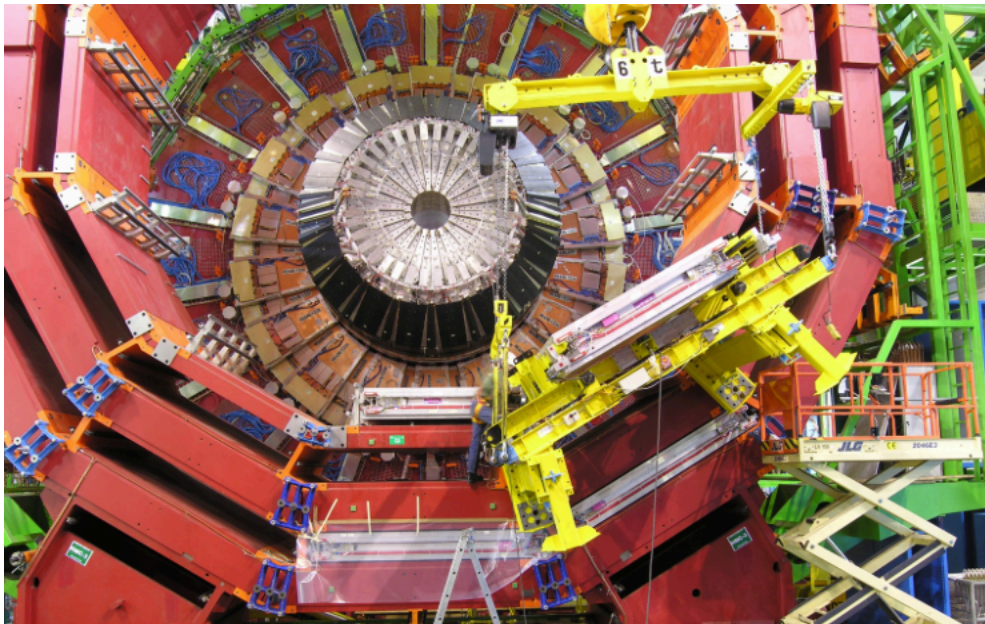


Figure 2.20: Drift chambers in the CMS.

2.2.5.2 Cathode Strip Chambers (CSC)

CSC covers the endcap region with a range of $0.8 < |\eta| < 2.4$. It consists of strip copper plates for cathode and wires for anode with a special gas. When the muon passes through the chamber, it ionizes the atoms of the gas, and produces electron-ion pairs. The ions are collected by the cathode and the electrons are collected by the anode. Collection of an electron at the anode wire creates an avalanche of electrons and collection of ions by the copper cathode induce a pulse in the strips. In the CSC, the strips and wires are perpendicular to each other so that we get two coordinates information from the chambers. Because of closely spaced wires it provides precise time and space resolution for tracking and triggering of muons in the endcaps. Figure 2.21 shows a location of the CSC in CMS[27]. There are total 468 chambers mounted on eight disks - four in each endcap.

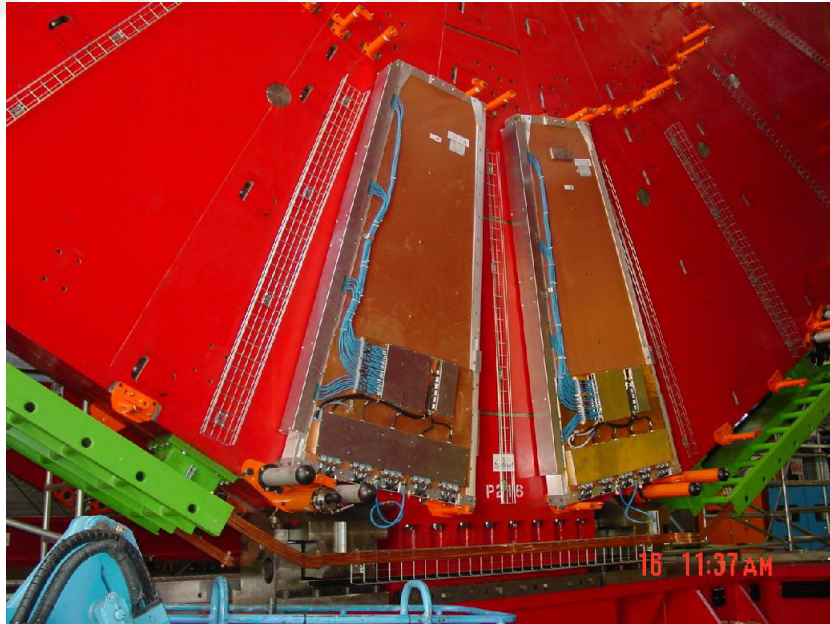


Figure 2.21: Cathod strip chambers in the CMS.

2.2.5.3 Resistive Plate Chambers (RPC)

The RPCs are the gaseous chambers that are made of very high resistivity plastic anode and cathode parallel plates. Robustness of this detector helps to operate in

very high rate and with a high gas gain without developing streamers or sparks. RPCs are located both in barrel and endcap region with a coverage of $|\eta| < 2.1$. It is divided into five wheels in the barrel and three disks in each endcap[28]. Figure 2.22 shows the location of RPC's in the CMS detector.

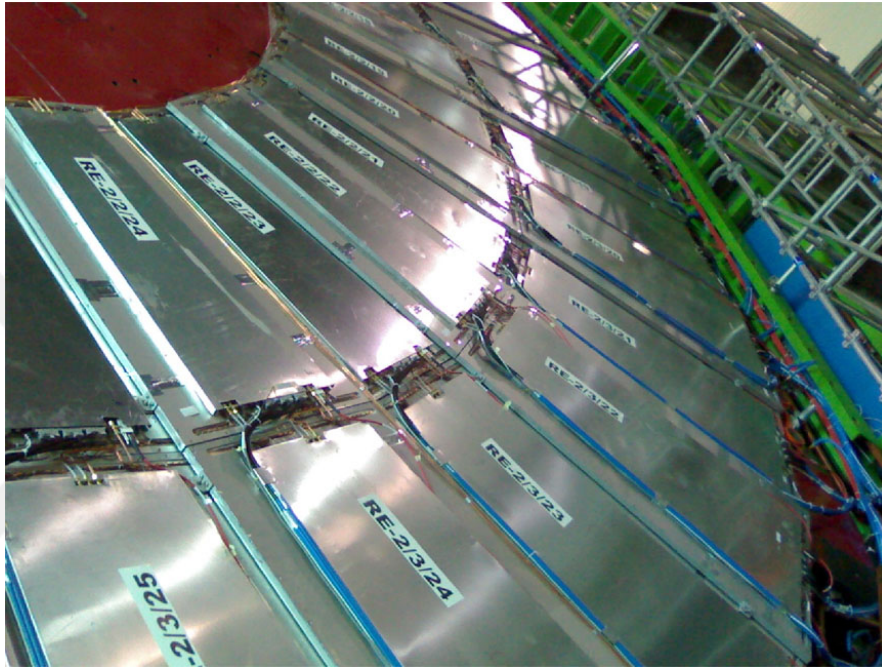


Figure 2.22: Resistive plate chambers in CMS.

3. THEORY

In this section, Standard Model (SM) and Quantum Chromodynamics (QCD) will be described.

3.1 Standard Model

The Standard Model (SM) started to develop in 1970-73. It covers the theory of fundamental particles and their interactions. It is an analogy of periodic table as in chemistry, it classifies particles instead of atoms. The SM contains three sections; leptons, quarks and force carriers which are the fundamental or point like particles. The SM particles are divided into two groups in terms of their intrinsic properties. The building blocks of matter (leptons and quarks) called “Fermions” and the mediators called “Bosons”. Fermions obey the statistics that was developed by Enrico Fermi (1901-1954), Wolfgang Pauli (1902-1984), and Paul Dirac (1902-1984), so called exclusion principle, which states that two fermions can not share the same quantum state. Bosons obey the Bose-Einstein statistic that was developed by Satyendra Bose (1894-1974) and Albert Einstein (1879-1955), it states that two bosons can share same quantum state at the same time.

Fermions such as leptons and quarks have half integer ($1/2$) spin number and bosons such as photon, gluon, W^\pm and Z^0 have integer (1) spin number. Spin 1 bosons are also called vector bosons[25]. Besides vector bosons, there is also spin 0 scalar Higgs boson particle that helps generate the Higgs field to give mass to the particles that pass through this field. There is also a spin 2 boson called graviton that is the

mediator for the gravitational force. The details of those fundamental particles are given in Fig. 3.1.

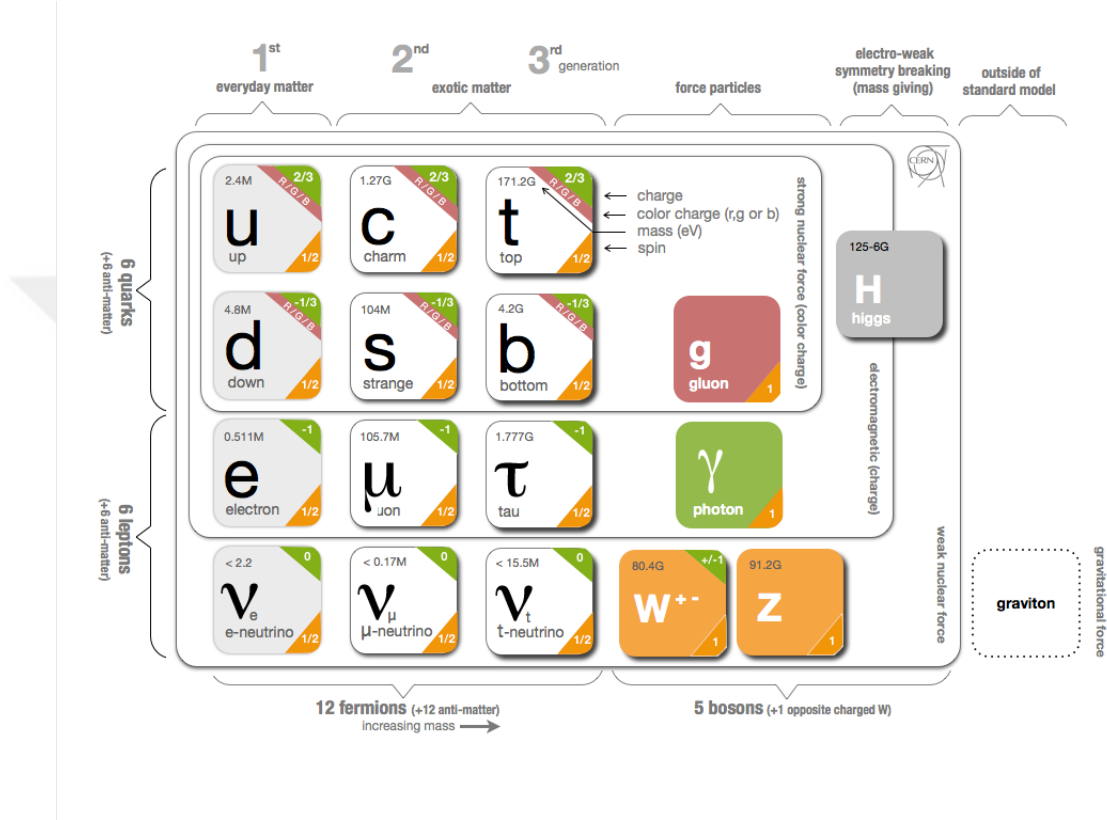


Figure 3.1: Fundamental particles of the standard model.

As can be seen from Fig. 3.1 there are three generation of the particles and their mediators (force carriers). The first generation of the particles are the lightest and most stable particles that make the building blocks of matter and the second and third generations of particles are heavier and unstable particles that make the exotic matter. The force carrier particles make the interaction between these particles.

Basically our understanding of the universe can be explained by using information covered by the SM. Before the matter evolved, quarks and gluons interact freely since the energy and the temperature were too high to bind them together. After temperature drops and energy decreases quarks and gluons bind together to make protons and neutrons, further decrease of the temperature and energy causes to form the matter. Even though SM is a very successful model to explain particles and their interactions, it still does not explain certain subjects such as gravity, dark matter,

anti-matter, different mass of the particles and more.

3.1.1 Fundamental Interactions and Forces

In particle physics, the interactions are described by a mathematical model. The electromagnetic interaction is described by quantum electrodynamics, (QED). The Strong interaction that occurs between colored quarks is described by quantum chromodynamics, (QCD). The weak interaction between flavored particles is described by electroweak theory, (EWT). The SM of particle physics does not include gravitational interaction among the fundamental interactions, even if its mediators would be graviton and the mathematical model would be called quantum gravity. This will be studied in a theory beyond the SM.

- The strong force that binds quarks and gluons to make protons and neutrons. It is a short-range force that acts only between subatomic particles and it loses its affect above a distance of 10^{-15} m. At the same time residual strong force binds nucleons and opposes the repulsion force between protons to hold nuclei together (see Fig. 3.2).
- The electromagnetic force acts between two charges and it plays an important roll keeping electron in the nuclei thus atoms and molecules form.
- The weak force plays an important roll for the nuclear interactions, especially when the neutron decays into proton, electron and electron neutrino via a virtual W^- boson (see Fig. 3.3).

The mediators of these forces are the photon (EM), gluon (Strong), W^\pm , Z^0 (Weak) and graviton (Gravity) also called “gauge bosons”. Three mediators have spin 1 and are also called vector bosons and the graviton has a spin of 2.

Mainly all forces act between particles that have different properties such as electrical charge for electromagnetic force, color charge for strong force, quark flavor for the weak force and mass for the gravitational force. Interaction between quarks, charges and flavors are mediated by gluons, photons and W, Z bosons respectively. The Fundamental interactions and their strengths are given in Table 3.1.

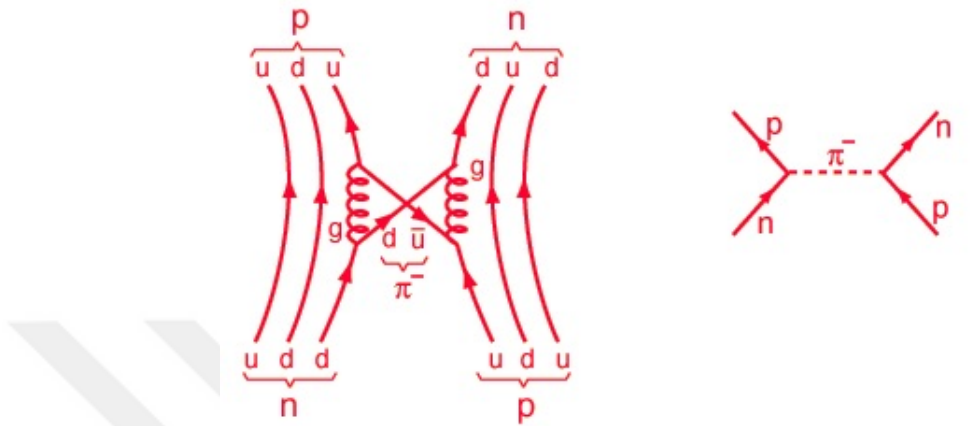


Figure 3.2: Residual strong force binding the nucleons.

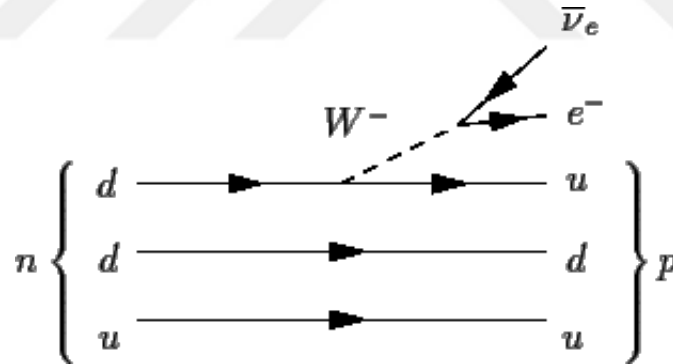


Figure 3.3: Free neutron decays to proton via mediator W boson.

Table 3.1: The forces and interactions.

Property	Interaction				
	Gravitational	Weak (Electroweak)		Electromagnetic	Strong
Acts on:	Mass – Energy	Flavor		Electric Charge	Color Charge
Particles experiencing:	All	Quarks, Leptons		Electrically charged	Quarks, Gluons
Particles mediating:	Graviton (not yet observed)	W ⁺ W ⁻ Z ⁰		γ	Gluons
Strength relative to electromag for two u quarks at:	10 ⁻⁴¹	0.8		1	25
	10 ⁻⁴¹	10 ⁻⁴		1	60
for two protons in nucleus	10 ⁻³⁶	10 ⁻⁷		1	Not applicable to hadrons
					Mesons
					Not applicable to quarks
					20

3.1.2 Fundamental Particles

As was discussed above in the SM, particles are classified by their common properties such as spins and constituents. Half integer spin particles are leptons, quarks and baryons. Integer spin particles are mesons and mediators. Leptons are the fundamental particles also called point particles. They have spin $1/2$ and they don't participate in the strong interactions. There are six leptons; electron, muon, and tau with charge -1 and their neutrinos; neutrinoelectron, neutrino muon and neutrino tau with charge zero. The quarks are also known as fundamental particles that carry spin $1/2$ as leptons. There are six quarks, up (u), charm (c), and top (t) quarks with charge $2/3$ and down (d), strange (s) and bottom (b) quarks with charge $-1/3$. Quarks are the only particles that carry fractional charges, but they combine in three or two quark-anti quark to make particle with a integer charge. In nature an particle with a fractional charge does not exist. The particle listing of the quarks and leptons are given in the Fig. 3.1.

Baryons and mesons are also called “Hadrons” that are composed of quarks and anti quarks. Baryons are fermions with half integer spins ($1/2, 3/2, 5/2, \dots$, etc.) and mesons are bosons with integer spins ($0, 1, 2, 3, 4, \dots$, etc.), (Fig. 3.4). Well known baryons are the proton and neutron that make up the matter and mesons play an important roll for the residual strong force between nucleons. More details of the baryons and mesons can be seen in Tables 3.2 and 3.3[31].

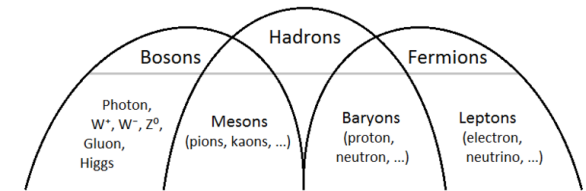


Figure 3.4: The bosons, fermions and hadrons.

In the tables the S and B stands for strangeness and baryon numbers, respectively. For a strong interaction, strangeness has to be conserved in a decay, but it is not mandatory for other interactions. Baryon number is also has to be conserved for all type of interactions according to the SM rules.

Table 3.2: Example of baryons.

Particle	Symbol	Quark Contents	Rest mass MeV/c ²	Spin	B	S	Lifetime (Seconds)	Decay Modes
Proton	p	uud	938.3	1/2	+1	0	Stable	...
Neutron	n	ddu	939.6	1/2	+1	0	920	p e $\bar{\nu}_e$
Lambda	Λ^0	uds	1115.6	1/2	+1	-1	2.6×10^{-10}	p π^- , n π^0
Sigma	Σ^+	uus	1189.4	1/2	+1	-1	0.8×10^{-10}	p π^0 , n π^+
Sigma	Σ^0	uds	1192.5	1/2	+1	-1	6.0×10^{-20}	$\Lambda^0 \gamma$
Sigma	Σ^-	dds	1197.3	1/2	+1	-1	1.5×10^{-10}	n π^-
Delta	Δ^{++}	uuu	1232	3/2	+1	0	0.6×10^{-23}	p π^+
Delta	Δ^+	uud	1232	3/2	+1	0	0.6×10^{-23}	p π^0
Delta	Δ^0	udd	1232	3/2	+1	0	0.6×10^{-23}	n π^0
Delta	Δ^-	ddd	1232	3/2	+1	0	0.6×10^{-23}	n π^-
Xi Cascade	Ξ^0	uss	1315	1/2	+1	-2	2.9×10^{-10}	$\Lambda^0 \pi^0$
Xi Cascade	Ξ^-	dss	1321	1/2	+1	-2	1.64×10^{-10}	$\Lambda^0 \pi^-$
Omega	Ω^-	sss	1672	3/2	+1	-3	0.82×10^{-10}	$\Xi^0 \pi^-$, $\Lambda^0 \bar{K}^-$
Lambda	$\Lambda^+ c$	udc	2281	1/2	+1	0	2.0×10^{-13}	...

Table 3.3: Example of mesons.

Particle	Symbol	Quark Contents	Rest mass MeV/c ²	Spin	S	B	Lifetime (Seconds)	Decay Modes
Pion	π^+	$u\bar{d}$	139.6	0	0	0	2.60×10^{-8}	$\mu^+ \nu_\mu$
Pion	π^0	$\frac{u\bar{u} - d\bar{d}}{\sqrt{2}}$	135.0	0	0	0	0.83×10^{-16}	2γ
Kaon	K^+	$u\bar{s}$	493.7	0	+1	0	1.24×10^{-8}	$\mu^+ \nu_\mu$, $\pi^+ \pi^0$
Rho	ρ^+	$u\bar{d}$	770	1	0	0	0.4×10^{-23}	$\pi^+ \pi^0$
Rho	ρ^0	$u\bar{u}, d\bar{d}$	770	1	0	0	0.4×10^{-23}	$\pi^+ \pi^-$
Omega	ω^0	$u\bar{u}, d\bar{d}$	782	1	0	0	0.8×10^{-22}	$\pi^+ \pi^- \pi^0$
Phi	ϕ	$s\bar{s}$	1020	1	0	0	20×10^{-23}	$K^+ K^-, K^0 \bar{K}^0$
D	D^+	$c\bar{d}$	1869.4	0	0	0	10.6×10^{-13}	$K^+ \pi^0, e^+ \pi^-$
D	D^0	$c\bar{u}$	1864.6	0	0	0	4.2×10^{-13}	$[K, \mu, e]^+ \pi^-$
D	D_s^+	$c\bar{s}$	1969	0	+1	0	4.7×10^{-13}	$K^+ \pi^0$
J/Psi	J/ψ	$c\bar{c}$	3096.9	1	0	0	0.8×10^{-20}	$e^+ e^-, \mu^+ \mu^- \dots$
B	B^-	$b\bar{u}$	5279	0	0	-1	1.5×10^{-12}	$D^0 \pi^-$
B	B^0	$d\bar{b}$	5279	0	0	-1	1.5×10^{-12}	$D^0 \pi^-$
B _s	B_s^0	$s\bar{b}$	5370	0	0	-1	...	$B_s^- \pi^+$
Upsilon	Υ	$b\bar{b}$	9460.4	1	0	0	1.3×10^{-20}	$e^+ e^-, \mu^+ \mu^- \dots$

All the fundamental particles have their corresponding anti-particles such as anti-leptons, anti-quarks, anti-baryons, and anti-mesons. Anti particles have the same mass with the corresponding particle but charges or color charges changes. For instance anti particle of the electron (e^-) is the positron (e^+) and anti particle of the proton, p (uud), is the anti-proton, $\bar{p}(\bar{u}\bar{u}\bar{d})$, so the up (u) quark with charge $2/3$ changes to \bar{u} with a charge of $-2/3$ and down (d) quark with charge $-1/3$ changes to \bar{d} with a charge of $1/3$.

3.2 Quantum Chromodynamics QCD

QCD is a gauge field theory which is defined by strong interactions of the gluons and colored quarks. it is defined by $SU(3)$ symmetry group of the SM. According to the $SU(3)$, there are 3 colored quarks and 8 gluons. According to QCD theory there are three possible colors of a quark defined as red, blue, and green and anti-quarks have anti-colors that are anti-red, anti-blue and anti-green. On the other hand each gluon has one color and one anti-color thus the color is conserved for every quark-quark-gluon, (qqg) vertices. For instance one blue quark can decay into a red quark by emitting one blue-anti-red gluon[32].

QCD describes the interaction of the quark and gluon by using the Lagrangian equation given by (3.1) .

$$L = \sum_q \bar{\psi}_{q,a} (i\gamma^\mu \partial_\mu \delta_{ab} - g_s \gamma^\mu t_{ab}^C A_\mu^C - m_q \delta_{ab}) \psi_{q,b} \frac{1}{4} F_{\mu\nu}^A F^{A\mu\nu} \quad (3.1)$$

where γ^μ is the Dirac-matrices, $\psi_{q,a}$ is quark field spinors for mass m_q , q is a flavor of quark, g_s is coupling constant, index a represents 3 color charges coming from quarks and it takes values from 1 to $N_c = 3$. On the other hands A_μ^C represents gluon field and C superscript changes from 1 to $N_c^2 - 1 = 8$. It gives 8 gluon flavor. The t_{ab}^C corresponds to 8 type of 3×3 matrices and generators of the $SU(3)$ symmetry group. Finally $F_{\mu\nu}^A$ field tensor is given by equation (3.2).

$$F_{\mu\nu}^A = \partial_\mu \mathbf{A}_\nu^A - \partial_\nu \mathbf{A}_\mu^A - g_s f_{ABC} \mathbf{A}_\mu^B \mathbf{A}_\nu^C, [t^A, t^B] = if_{ABC} t^C \quad (3.2)$$

where, f_{ABC} is structure constant of SU(3) symmetry group[34].

QCD theory has a theory called “confinement”. According to this “confinement”, neither quarks nor gluons can be observed alone in the universe. Since the gluons can interact with each other and produce the potential for color field. Thus this potential increases by distance between color charges to keep them non isolated. The only way to observe existence of quarks and gluons is to measure the hadrons that consists of quarks called “valence quarks”. For instance there are three valence quarks (uud) glued by gluons in a proton. In addition to valence quarks, gluons produce virtual quark and anti-quark pairs called “sea quarks”. Those valence quarks, sea quarks and gluons in the proton are called “partons” introduced by Feynman in 1969. The momenta and number of the partons in the proton changes in time continuously. The average momentum distributions of partons in the proton on time described by parton distribution function (PDF). The PDF represents probability densities of partons having a momentum fraction x of the proton energy (Q^2). PDFs are measured as an experimentally and used as input for perturbative QCD (pQCD) that will be described in the following section[33].

QCD method contains perturbative expansions in coupling. Feynman rules for QCD contains quark-anti-quark-gluon (q \bar{q} g) vertices, three gluon vertices (proportional to g_s) and four gluon vertices (proportional to g_s^2). Fundamental parameters of QCD are the coupling g_s ($\alpha_s = \frac{g_s^2}{4\pi}$) and quark mass (m_q)[34].

3.2.1 Perturbative Quantum Chromodynamics pQCD

The pQCD is a theory of approximations which allow to apply perturbation theory techniques for the strong coupling constant α_s in QCD. It can be applied in such processes that happens in short distances and time. Infra-red safety and factorization approach can be calculable using the pQCD. In the hadronization period it plays an important role to understand the parton level processes. In the hard scattering of

the hadron-hadron collisions, the final particles are produced as partons (jets) and others[35]. Figure 3.5 shows a Feynman diagram of final state particles that come out from hadron collisions such as $p - p, p - \bar{p}$ ($h_A + h_B \rightarrow \text{jet} + X$).

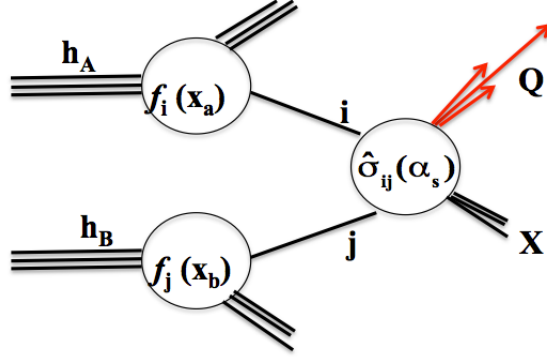


Figure 3.5: The visualization of the Feynman diagram for hadron collisions.

Transverse Energy of jet E_T is the sum of all transverse momenta of particles in the jet. The corresponding jet production cross section is given by Eq. (3.3).

$$\sigma(p_A, p_B) = \sum_{i,j} \int dx_a dx_b f_{i/h_A}(x_a, \mu_F^2) f_{j/h_B}(x_b, \mu_F^2) \hat{\sigma}_{i,j}(p_A, p_B \alpha_s(\mu_R), Q^2, \mu_F^2, \mu_R^2) \quad (3.3)$$

where, $f_{i/h_A}(x_a, \mu_F^2)$ and $f_{j/h_B}(x_b, \mu_F^2)$ are parton distribution functions (PDFs) which give the probability of finding a parton of i and j with momentum fraction x_a and x_b in the hadron h_A and h_B . The x_a and x_b are momentum fractions ($x = p_{\text{parton}}/p_{\text{nucleus}}$) of the total momenta p_A, p_B coming from h_A, h_B hadrons. μ_F and μ_R are factorization and renormalization scale respectively.

Finally $\hat{\sigma}_{i,j}(p_A, p_B \alpha_s(\mu_R), Q^2, \mu_F^2, \mu_R^2)$ is partonic cross section which interacts at the momentum transfer $Q^2 = E_T^2$ [36].

The running coupling $\alpha_s(\mu_R)$ is a basic parameter for pQCD predictions and defined as a function of renormalization scale. When μ_R close to Q scale $\alpha_s(\mu_R^2 \simeq Q^2)$, this is signature of the effective strength of hard interaction. In the high p_T process, partonic cross sections are given by Eq. (3.4) are calculated as series expansion in strong coupling constant, α_s .

$$\hat{\sigma} = \alpha_s^k \left(\hat{\sigma}^{(0)} + \frac{\alpha_s}{\pi} \hat{\sigma}^{(1)} + \left(\frac{\alpha_s}{\pi} \right)^2 \hat{\sigma}^{(2)} + \dots \right) \quad (3.4)$$

The cross section is formalized as an order of α_s where the first order is called Leading Order (LO), the second order is Next to Leading Order (NLO) and the third order is Next-Next to Leading Order (NNLO), ..., etc. The first LO order calculates magnitude of the cross sections and distributions. However the jets coming from the partons start to be observed beyond the LO. In order to compare experimental jet cross section measurements with the theory, jet definition must do and compare with the NLO measurements[37].

3.2.2 Numerical Measurements of NLO

In this thesis five different PDF sets are used to calculate NLO calculations. For this purpose NLOJet++ program (v2.0.1)[38] is used within framework of the fastNLO package (v1.4)[39].

The PDF sets are: NNPDF2.1[40], CT10[41], MSTW2008NLO[42], HER-APDF1.0[43], and ABKM09[44] at the corresponding default values of the strong coupling constant $\alpha_s(M_z) = 0.1180, 0.120, 0.119, 0.1176, \text{ and } 0.1179$, respectively.

3.3 Non-Perturbative QCD (NP)

The perturbative QCD (pQCD) predictions include initial-state radiation, which form parton scattering from hadron-hadron interactions. At the experimental high energy physics, non-perturbative corrections are applied to bring parton level calculations to particle level. For this purpose next-to-leading order (NLO) predictions of pQCD are corrected for non-perturbative (NP) effects, which include hadronization and multiple parton interaction (MPI).

3.3.1 Hadronization

pQCD is valid at short distances and breaks down at long distances. In this case, the colored quarks transform into colorless particles so called hadronization. We are not able to observe partons from hard scattering at the detector level but observe hadrons, which pass on hadronization process. After quark-antiquark collision at hard scattering, the outgoing partons carry color charge and create strong color fields between themselves. The strong color fields between charge and anti-charge increase linearly with a separation of charges until getting enough energy to create additional quark-antiquark pairs. Due to this reason, every time original parton loses some of its own energy and momentum until there is not enough energy to create a new quark-antiquark pairs left and thus color charge becomes neutral end of the hadronization process. The original parton transforms into a shower of hadrons that is known as a particle jet. Thus the energy of hadrons collimate into calorimeter cluster which known as calorimeter jets and observed by detector.

3.3.2 Multiple Parton Interaction, (MPI)

Multiple Parton Interactions are defined as a scatter that does not take a role at the hard scattering directly. In the proton beam, the initiator partons produce an initial-state radiation that transforms from parton level to detector level, and leaves behind pair of parton remnant called spectators. These spectators that are separated from original color charge produce color fields and then also it may produce parton showers as well. Thus, the spectators interact with out-going partons and also softly with each other. Moreover, spectators introduce degrees of freedom by sharing some of the energy of original parton. This energy causes more energy than getting energy from particle jets and calorimeter jets. All of these parton interaction which are not calculated from hard scattering, can be grouped as an underlying event (UE)[33].

3.3.3 Non-Perturbative Corrections

In order to derive NP correction factor, the following MC event generators are used: PYTHIA6 (tune Z2) and HERWIG++ 2.4.2[45]. For MC event generators, both Nominal and noMPI-noHAD settings are applied. Nominal settings refer to cross section measurements obtained from MC generations which includes hadronisation and MPI, while noMPI-noHAD settings refer to cross section measurements obtained from MC generations with hadronization and MPI effects switched off. NP correction factor is defined as the ratio of Nominal setting to noMPI-noHAD setting:

$$\text{NP correction} = \frac{\text{predictions with nominal settings}}{\text{predictions with MPI and Hadronization switched off}}$$

The NP correction factor calculated for each rapidity region as a function of PFjet p_T and fitted with same fit function, $[0]+[1]/\text{pow}(x,[2])$ for both PYTHIA6 (tune Z2) and HERWIG++ 2.4.2. The systematic errors are calculated by getting center of bin for every fit function separately. Thus only one NP correction factor, which is produced from both MC generators, is used for NLO of pQCD predictions.

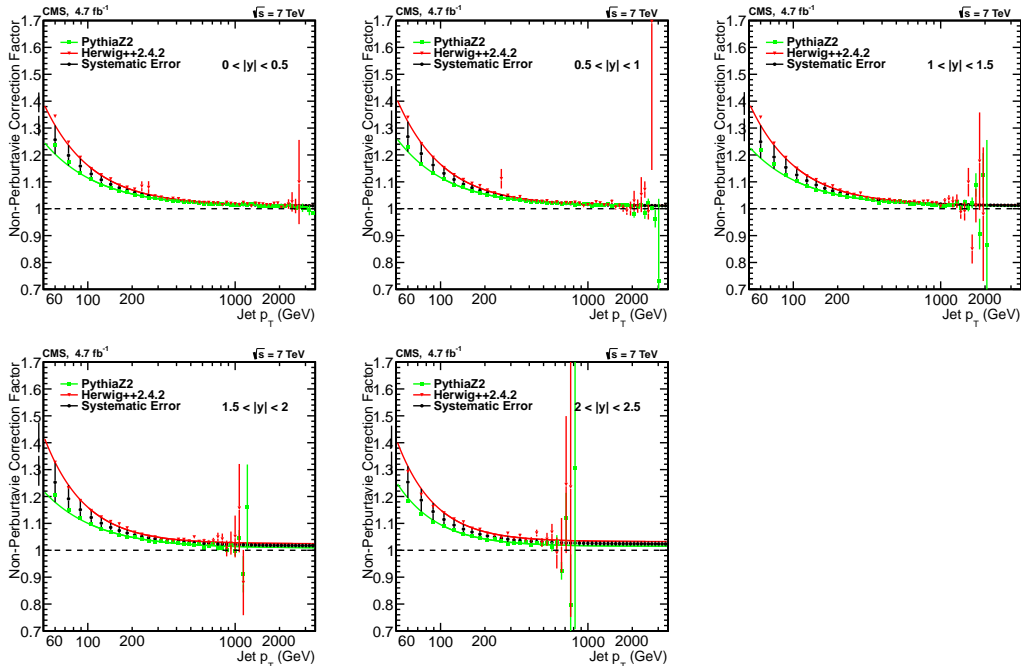


Figure 3.6: NP correction factor from PYTHIA6 (tune Z2) and HERWIG++ 2.4.2 for different rapidity region.

In Fig. 3.6 the top line (Red) shows the HERWIG++ results, the bottom line (green) shows the PYTHIA results and the middle black line shows the average values of both PYTHIA and HERWIG++. Thus the average values are used for the final corrections[46].

3.4 Theoretical Uncertainty Correlations

The theoretical predictions for the jet energy cross section measurements consist of a next-to-leading-order (NLO) QCD calculation, non-perturbative (NP) correction to account for the multiparton interactions (MPI), hadronisation effects (HAD), renormalization and factorization scale uncertainty μ_R and μ_F .

As seen in Fig. 3.7, PDF uncertainty with colored red is the dominant source of uncertainties on theory predictions of up to 30% at highest jet p_T in five rapidity region. Additional uncertainty comes from NP correction with colored green and adds 10% for theory prediction. Variation of the strong coupling constant $\alpha_s(M_z)$ by ± 0.001 introduces 1%-2% uncertainty. The uncertainty coming from the choice of μ_R and μ_F is estimated as the maximum deviation at the six points $(\mu_F/\mu, \mu_R/\mu) = (0.5, 0.5), (2, 2), (1, 0.5), (1, 2), (0.5, 1), (2, 1)$, where $\mu = p_T$ for inclusive jets[47].

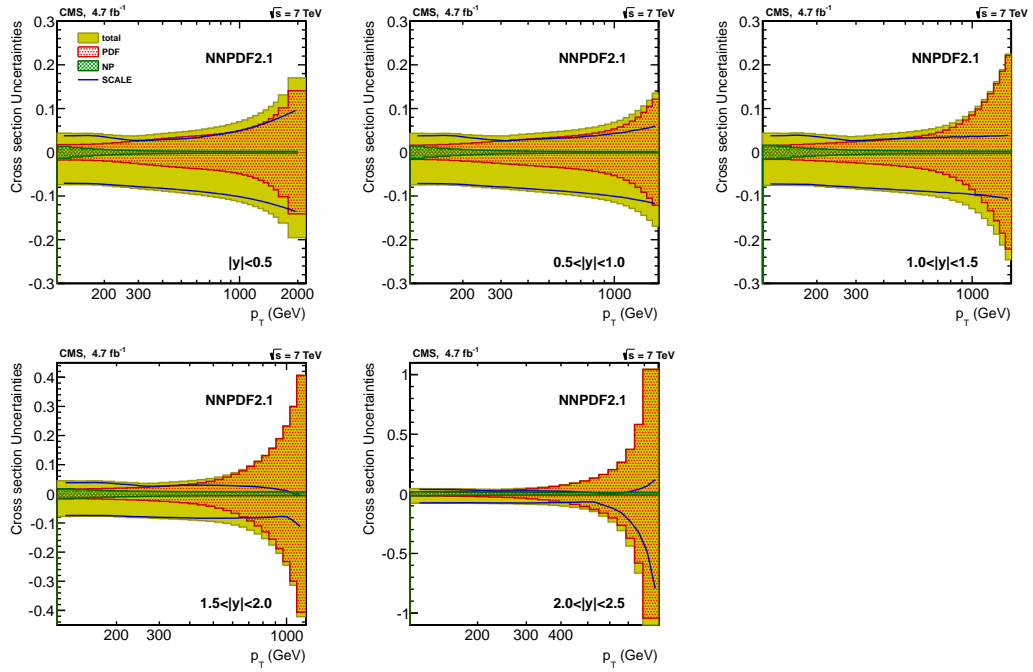


Figure 3.7: The theoretical uncertainties on theoretical inclusive jet p_T cross section measurements in five rapidity region for NNPDF2.1 PDF set.

4. JET RECONSTRUCTION

Quarks and gluons that carry a color charge have not been observed in nature as single particles because of the color confinement. On the other hand, combining quarks and gluons make the hadrons as colorless particles. In the high energy physics experiments such as the CMS experiment, the quarks and gluons are generated by two head on protons at a high energy. This is called as “parton level”. Then, these quarks and gluons recombine and produce hadrons known as hadronization process. After transforming the partons into hadrons, the hadrons scatter through like a cone shape. This cone shaped jets are experimental signatures of the quark and gluons in high energy physics. Figure 4.1 shows a jet production during the hard p-p scattering with high energy.

These particle jets penetrate the CMS detector and leaves their signature in the trackers, ECAL and HCAL calorimeters. Later the jets are reconstructed by the CMS jet algorithms by combining the signatures. These jets are called as reconstructed jets in the CMS experiment. There are three types of reconstructed jet methods defined by the CMS detector. One of them is the calorimeter jets (CALOJets) based on calorimeter, the other one is the jet plus tracks jets (JPTJets) based on trackers and calorimeter jets and the last one is the particle flow jets (PFJets) based on information coming from all the subdetectors of the CMS experiment. In this analysis PFJets are used to construct the inclusive jet cross section. More details of the PFjets and jet clustering algorithm are given in the following sections.

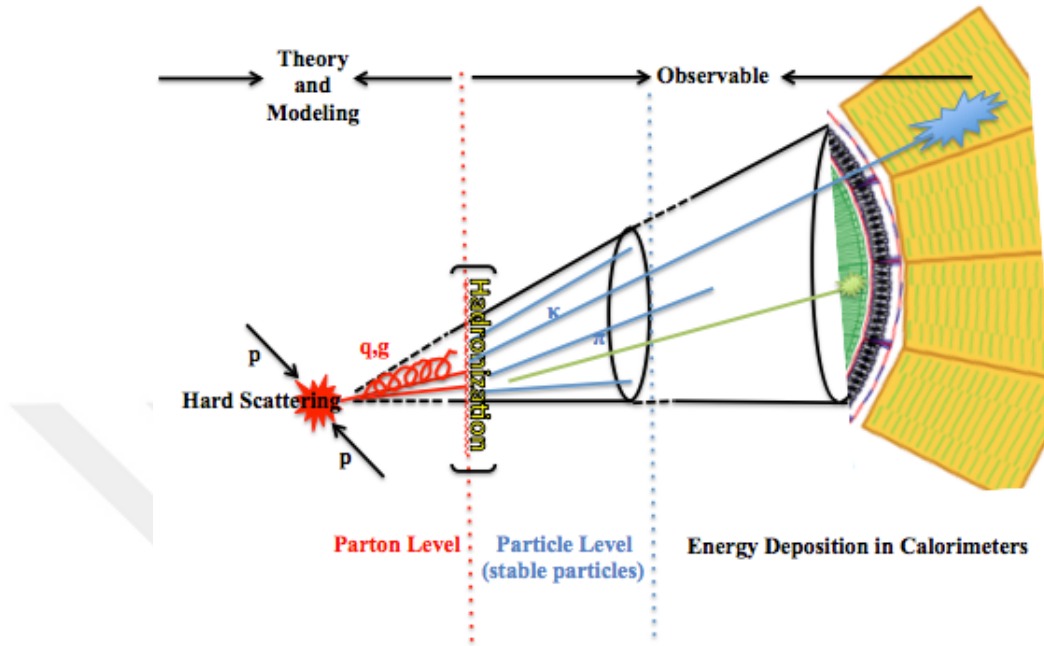


Figure 4.1: Jet production at the p-p collision.

4.1 Jet Clustering Algorithm

The jet clustering is a jet finding method which is one of the important method to analyze the data coming from hadronic collisions. All the objects are recombined with jet algorithms by reconstructing jet momentum. In order to cluster the jets, they require two important theoretical constraints that are infrared safe (IRS) and collinear safe. IRS means that when the soft particles join randomly into the list of the cluster object, the final jets are never affected, in other words the soft particles do not change the jet shapes. Collinear safety is based on collinear splitting which emits a gluon at the small angle. If there are two adjacent calorimeter inputs that are placed in only one jet size, these two adjacent inputs should cluster into two jets for collinear unsafe algorithms while collinear safe algorithms cluster them into only one jet. The collinear split is not important for the collinear safe algorithm and should not change jet shape. Infrared safety and collinear safety algorithms are shown schematically in Fig. 4.2. The first two shapes on the left hand side represent collinear safety algorithm and next three shapes on the right hand side represent infrared safety algorithm. It can be seen from Fig. 4.2 that collinear split does not

change the jet shape for collinear safety algorithm and soft particles does not effect the final jet shape for infrared safety algorithm.

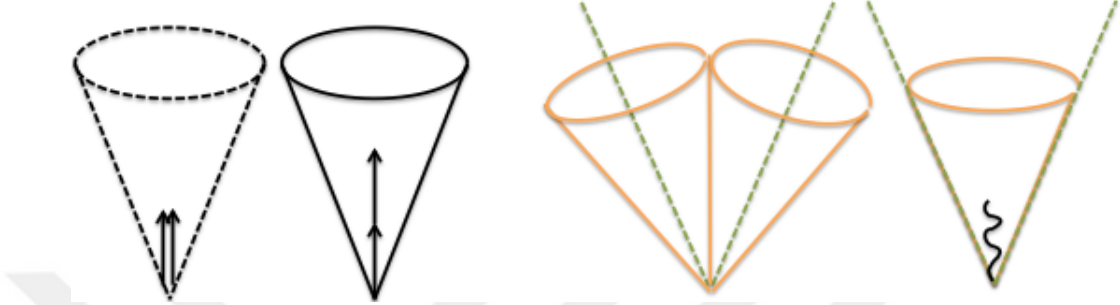


Figure 4.2: Collinear safety (left two shapes) and infrared safety (right three shapes) algorithms.

Two kind of jet algorithms are used widely for hadron colliders to recombine all the objects by using four-momenta: cone type algorithms and sequential clustering algorithms.

The cone algorithms are classified as midpoint cone, iterative cone and seedless infrared-safe cone, (SISCone)[48]. Cone algorithms define a jet as dominant direction of the energy flow. In order to find dominant energy flow's direction, first algorithm defines more energetic particles in the events as a seed and then, it presents a stable trial cone around the seed with the fixed R radius in the $(y - \phi)$ space. So it calculates all 4-momenta of the particles into points of the trial cone at the same direction. Next this stable trial cone is defined as a trial jet and trial jet axis is compared with seed axis. If they are identical, trial jet is called as a jet. Finally, all the particles in the jet from the events are removed and the procedure is repeated with the next hardest seed (more energetic) by using new 4-momenta results. This procedure is iterated by starting from only one seed for center of cone until finding a stable final cone and leaving any single one seed behind. This is called iterative cone method.

Midpoint cone algorithm defines a cone around the hardest seed by summing transverse momentum of all particles above a seed threshold. Then algorithm adds midpoints between pairs of the stable cones into new set of seeds. This kind of algorithm implements overlapping hardest cone couples.

Although midpoint and iterative cone algorithms are experimentally basic, they fail

to give finite perturbative results. Because, the hardest particle could easily change with quasi-collinear splitting for high order perturbative calculations at the particle level. Because of these reason this kinds of algorithms are known as IR and collinear unsafety algorithms. Otherwise, SISCone algorithm is IR and collinear safety cone (IRC) algorithm which is currently the standard cone algorithm at the LHC. SISCone algorithm is seedless cone algorithm that defines all possible subsets of the particles in event and determines rapidities, azimuthal angles and momenta of them. Each subset represents cone centered on corresponding rapidity and azimuthal angles. It also checks whether each cone contain all particles in subsets. If so, subset is called as a stable cone.

The sequential clustering algorithm is the most comprehensive algorithm for inclusive jet research at the hadron colliders[49]. The sequential recombination algorithms are classified as k_t , Cambridge/Aachen (CA), anti- k_t algorithms. These kinds of algorithms are IRC safety algorithms as well as soft resilient, which recover small part of the lost momentum resolution because of the pile-up and underlying event effect on data. The sequential recombination algorithms define d_{ij} distances between the i and j objects in event and d_{iB} distances between the i object and beam axis, B. The cluster calculates all the d_{ij} and d_{iB} distances of the particles until it finds the smallest one. If the smallest one is d_{ij} , the cluster combines i and j objects by summing 4-momenta of them and searches for next smallest ones. If the smallest one is d_{iB} , the cluster defines i object as a jet and removes it from particle list. Then algorithm recalculates distances and the procedure is repeated until all particles are clustered into a jet and being a $d_{ij} > d_{iB}$. This algorithm parameterizes power of the energy scales and it calculates distances according to Eqs, (4.1) and (4.2).

$$d_{ij} = \min(k_{ti}^{2p}, k_{tj}^{2p}) \frac{\Delta_{ij}^2}{R^2} \quad (4.1)$$

$$d_{iB} = k_{ti}^{2p} \quad (4.2)$$

where, $\Delta_{ij}^2 = (y_i - y_j)^2 + (\phi_i - \phi_j)^2$ and the k_{ti} , y_i and ϕ_i represent transverse momentum, rapidity and azimuth angle for i particle, respectively while R is radius

parameter and p is the parameter for the relative power of the energy versus geometric scale. The p parameter distinguishes sequential recombination algorithm classes: $p > 0$ condition corresponds to k_T algorithm, $p = 0$ condition reverts to CA algorithm and $p < 0$ condition refers to anti- k_T jet clustering algorithm.

The inclusive jet particles are clustered by anti- k_T algorithm in this thesis. The anti- k_T algorithm behaves like an ideal cone when it clusters particles as a jet. It has extra characteristics compared to other algorithms. The soft resilient shows general behavior, in other words soft particles like a pile-up and underlying events do not change shape of jet for the entire IRC safety algorithm. For instance; there are two definitions in calculations of jet area, passive area and active area. The passive area means to calculate susceptibility of jets for point-like radiation while active area means to calculate susceptibility of jets for diffusion radiation. The active and passive areas are identical for only anti- k_T jets in comparison with the other jet algorithms since the boundaries of the anti- k_T jets are not affected by soft radiation. The effects of soft radiation on the momentum energy resolution is related with the values and fluctuations of the jet area and this effect approaches to zero for only anti- k_T algorithm.

Another property is back-reaction which means that “net transverse momentum is changing for each of the two hardest jets due to the reassignment of non-pileup particles when one adds high-luminosity LHC pileup to the event”. This hard jet event is strongly suppressed for anti- k_T jet algorithm by comparing with the other algorithms. So, this characteristic of anti- k_T algorithm helps to reduce smearing of the jet transverse momentum due to soft radiation. In order to make a clustering, jet algorithms require fast computing time. For this reason jet algorithm has to provide fast implementation. The anti- k_T jet algorithm is faster than k_T jet algorithm for FastJet implementation[50]. This is another important characteristic of the anti- k_T jet algorithm. It is reported that other characteristics are related to the anti- k_T jet algorithm in reference[49].

In this thesis FastJet implementation package is used to cluster the anti- k_T jets. The FastJet package is a software package which is supported by C++ programming and called as CMSSW. Also FastJet package calculates jet area by identifying jets

and calculates pile-up and underlying event subtraction, as well as defines the jet's area[50].

4.2 Particle Flow Jets (PFJets)

For this analysis, the particle flow jets that are reconstructed by combining all the information, such as e^- , μ , γ , charged and neutral hadrons in events coming from all the sub-detector are used. According to the PF reconstruction algorithm[51], charged particles are reconstructed by using ECAL and HCAL energy clusters and corresponding correlated trackers, while neutral particles are reconstructed by ECAL and HCAL energy clusters. In this case, trackers allow to identify neutral particle energy from charged particle energy deposited in the ECAL and HCAL energy clusters by using their tracks momentum. The energies of the muons are measured with a high efficiency by using information of the muon chambers and the trackers. The energy of the photons is measured by hermitic ECAL crystal, which has good granularity and perfect energy resolution. The energy of the electrons are obtained from bremsstrahlung photons emitted by electrons deposited in the ECAL energy clusters with their correlated tracks. The energy of the charged and neutral hadrons is measured from HCAL energy clusters that surrounds ECAL embedded in the solenoid coil. The HCAL has 25 times more granularity than ECAL that does not allow energy depositions of the charged and neutral hadrons with jets p_T above the 100 GeV. However, in the combined ECAL and HCAL system, the hadron energy resolution is 10% in 100 GeV. This hadron energy resolution is affected by the energy of the charged hadrons directly as if they are neutral hadrons. The energy of the charged hadrons is measured from angular momentum of the trackers and energy resolution of the corresponding ECAL and HCAL calorimeters. Finally, the energy of the charged hadrons, which have particles with the high pseudorapidity between 3.0 and 5.0, are obtained from HF placed 11 m. away from the interaction point.

In this analysis jets are reconstructed using the anti- k_T clustering algorithm as described before with size parameter $R=0.7$. The clustering is performed using four-momentum summation, where the chosen size parameter allows for the capture of

most of the parton shower. The inputs to the jet clustering algorithm are the four-momentum vectors of the reconstructed particle-flow jets, PF_{jet} . Each individual particle is reconstructed with the PF_{jet} technique which combines the information from all the sub-detector of the CMS experiment. For example, charged hadrons are reconstructed by using the trackers, ECAL and HCAL energy clusters, the neutral hadrons are reconstructed by using the ECAL and HCAL energy clusters and, also known as electromagnetic particles, the charged e^\pm are reconstructed by trackers and ECAL energy clusters while neutral photons are reconstructed by only ECAL energy clusters.

The jet energy fractions are carried by charged particles (hadrons, electrons and muons) and neutral particles (photon and neutral hadrons) within jets. Energy of the particles measured with the help of the calorimeter clusters via electromagnetic and hadronic showers in the CMS detector.

Normally CMS calorimeter towers deposit approximately 65% of the energy compositions from charged hadrons, 27% from neutral electromagnetic fractions (photons), 10% from neutral hadron fractions and, 1% from invisible particles like neutrinos that will be described in missing transverse energy section. Figures from 4.3 to 4.7 show inclusive PF_{jet} jet energy fractions which belong to different triggers in five eta region for DATA and MC events. It shows that over 99% of the PF_{jet} is reconstructed after they passed from the event and jet selection criteria which will be shown in the following section[47].

In Fig. 4.3, filled area with red, green and, dark blue colors represent CHF, NEF and, NHF for DATA events, respectively, while black open circle, open square and, open diamond represent charged hadron fraction, neutral electromagnetic fraction and, neutral hadronic fraction for MC events, respectively.

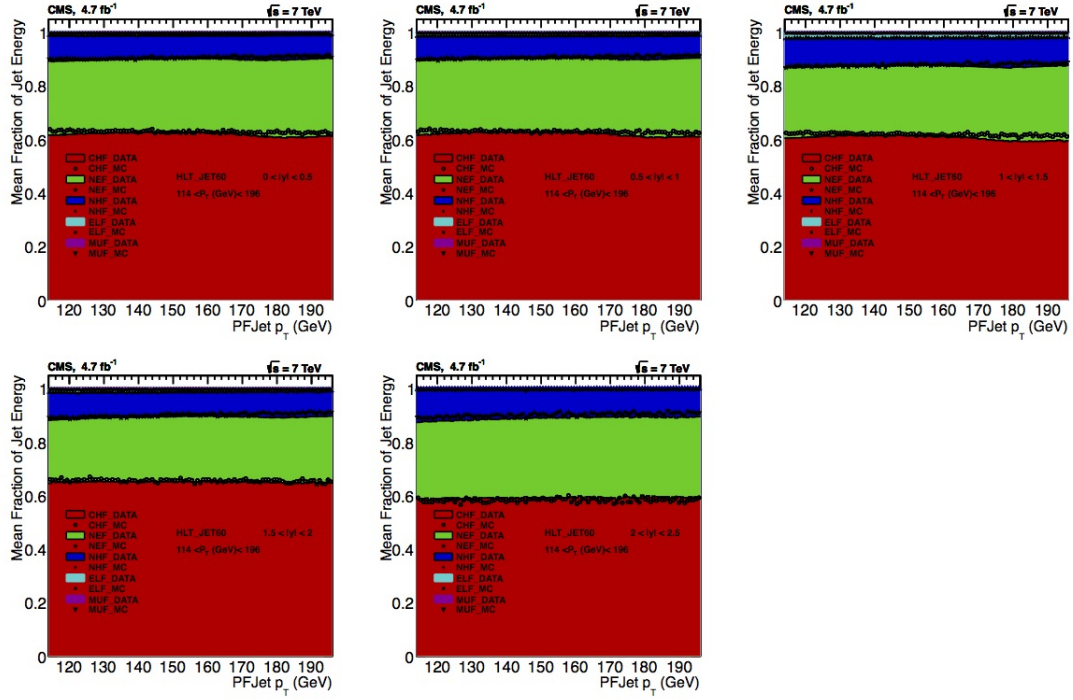


Figure 4.3: Distribution of the component fraction for JetHLT60 trigger with threshold $p_T > 114$ GeV in five eta region between DATA and MC inclusive PF_{jet} .

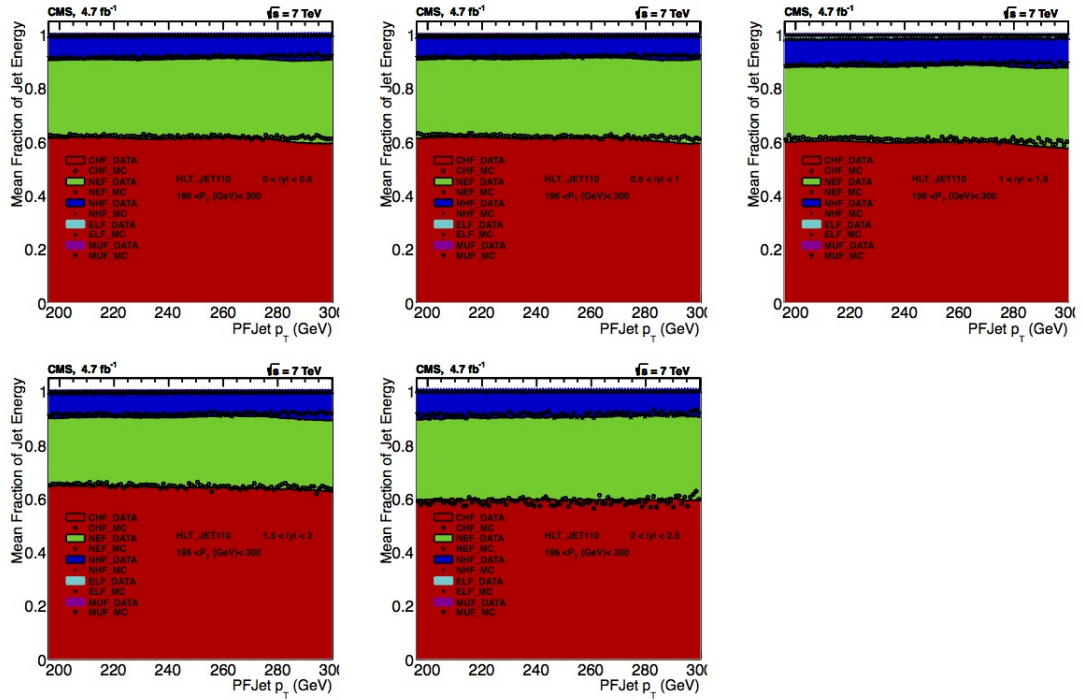


Figure 4.4: Distribution of the component fraction for JetHLT110 trigger with threshold $p_T > 196$ GeV.

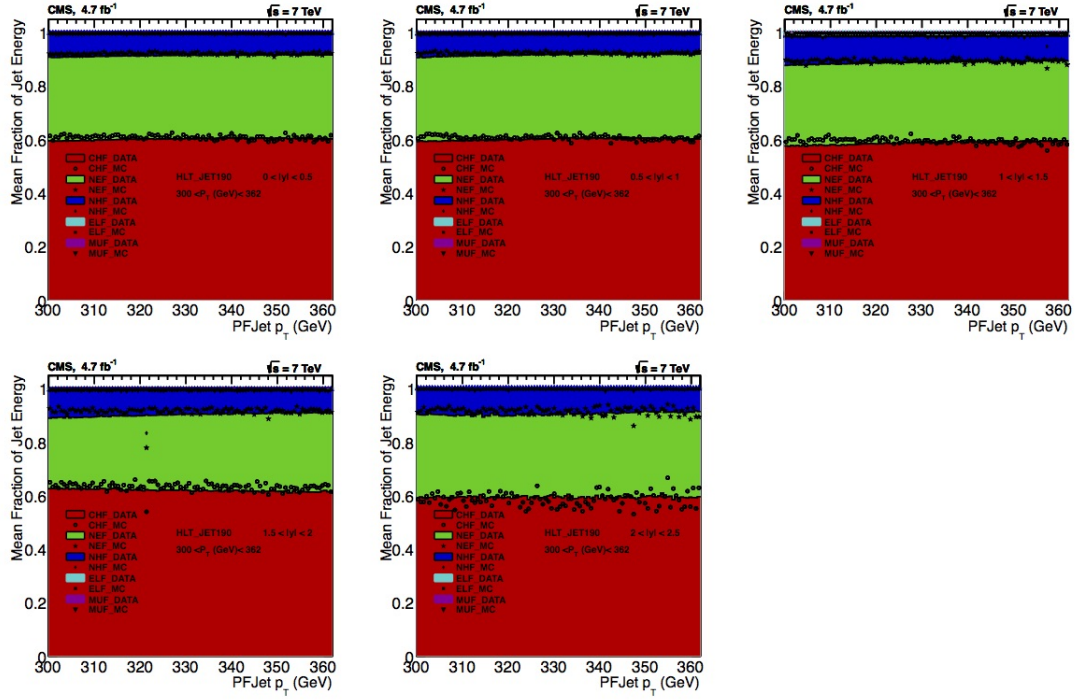


Figure 4.5: Distribution of the component fraction for JetHLT190 trigger with threshold $p_T > 300$ GeV.

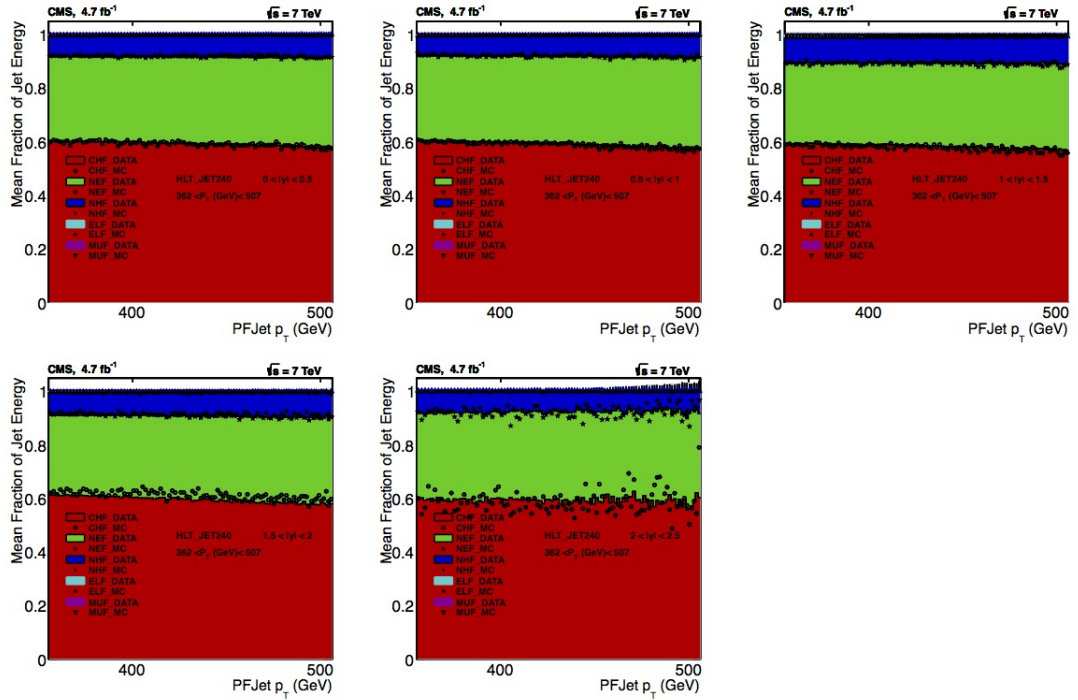


Figure 4.6: Distribution of the component fraction for JetHLT240 trigger with threshold $p_T > 362$ GeV.

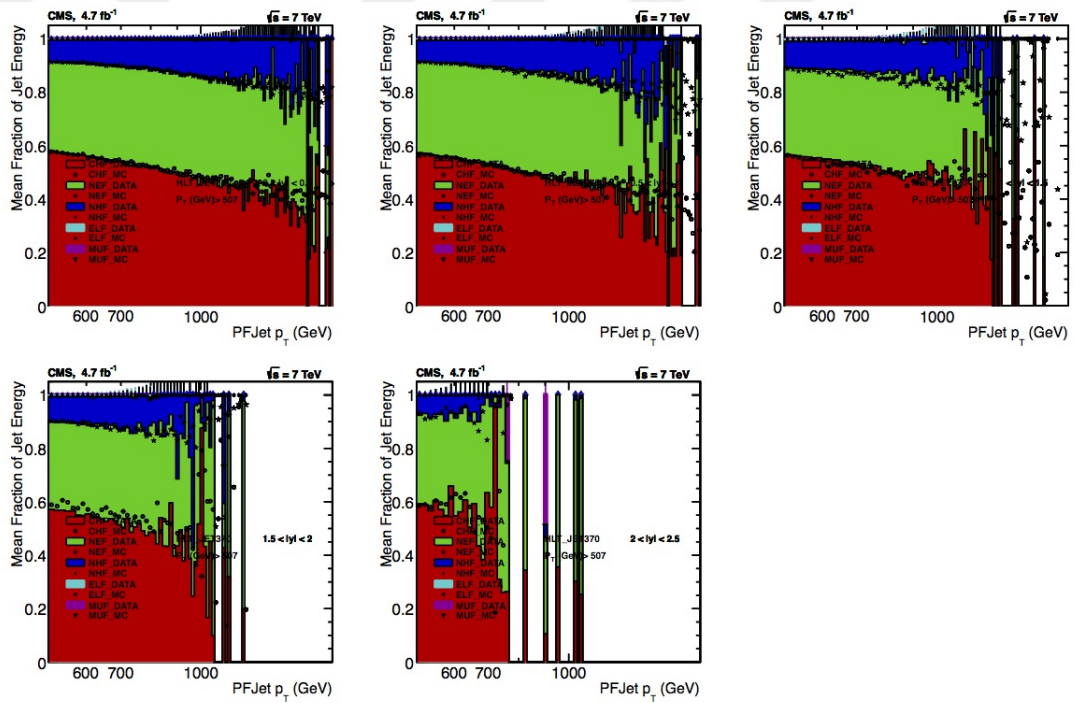


Figure 4.7: Distribution of the component fraction for JetHLT370 trigger with threshold $p_T > 507$ GeV.

4.3 Jet Energy Correction in The CMS Detector

The particles from proton-proton hard scattering collisions move through the CMS detector and leave their signals on the sub-detectors such as, trackers, ECAL and HCAL. Then these signals are reconstructed as a jet by using jet algorithms. More often measured energy of the particles is smaller than the corresponding energy at the particle level (so called true particles) because of the detector responses.

The purpose of the jet energy calibration (JEC) is to calibrate the measured energy of the jets from the detectors and bring it to particle level jet.

JEC is important for all the physics analysis in the experiment and also it is one of the important components of the systematic uncertainties. In the CMS experiment JEC is factorized in multi-level steps that are offset correction for subtracting electronic noise and pile-up from data, the residual relative correction (η dependent) for non-uniform variation of the jet response in η and the residual absolute correction (p_T dependent) for non-linear response in the calorimeters as a function of the jet p_T .

The offset, relative and absolute corrections which are explained in detail in the following sections can be extended with the optional correction by multiplying a factor such as electromagnetic correction and flavor correction. The electromagnetic fraction is optional correction for the variation of the jet response with electromagnetic fraction deposited by calorimeter, while the flavor correction is optional correction for the variation of the jet response with regard to different parton flavor such as b, c quarks and gluon[52]. Figure 4.8, shows the levels of jet energy calibration in the CMS detector.

The resulting jets require an additional energy correction to take into account the non-linear and non-uniform response of the CMS calorimetric system to the neutral-hadron component of the jet. In this thesis jet energy corrections are obtained by using generated events from PYTHIA6 (version 6.4.22)[53] and reconstructed events from GEANT4[54]. JEC version (GR_R_42_V22) as recommended by the JEC group is applied. By design JEC corrects reconstructed jets to the particle level. An offset correction is applied to take into account the extra energy clustered in jets due to

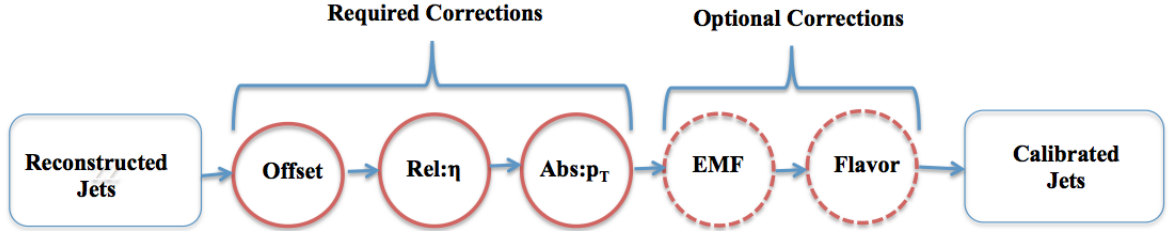


Figure 4.8: The illustration of the factorized jet energy corrections steps in the CMS detector. The jet energy correction factors are applied into reconstructed jets to obtain calibrated jets.

additional proton-proton interactions within the same or neighboring bunch crossings (in and out of time pile-up). Pile-up effects (10% jet energy scale correction and 1% systematic uncertainty) are only important for low p_T jets and almost vanish for jets with $p_T > 200$ GeV[55]. Hence they do not affect the inclusive jet analysis in this study since PF_{jet} with $p_T > 114$ GeV are selected. The jet-energy correction that depends on the η and p_T of the jet is applied as a multiplicative factor to the jet four-momentum vector. The multiplicative factor is in general smaller than 1.2 and, approximately uniform in η . For a jet with $p_T=100$ GeV, momentum factor decreases from 1.1 to 1.0 with increasing p_T . The typical jet p_T resolution is 10% at $p_T=100$ GeV.

4.3.1 Offset Correction

Offset correction aims to subtract excess energy from real multi p-p collisions due to electronic noise and pileup events. In order to obtain offset correction in the CMS, three different approaches are used: the jet area method, the average offset method, and the hybrid jet area method. The jet area method calculates average p_T density, ρ per unit area. This density characterizes combination of the underlying event, electronic noise and pileup for each event. The offset energy is obtained for jet-by-jet and event-by-event from the information of jet area and event density ρ . The average offset method measures average offset p_T due to pileup and electronic noise clustered

in a cone with radius R in $\eta - \phi$ space. Once again, the hybrid jet area method takes into account measurements of the offset energy as a function of η by taking note of average p_T density, ρ per unit area.

4.3.2 Relative Correction

The η dependence correction removes variation of the relative jet energy response and obtains a flat jet energy response as a function of η . For the relative response measurement, dijet balance technique accepted by the CMS is used. The technique is based on conservation of the transverse momentum in back to back dijet QCD events. This technique predicts that one of the jets has to be at the center of the detector (barrel jet), while another one has to be randomly in any η region (probe jet). Thus p_T balance is measured in back to back dijet events in azimuthal angle. The reason for selecting one of the jets in barrel region is that central region is uniform and the variation of the jet energy response is smaller than other detector regions.

4.3.3 Absolute Correction

The jet energy response in calorimeters changes as a function of jet p_T . The purpose of the absolute jet energy calibration is to remove the variation of the jet energy response as a function of p_T . For this reason absolute jet energy response is measured by using γ/Z +jets events with p_T balance technique and missing transverse energy projection fraction (MPF) method. The p_T balance technique has been explained in the previous section. Also MPF method is based on the fact that the γ/Z +jets events have no intrinsic missing E_T and at parton level, the γ or Z is perfectly balanced by the hadronic recoil in the transverse plane. In order to obtain the absolute energy calibration, jet energy response that is measured with both p_T balance technique and MPF method is extracted from MPF response. The reason for taking γ +jets and Z +jets events as a reference for absolute energy correction is that the energies of the γ and Z that decay into e^- and e^+ are measured from the ECAL and also the energy of the Z that decays into μ^+ and μ^- is measured precisely from trackers or muon detectors[55].

After combining the offset and relative correction, absolute p_T correction is also applied into jet to get the calibrated jets. Thus jets are corrected from detector level to particle level.

4.4 Jet Energy Resolution (JER)

In order to measure jet p_T resolution, p_T asymmetry method is used from the dijet events. The first two highest momentum jets (leading jets) are selected in events to calculate the asymmetry, A as

$$A = \frac{(p_T^{\text{jet1}} - p_T^{\text{jet2}})}{(p_T^{\text{jet1}} + p_T^{\text{jet2}})} \quad (4.3)$$

where p_T^{jet1} and p_T^{jet2} refer to the randomly ordered transverse momenta of the two leading jets. The variance of the asymmetry σ_A can be expressed as

$$\sigma_A^2 = \left| \frac{\partial A}{\partial p_T^{\text{jet1}}} \right|^2 \cdot \sigma^2(p_T^{\text{jet1}}) + \left| \frac{\partial A}{\partial p_T^{\text{jet2}}} \right|^2 \cdot \sigma^2(p_T^{\text{jet2}}), \quad (4.4)$$

and assuming $p_T \equiv p_T^{\text{jet1}} = p_T^{\text{jet2}}$ and $\sigma(p_T) \equiv \sigma(p_T^{\text{jet1}}) = \sigma(p_T^{\text{jet2}})$ for two leading jets in same rapidity region, the fractional jet p_T resolution is calculated to be

$$\frac{\sigma(p_T)}{p_T} = \sqrt{2}\sigma_A \quad (4.5)$$

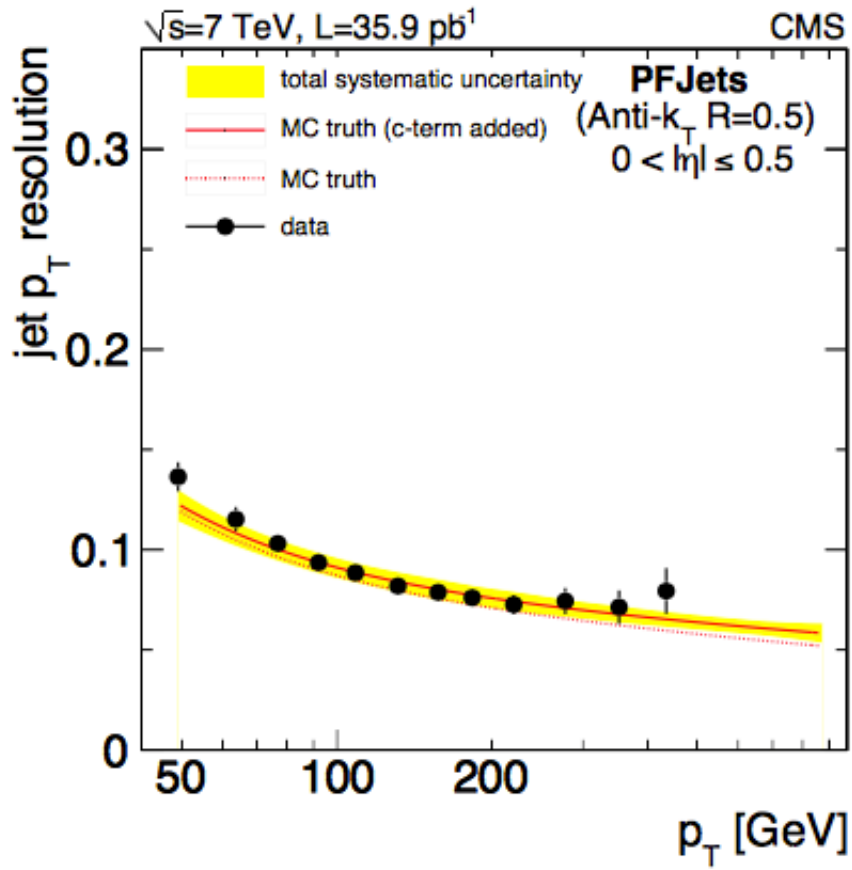


Figure 4.9: PF jet p_T resolution in $|\eta| < 0.5$ [55].

Jet energy resolution for particle flow jets is measured from dijet events using asymmetry method described above. As can be seen from Fig. 4.9 for PF jets in $|\eta| < 0.5$ with p_T of 100 GeV, the energy resolution is less than 10 %.

5. DATA ANALYSIS

5.1 Trigger Selection

The CMS trigger system is designed to control the recorded event rates consistent with available bandwidth. It consists of two parts, the level-1 trigger, (L1) and high-level trigger, (HLT), where the former one is mainly a hardware based trigger, where as the later one is a software based trigger. In this thesis the triggers used are single jet triggers such as L1SingleJet and HLT jet which forms the HLT jet trigger path. The integrated luminosity and average prescales of the HLT paths are given in Table 5.1. Note that jets used in the trigger paths are corrected for PF_{jet} reconstructed by anti- k_t with cone size $R = 0.7$.

Table 5.1: The integrated luminosity for each trigger paths.

Path	HLT Jet60	HLT Jet110	HLT Jet190	HLT Jet240	HLT Jet370
$L_{eff}(\text{pb}^{-1})$	0.4	6.9	145	496	4670
Average prescale	12084	672	32.1	9.4	1

The current 2011 data samples contain several jet triggers at the level of HLT which are presented in Table 5.2 along with the corresponding L1 triggers.

Table 5.2: HLT jet triggers and corresponding L1SingleJet trigger for the 2011 data sets.

L1SingleJet36	L1SingleJet68	L1SingleJet92	L1SingleJet92	L1SingleJet128
HLT Jet60	HLT Jet110	HLT Jet190	HLT Jet240	HLT Jet370

Because of the high rates of QCD events and existing limited bandwidths (~ 400 Hz) most of these trigger paths are subject to prescale factors. In addition, due to the high instantaneous luminosity in 2011 datasets, pile up may have sizable effects which in turn may affect the trigger efficiencies.

In order to avoid any trigger bias additional p_T thresholds are required for the jet selection. This trigger thresholds that are given in Table 5.3 are determined using the turn on point of the trigger efficiency which is the ratio of the lower threshold single-jet trigger and single-muon triggers. Figure 5.1 shows the trigger efficiency as a functions p_T for the central rapidity region, $|y| < 0.5$ and highest trigger threshold.

Table 5.3: HLT jet trigger thresholds.

Path	HLT Jet60	HLT Jet110	HLT Jet190	HLT Jet240	HLT Jet370
$p_T(\text{GeV})$	114	196	300	362	507

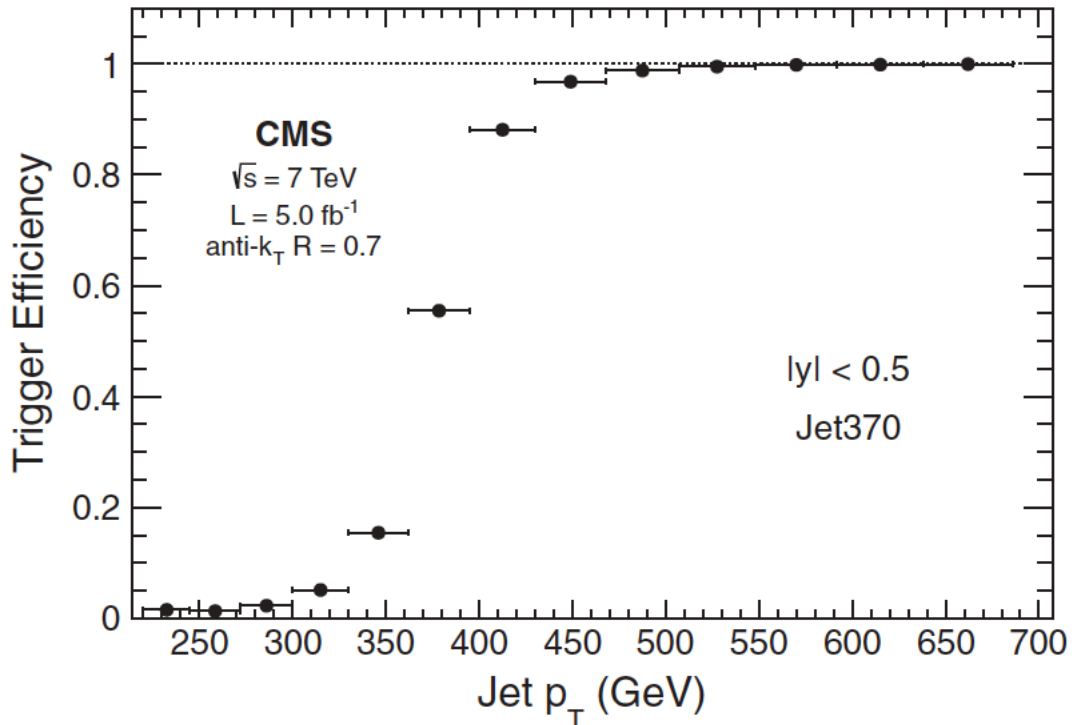


Figure 5.1: HLT single jet trigger efficiency.

5.2 Event Selection

Even though the CMS experiment has a hermitic structure to observe all the visible particles that interacts strongly and electromagnetically with matter, it misses out some weakly interacting neutral particles such as neutrinos.

5.2.1 Missing Energy

In the data it is not possible to observe the missing transverse energy, E_T^{miss} . On the other hand MC simulations estimate the E_T^{miss} using unbalanced summed transverse momentum (p_T) coming from the hard scattered visible particles that were obtained by using full detector information. There is also “fake” E_T^{miss} that occurs due to the detector effects such as, detector noise, cosmics, ..., etc.

In this study, E_T^{miss} is derived from reconstructed particle flow events using MC simulation. Figure 5.2 shows distribution of $E_T^{\text{miss}}/\Sigma E_T$ for both MC and data events before applying event selection criteria cut $E_T^{\text{miss}}/\Sigma E_T < 0.3$.

E_T^{miss} defined below represents the sum of the missing transverse energy vector which is calculated by independent calorimeter towers with E_i energy corresponding to η_i pseudo rapidity and ϕ_i azimuthal angle;

$$\vec{E}_T^{\text{miss}} = -\sum_i (E_i \sin\theta_i \cos\phi_i \hat{x} + E_i \sin\theta_i \sin\phi_i \hat{y}) \quad (5.1)$$

where \hat{x} and \hat{y} are the unit vectors in the direction of x and y axis and ΣE_T represents sum of the scalar transverse energy in the calorimeter towers in an event: $\Sigma E_T = \sum_i E_{Ti}$, where $E_{Ti} = E_i \sin\theta_i$.

It can be seen from Fig. 5.2 that the tail for MC and data are different which may come from the process such as Z+jet(s). Moreover the tail in data events are interesting for studies beyond the standard model physics that include some models for dark matter and extra dimensions. In order to remove this tail in data events and to reject detector effects such as noise, the $E_T^{\text{miss}}/\Sigma E_T < 0.3$ upper limit cut is applied as an event selection criteria. The hard QCD processes do not produce fake

E_T^{miss} because of the good energy resolution. And also, E_T^{miss} values calculated in the event are very small compared to the ΣE_T .

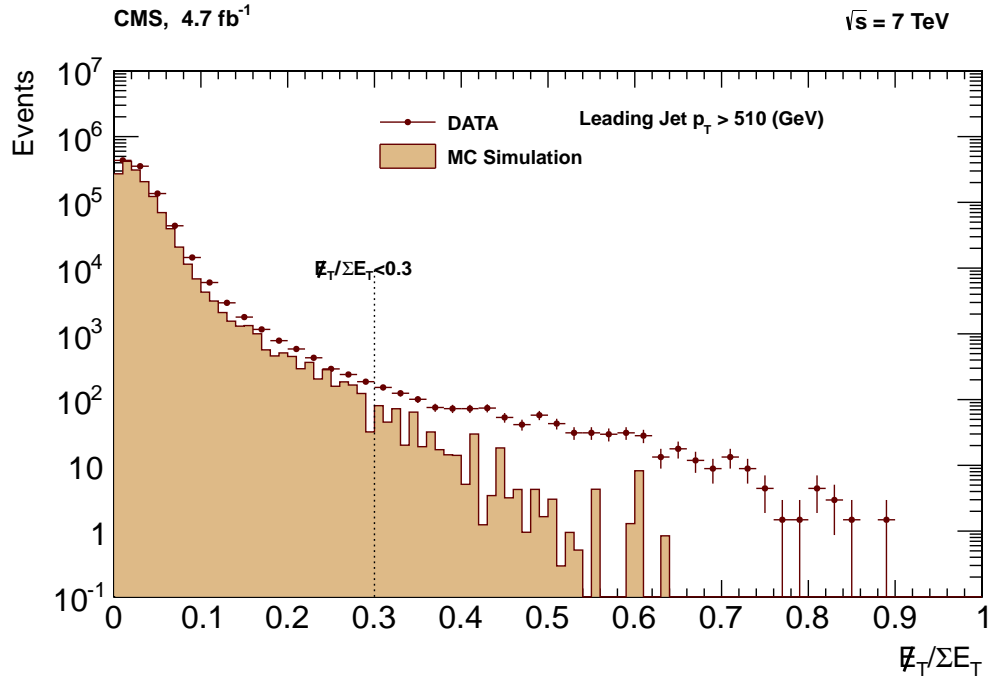


Figure 5.2: Distribution of $E_T^{\text{miss}} / \Sigma E_T$ for both the data and MC simulations with leading Jet $p_T > 510$ GeV. Red points represent data events and filled area with camel color represents the MC simulation events.

5.2.2 Vertex Quality Cut

The Vertices are required to distinguish between “real” jets, which come from hard scattering collisions, and “fake” jets, which come from detector background (beam halo, noise). Tracking information is required to identify cosmic beam in the data events and to reduce the beam background from the data. When particles are reconstructed, they use the energy clusters. To get a “good” reconstructed jet from the energy clusters, the kinematic of the clusters for each calorimeter are reconstructed by using primary vertices. Thus, the additional E_T which comes from detector background in the calorimeter towers is measured as a function of η and number of reconstructed primary vertex, N_{PV} , and subtracted from “real” jets. Each selected event has to have at least one primary vertex with $|z(PV)| < 24$ cm and have to have at least four tracks considered in the vertex fit $n_{dof}(PV) \geq 5.0z(PV)$. In addition, selected events have to have at least two reconstructed PF_{jet} with $p_T > 30$ GeV for $|\eta| < 2.5$. Then, the events are redefined as a four-vector sum of the clusters and assigned a specific trigger.

Average energy fractions as a function of number of vertices for charged hadrons, neutral hadrons and photons are shown in Figs. 5.3-5.7 for different triggers, p_T and five rapidity regions. Electromagnetic and charge fraction distributions show identical behavior for each HLT triggers in different rapidity regions.

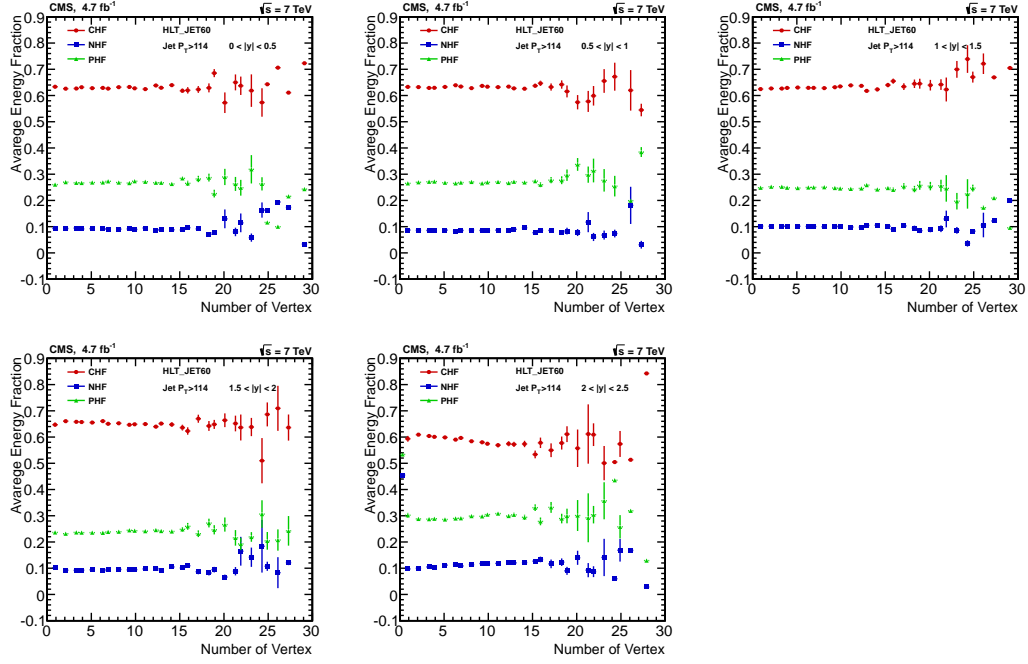


Figure 5.3: Average energy fraction vs number of vertex for JetHLT60 trigger for different rapidity bin region for $p_T > 114$ GeV in five η region. The red full circles represent charge hadron fraction, blue full squares represent neutral hadron fractions, and green full triangles represent photon hadronic fractions distributions.

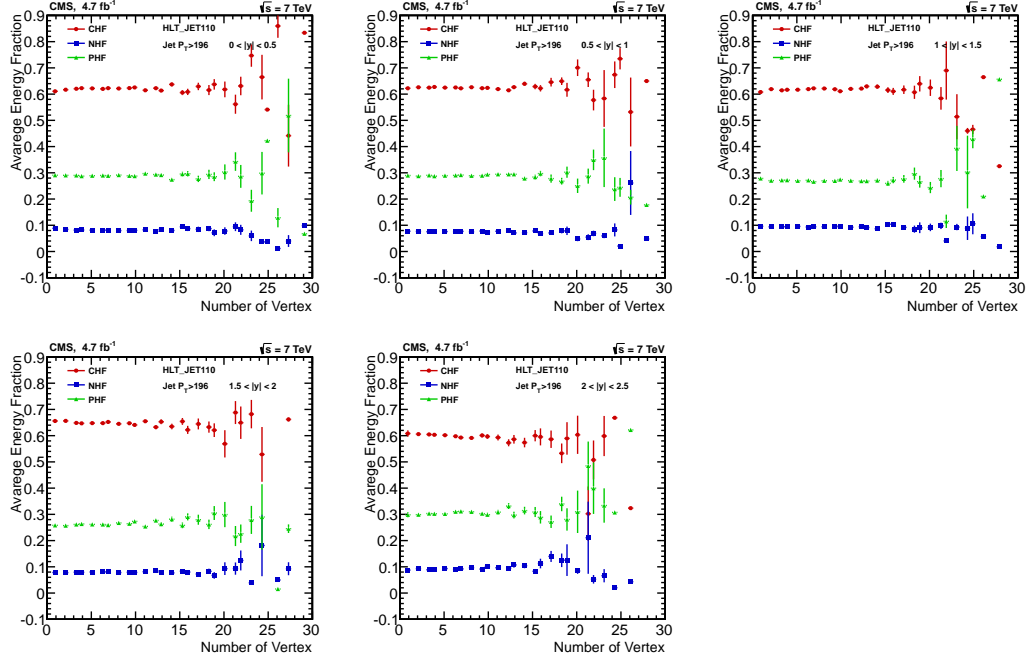


Figure 5.4: Average energy fraction vs number of vertex for JetHLT110 trigger for different rapidity bin regions for $p_T > 196$ GeV.

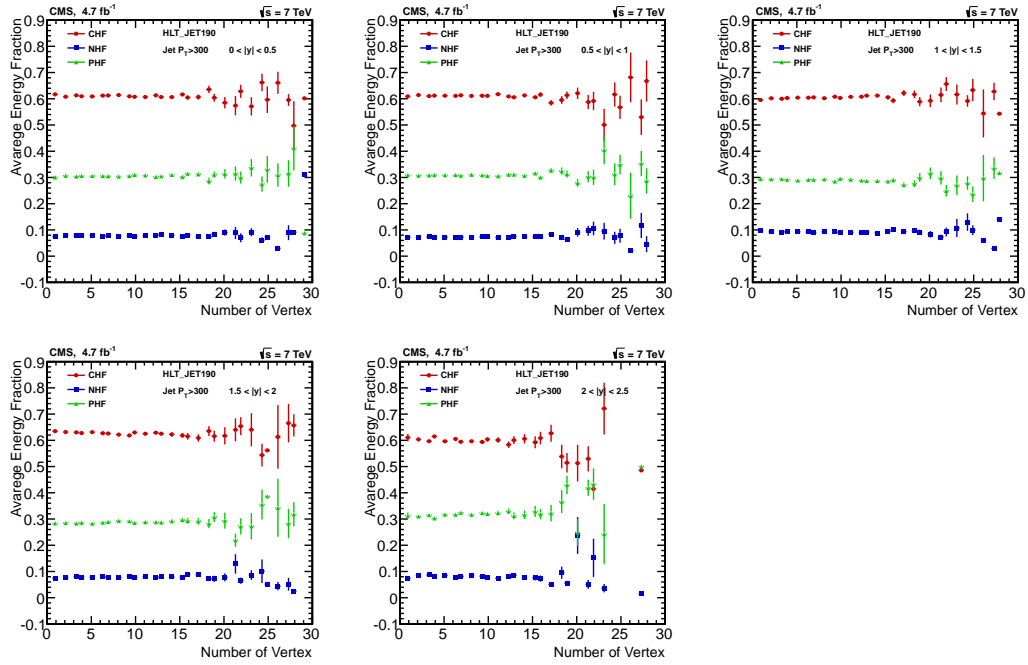


Figure 5.5: Average energy fraction vs number of vertex for JetHLT190 trigger for different rapidity bin regions for $p_T > 300$ GeV.

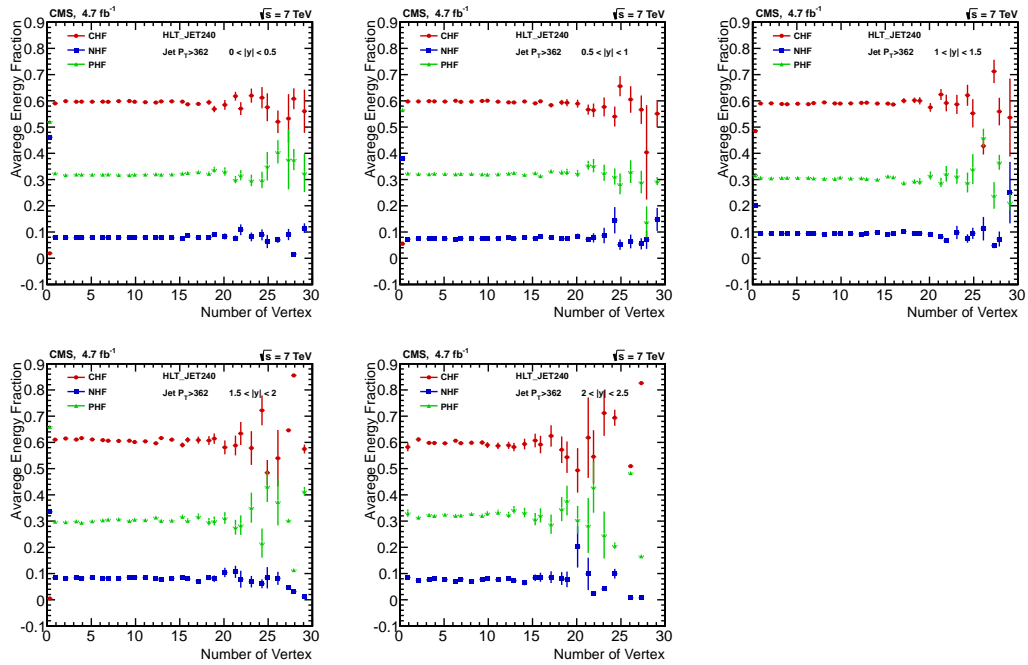


Figure 5.6: Average energy fraction vs number of vertex for JetHLT240 trigger for different rapidity bin regions for $p_T > 362$ GeV.

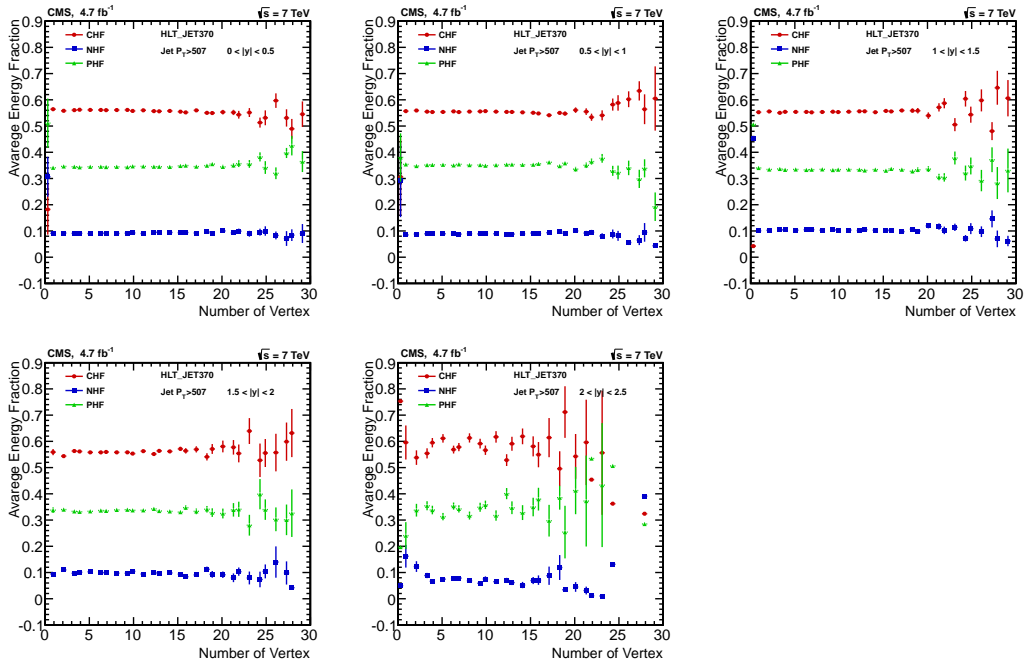


Figure 5.7: Average energy fraction vs number of vertex for JetHLT370 trigger for different rapidity bin regions for $p_T > 507$ GeV.

5.2.3 Good Run Selection

The data events are collected from runs recorded by the CMS detector. Each run has a certain prescale factor and luminosity value. It is important that “a good” run obtained from events has to have at least one primary vertex. Then each event has to satisfy the conditions set by corresponding software trigger. Figures 5.8 - 5.12 show jet component fractions which pass from different software trigger in five rapidity regions for every run. It can be seen from Figs. 5.8 - 5.12 that for every different trigger the energy of the component fractions, behave smoothly in five rapidity regions.

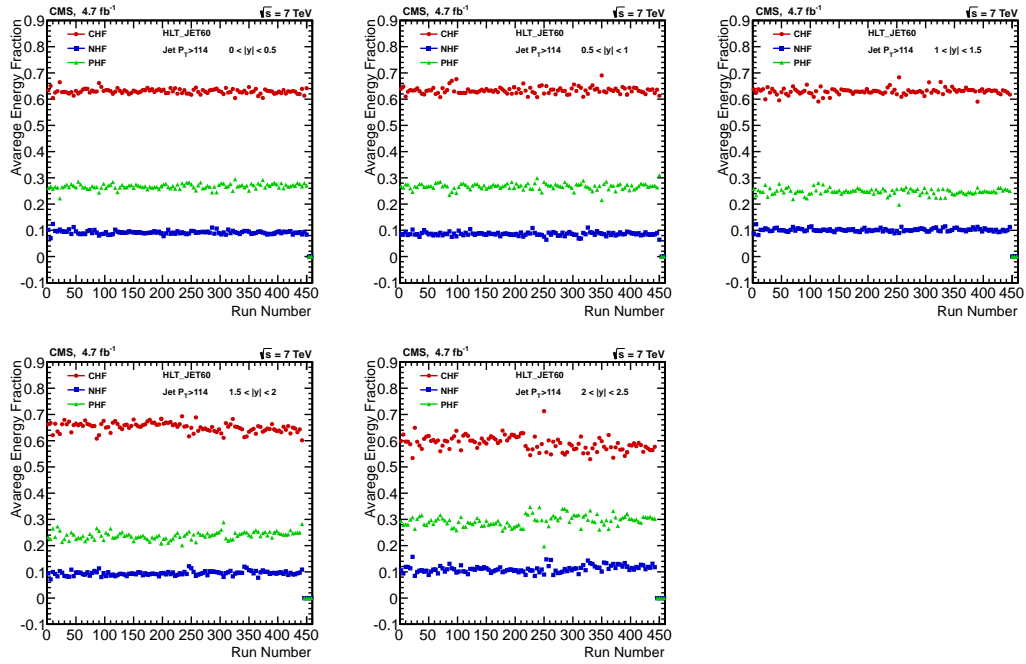


Figure 5.8: Distribution of the jet component fractions versus run numbers for JetHLT60 trigger with threshold $p_T > 114$ GeV in five rapidity bins. Here the red circles, green triangle and, blue square represent charged hadronic fraction, photon fraction and, neutral hadronic fraction respectively.

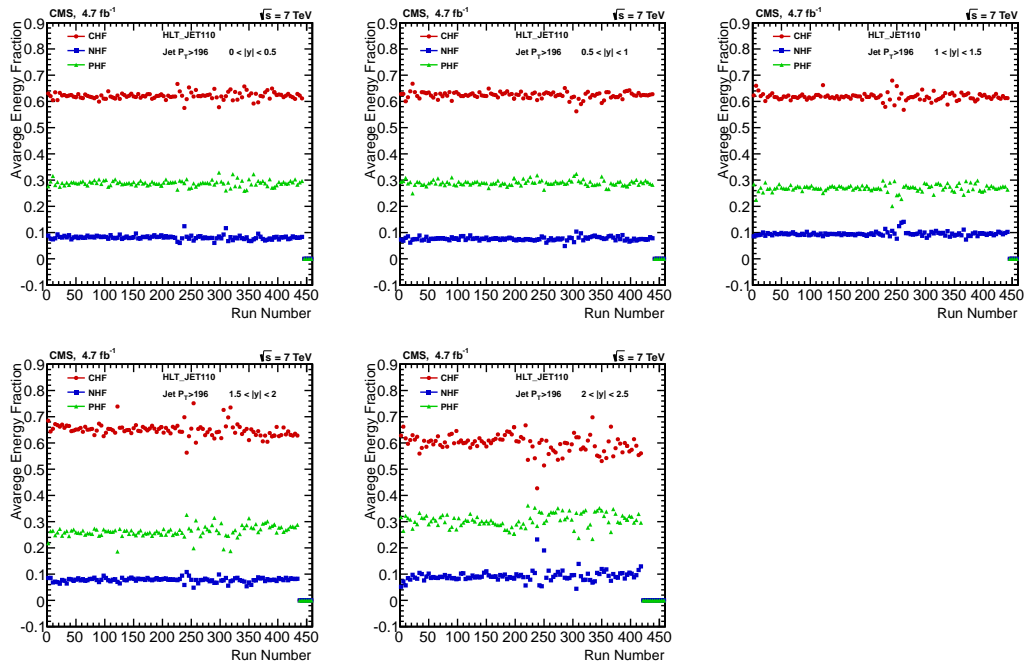


Figure 5.9: Distribution of the jet component fractions versus run numbers for JetHLT110 trigger with threshold $p_T > 196$ GeV in five rapidity bins.

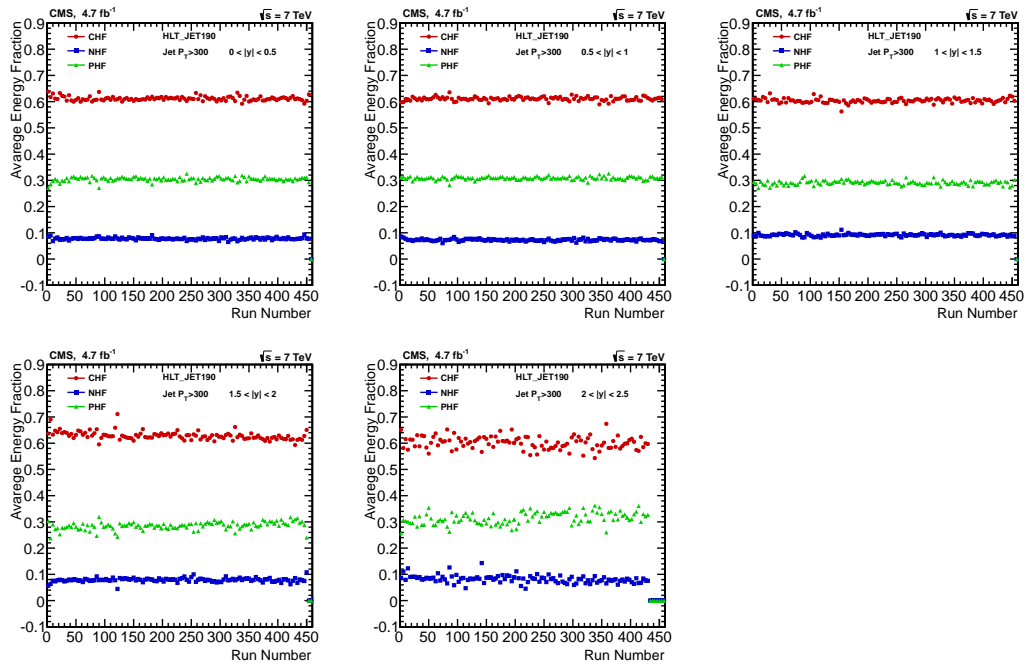


Figure 5.10: Distribution of the jet component fractions versus run numbers for JetHLT190 trigger with threshold $p_T > 300$ GeV in five rapidity bins.

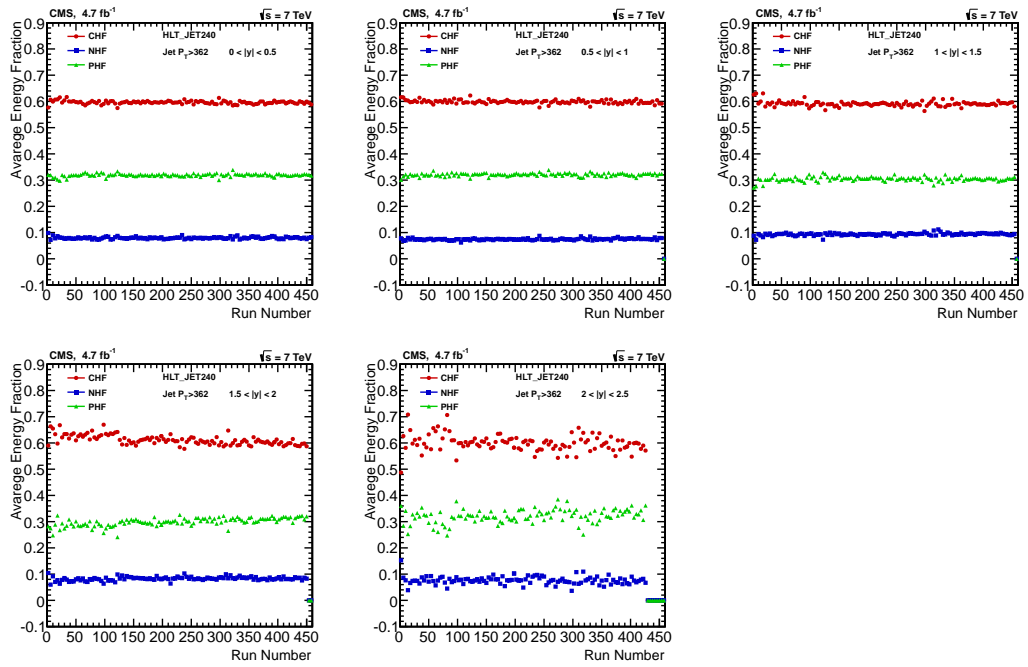


Figure 5.11: Distribution of the jet component fractions versus run numbers for JetHLT240 trigger with threshold $p_T > 362$ GeV in five rapidity bins.

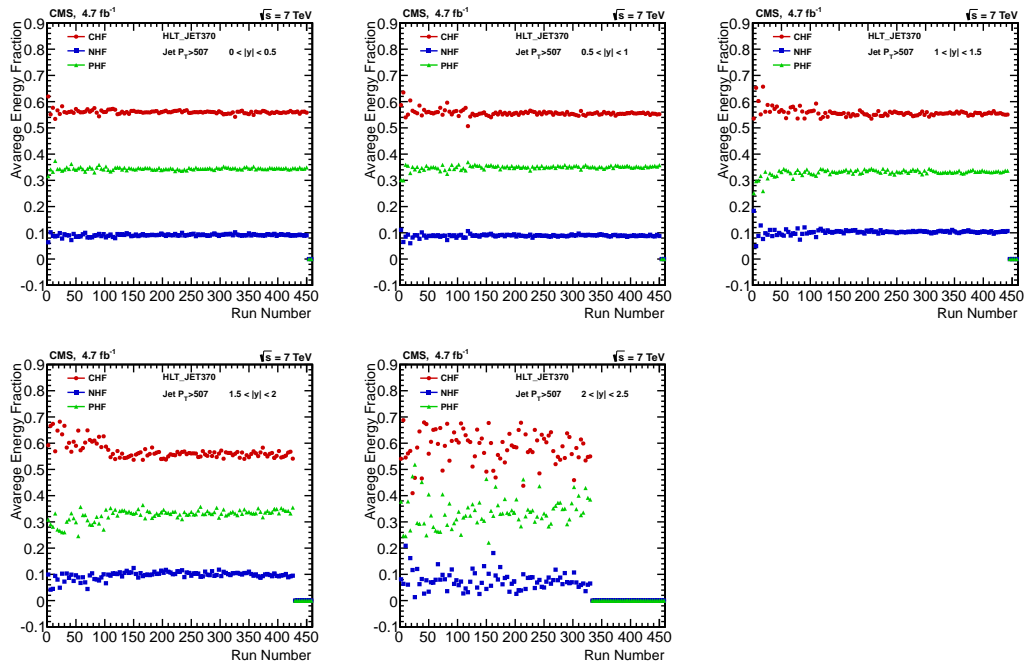


Figure 5.12: Distribution of the jet component fractions versus run numbers for JetHLT370 trigger with threshold $p_T > 507$ GeV in five rapidity bins.

5.3 Jet Identification

In the inclusive jet measurement to remove the noise (nonphysical jets) at detector level, the jets are selected with the “tight” jet identification with $p_T > 114$ GeV, 196 GeV, 300 GeV, 362 GeV, and 507 GeV for the five single-jet HLT triggers used respectively. Tight jet selection is done with following criteria:

- at least two PF particles
- at least one charged hadron with charged hadron fraction, $CHF > 0$
- neutral hadron fraction (NHF) carried by neutral hadron should be less than 90%,
 $NHF < 0.9$
- neutral electromagnetic fraction (NEF) carried by photon should be less than 90%,
 $NEF < 0.9$

Figures 5.13-5.27 show the distributions of DATA and MC events for charged hadron, neutral hadron and, photon energy fraction passed from five HLT triggers in five rapidity region. The plots show a reasonable competency between DATA and MC distributions for the inclusive jet events.

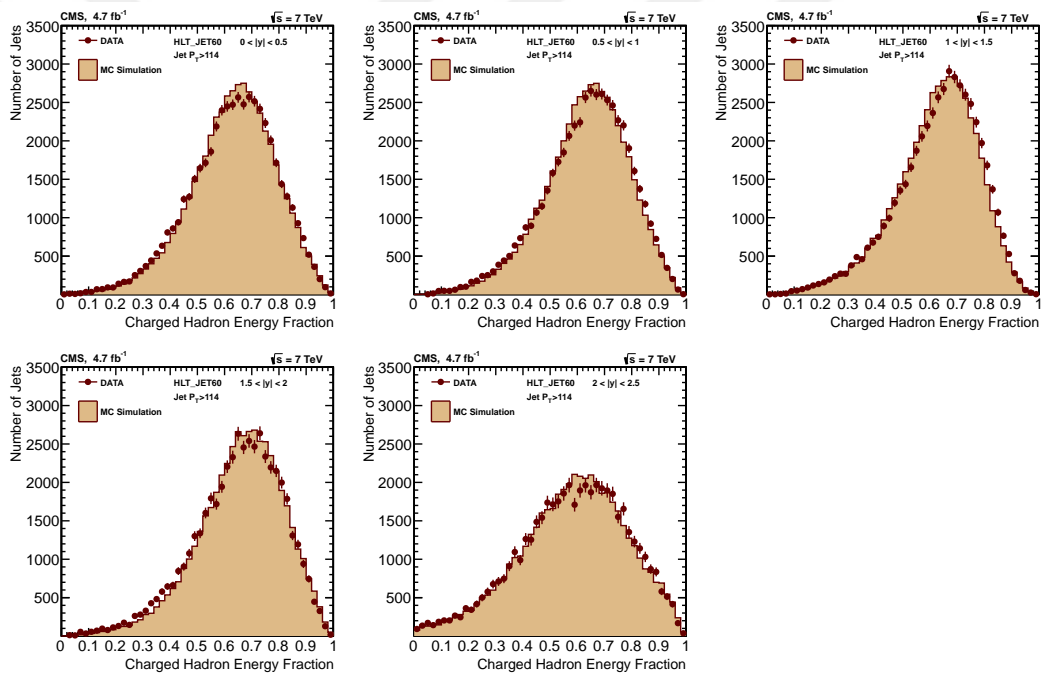


Figure 5.13: Comparison of the charged hadron energy fraction for JetHLT60 trigger with threshold $p_T > 114$ GeV in five rapidity bins between DATA and MC inclusive jet events. Red points represent data events and filled area with camel color represents the MC simulation events.

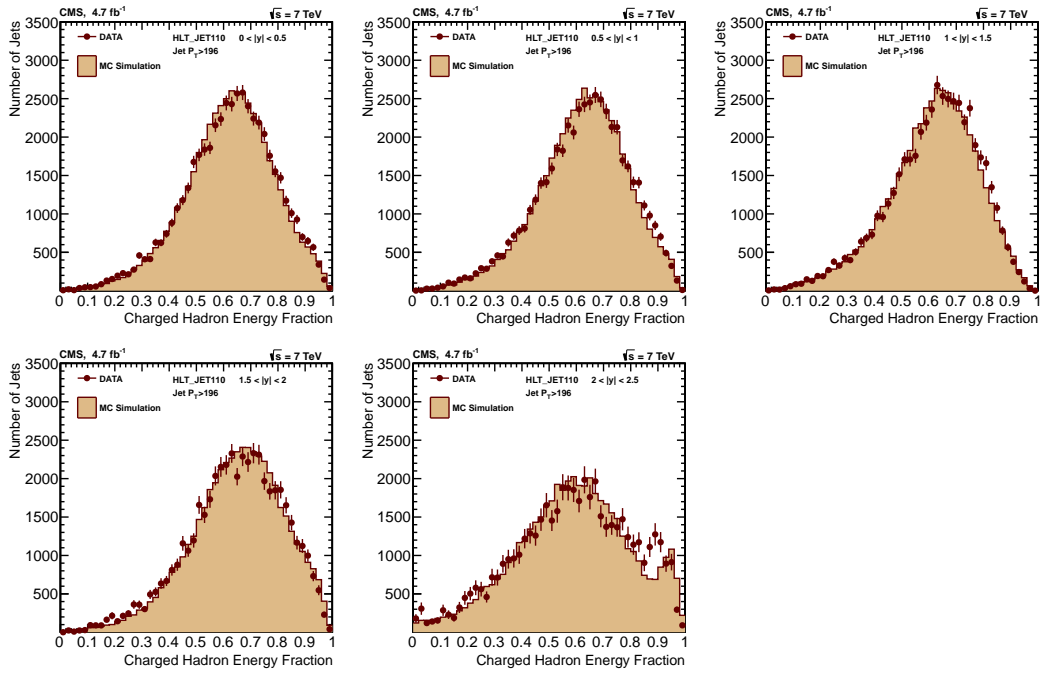


Figure 5.14: Comparison of the charged hadron energy fraction for JetHLT110 trigger with threshold $p_T > 196$ GeV in five rapidity bins between DATA and MC inclusive jet events.

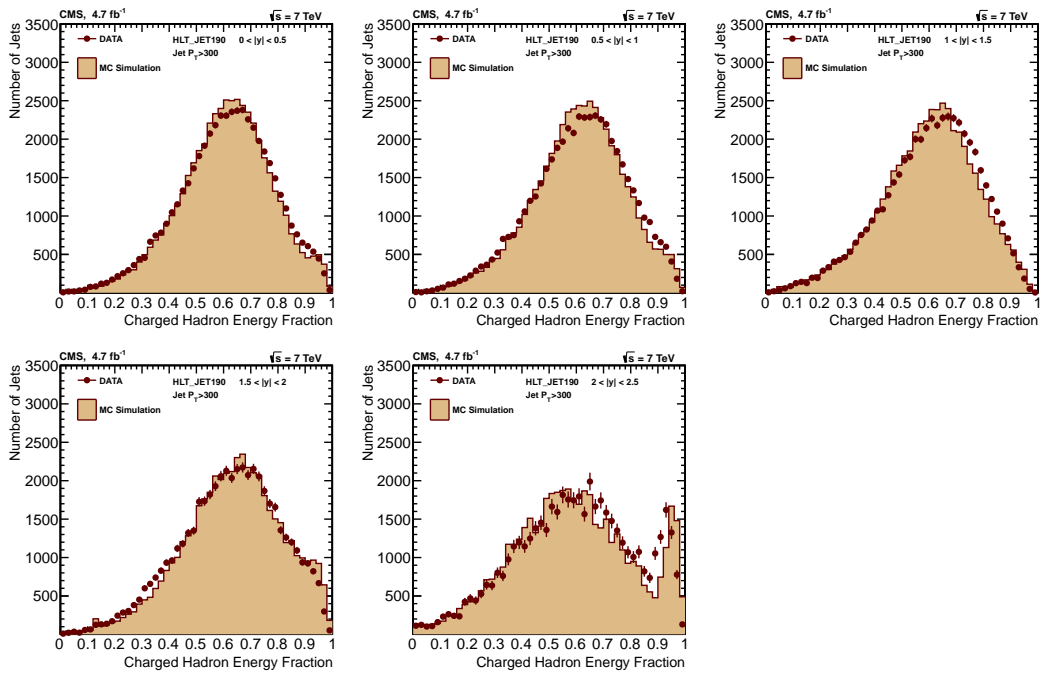


Figure 5.15: Comparison of the charged hadron energy fraction for JetHLT190 trigger with threshold $p_T > 300$ GeV in five rapidity bins between DATA and MC inclusive jet events.

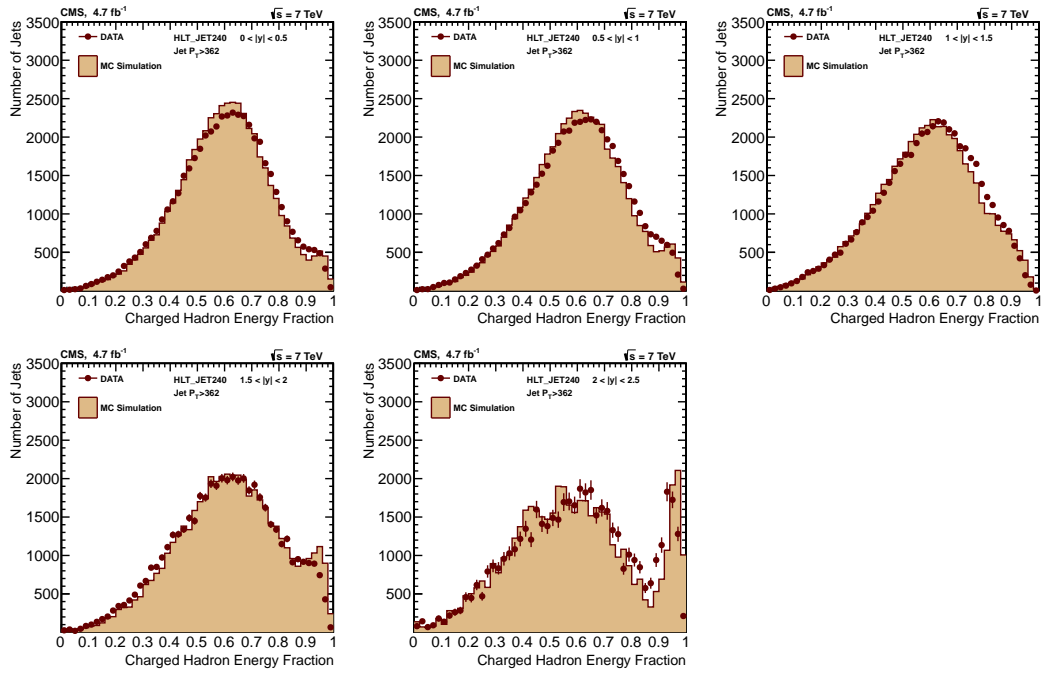


Figure 5.16: Comparison of the charged hadron energy fraction for JetHLT240 trigger with threshold $p_T > 362$ GeV in five rapidity bins between DATA and MC inclusive jet events.

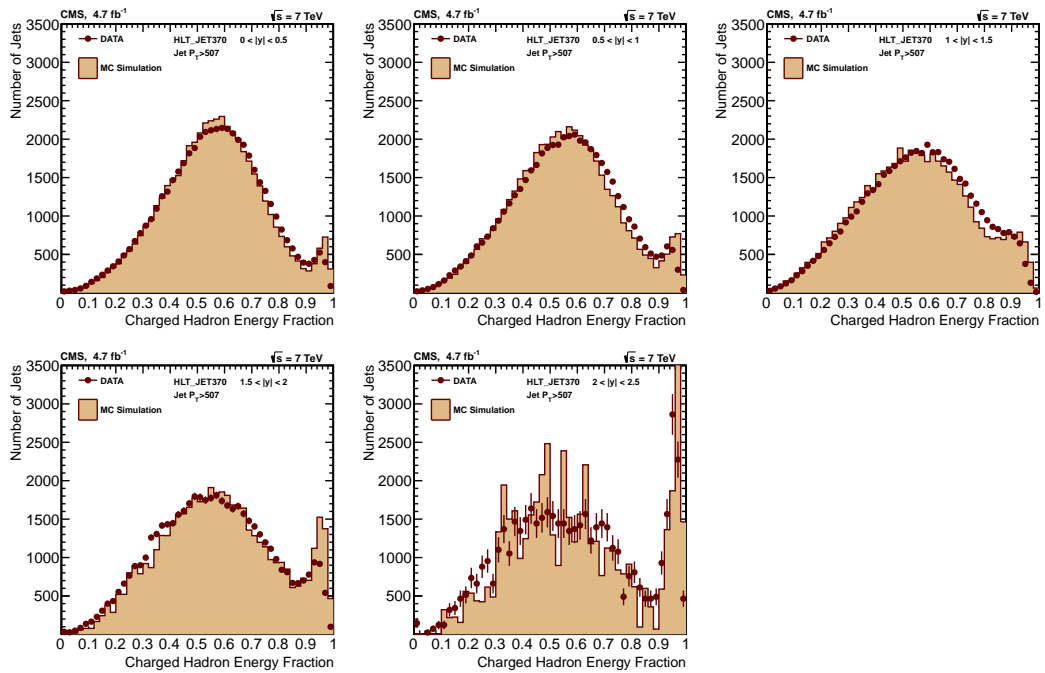


Figure 5.17: Comparison of the charged hadron energy fraction for JetHLT370 trigger with threshold $p_T > 507$ GeV in five rapidity bins between DATA and MC inclusive jet events.

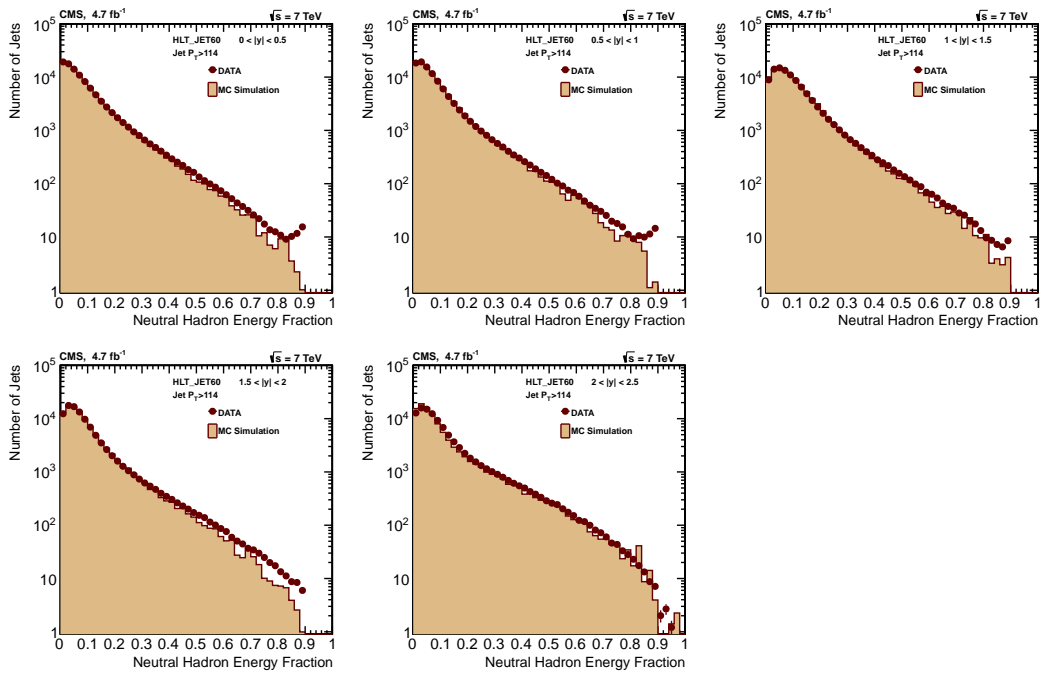


Figure 5.18: Comparison of the neutral hadron energy fraction for JetHLT60 trigger with threshold $p_T > 114$ GeV in five rapidity bins between DATA and MC inclusive jet events.

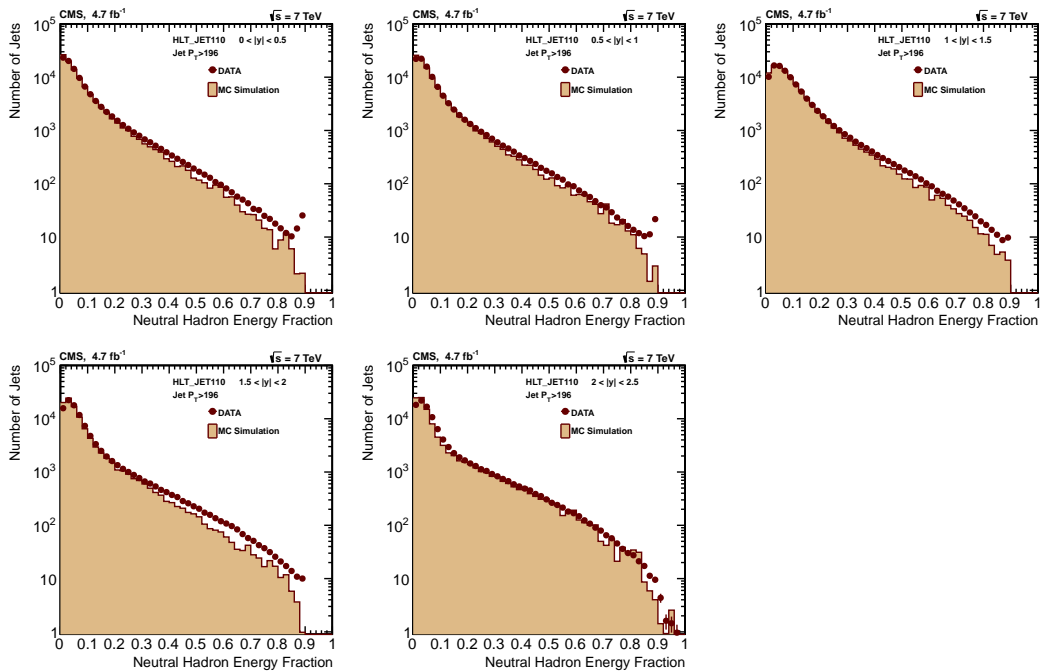


Figure 5.19: Comparison of the neutral hadron energy fraction for JetHLT110 trigger with threshold $p_T > 196$ GeV in five rapidity bins between DATA and MC inclusive jet events.

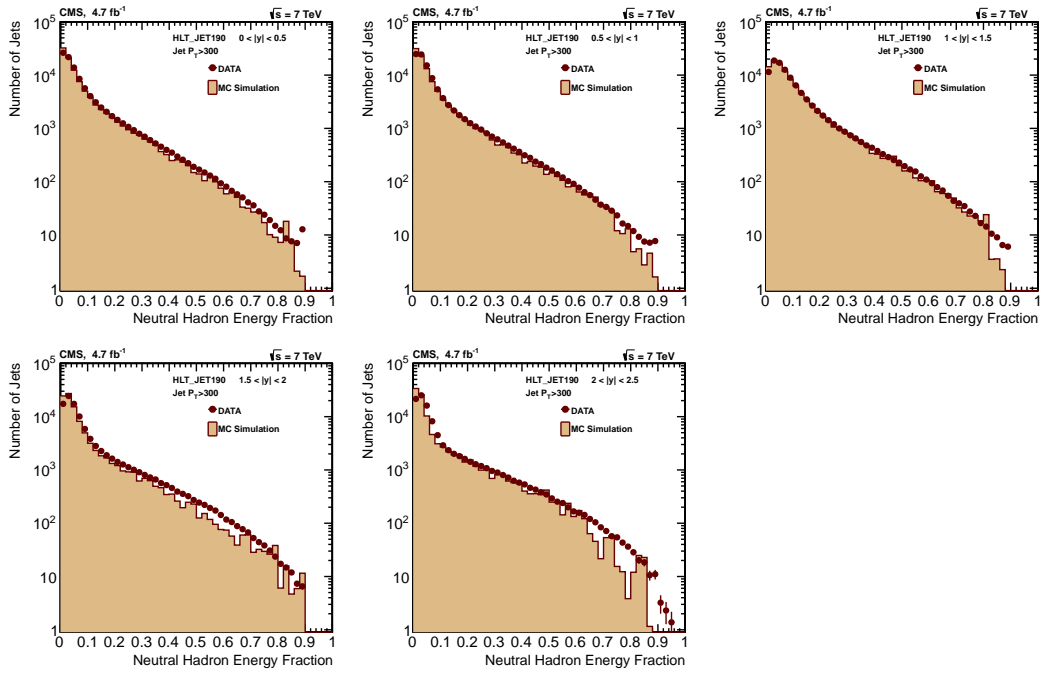


Figure 5.20: Comparison of the neutral hadron energy fraction for JetHLT190 trigger with threshold $p_T > 300$ GeV in five rapidity bins between DATA and MC inclusive jet events.

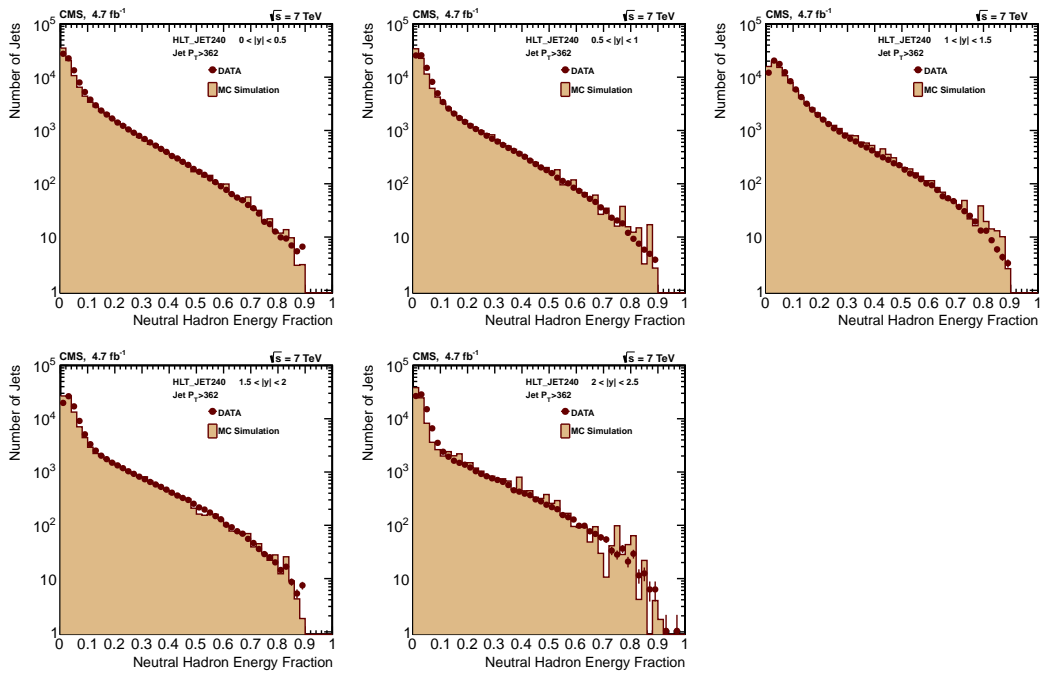


Figure 5.21: Comparison of the neutral hadron energy fraction for JetHLT240 trigger with threshold $p_T > 362$ GeV in five rapidity bins between DATA and MC inclusive jet events.

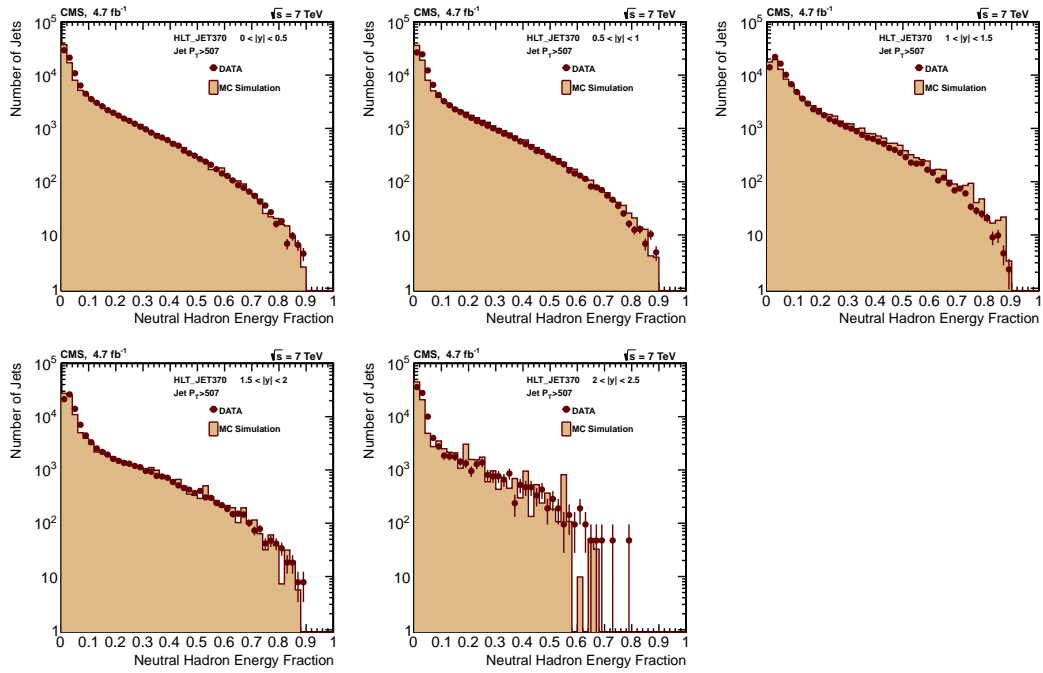


Figure 5.22: Comparison of the neutral hadron energy fraction for JetHLT370 trigger with threshold $p_T > 507$ GeV in five rapidity bins between DATA and MC inclusive jet events.

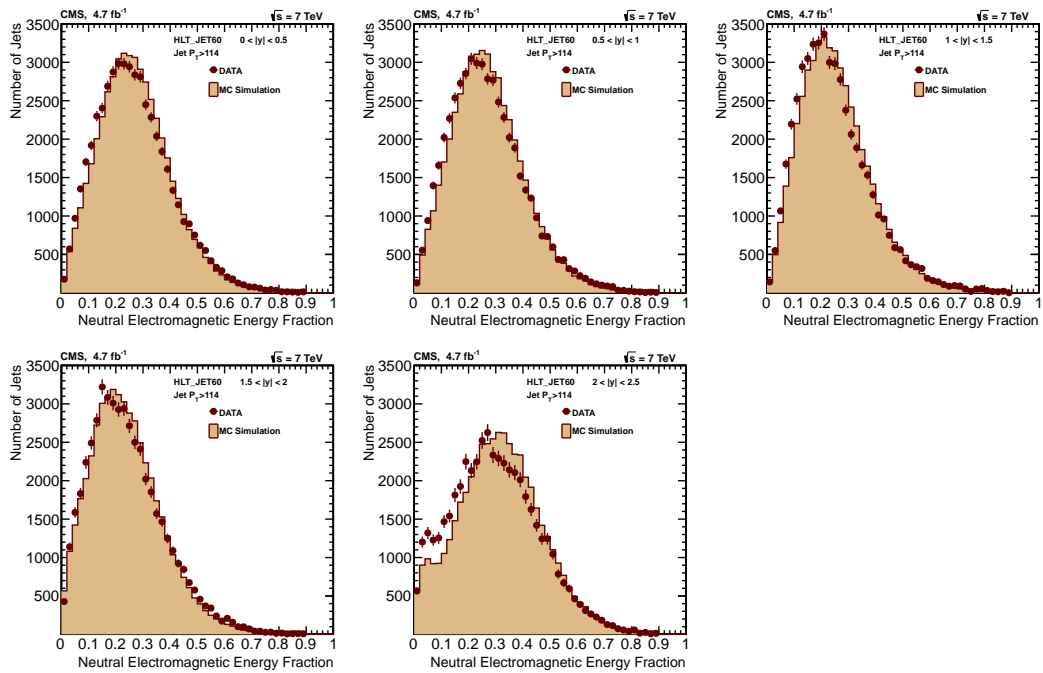


Figure 5.23: Comparison of the neutral electromagnetic (photon) energy fraction for JetHLT60 trigger with threshold $p_T > 114$ GeV in five rapidity bins between DATA and MC inclusive jet events.

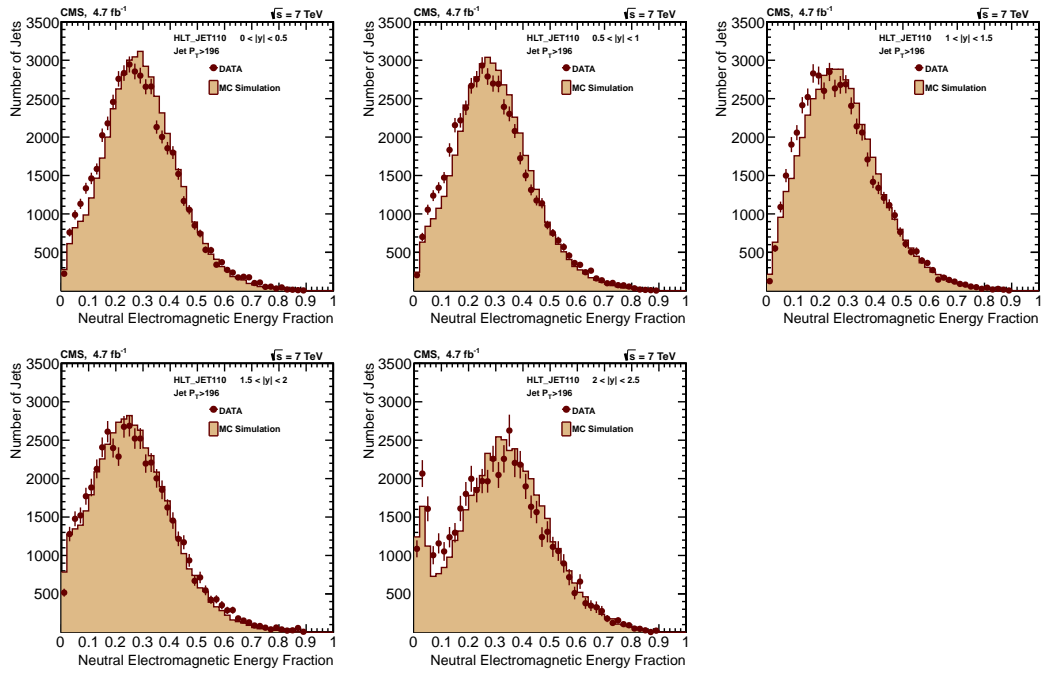


Figure 5.24: Comparison of the neutral electromagnetic (photon) energy fraction for JetHLT110 trigger with threshold $p_T > 196$ GeV in five rapidity bins between DATA and MC inclusive jet events.

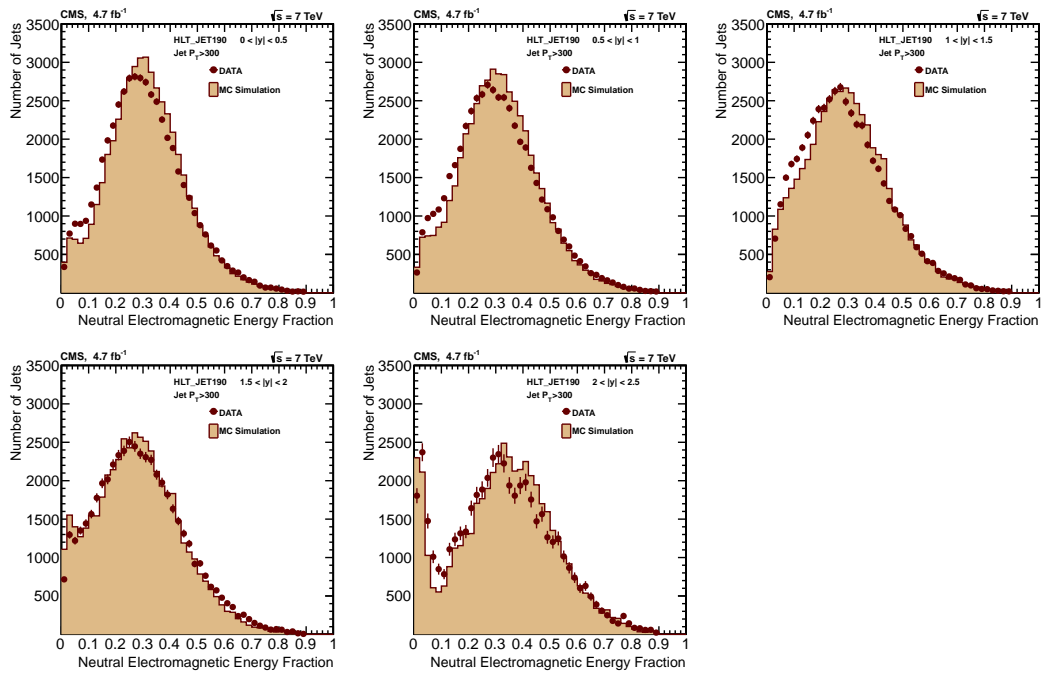


Figure 5.25: Comparison of the neutral electromagnetic (photon) energy fraction for JetHLT190 trigger with threshold $p_T > 300$ GeV in five rapidity bins between DATA and MC inclusive jet events.

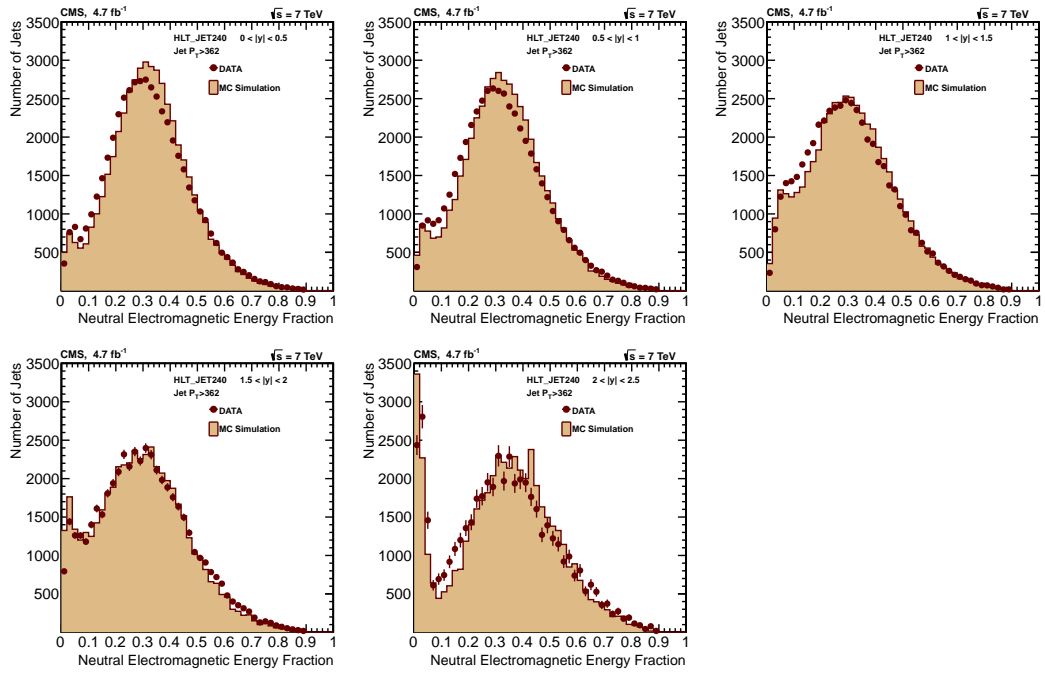


Figure 5.26: Comparison of the neutral electromagnetic (photon) energy fraction for JetHLT240 trigger with threshold $p_T > 362$ GeV in five rapidity bins between DATA and MC inclusive jet events.

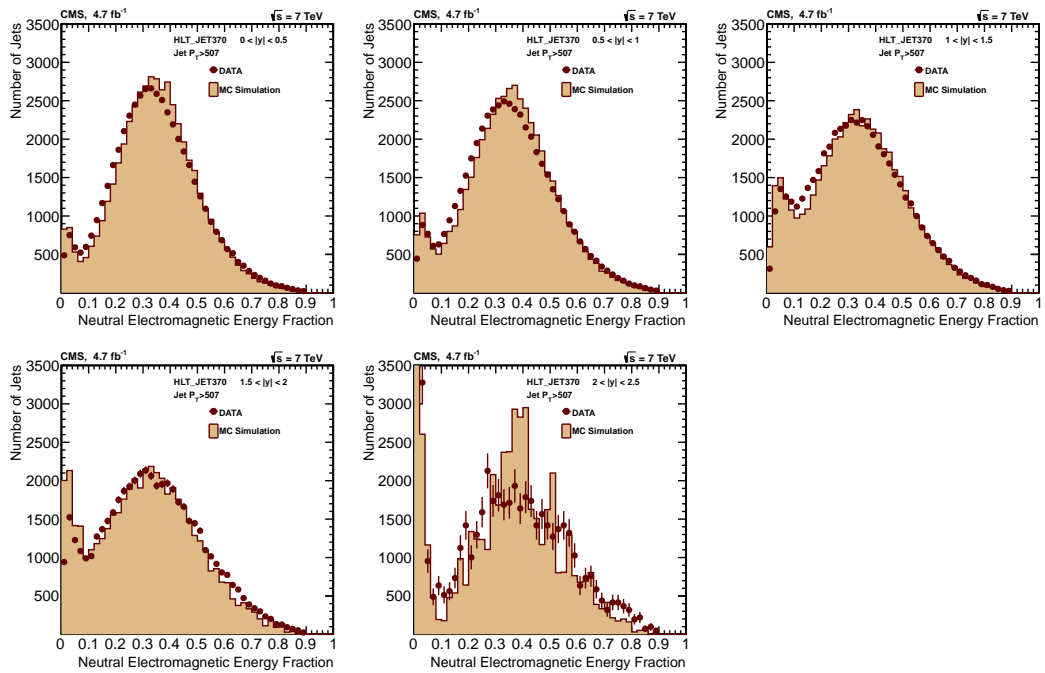


Figure 5.27: Comparison of the neutral electromagnetic (photon) energy fraction for JetHLT370 trigger with threshold $p_T > 507$ GeV in five rapidity bins between DATA and MC inclusive jet events.

5.3.1 Jet Identification (Jet ID) Efficiency

As we described at the previous section, one of the jet selection criteria is “tight” jet id. Jet ID efficiency is obtained with “tag” and “probe” method by using dijet events that require two highest transverse momentum jets, so called leading jets. The dijet events require to be back-to-back in azimuthal plane ($\Delta\phi > 2.7$) and to have inclusive jet event with $p_T > 114$ GeV. According to “tag” and “probe” jet method, one jet is selected randomly as a “tag” jet, which must satisfy all the jet selection criteria. Another jet is selected as a “probe” jet, which requires no further cuts. Thus, the jet ID efficiency is defined as the ratio of tag jets over the probe jets in dijet events. Figure 5.28 shows distribution of the jet ID efficiency versus probe jet p_T in five rapidity regions. Each color represents different trigger range with different p_T threshold. The jet ID efficiency is close to 100% in different rapidity regions as expected.

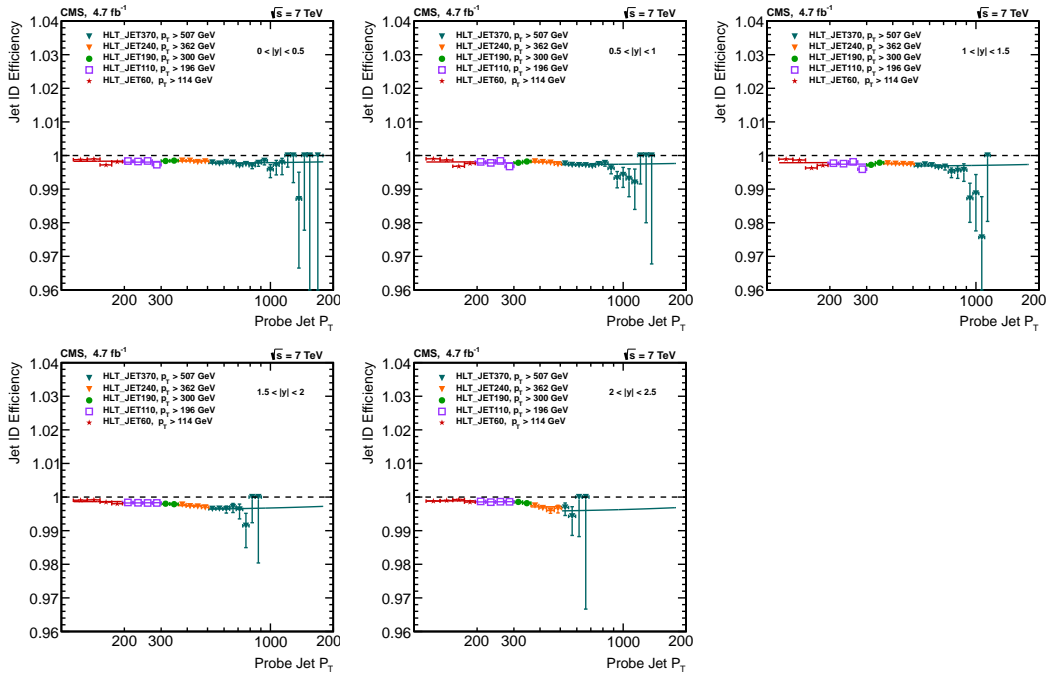


Figure 5.28: The distribution of the jet ID efficiency versus probe jet p_T in five rapidity regions. Each color represents different trigger range with different p_T threshold.

5.3.2 Normalized Rate

The luminosity effect of events that are recorded by the CMS detector is taken into account for the inclusive jet cross section calculations. As we discussed in the previous section, the CMS detector records events with certain luminosity value for the corresponding trigger. Also, every trigger has a “prescale”, P , factor to correct the rates that are accepted by L1 trigger. For the inclusive jet cross section measurements, the prescaled jets coming from five jet triggers are used. The following equations describe the relationships between cross section and luminosity.

$$\sigma = \frac{N_{\text{jet}}}{\int dt L} = \frac{N_{\text{jet}}}{L^{\text{int}}}, \quad \text{if } P = 1. \quad (5.2)$$

$$\sigma = \frac{N_{\text{jet}} \times P}{L^{\text{int}}}, \quad \text{if } P \neq 1. \quad (5.3)$$

$$\sigma = \frac{N_{\text{jet}}}{L_{\text{eff}}}, \quad \text{if } L_{\text{eff}} = \frac{L^{\text{int}}}{P} \quad (5.4)$$

where L^{int} is the integrated luminosity, which is integral of the total luminosity delivered by LHC over time and, L_{eff} is the effective luminosity, which is effective integrated luminosity corrected with prescale factor in the defined trigger menu for every trigger. In this analysis the effective luminosity is calculated by LumiCalc2 calculator as a well known off-line luminosity calculator in the CMS detector and it is used to correct total luminosity by eliminating P factor for each trigger.

The stability of inclusive jet cross section measurements are checked by plotting total normalized rates for each trigger above the turn on in five rapidity. The normalized rate plots are shown in Figs. 5.29-5.33. The distributions are obtained by using the number of jets calculated for each run which is normalized with the corresponding luminosity. The normalized event rate definition is given as:

$$\text{rate (HLT, run)} = \frac{N_{\text{jet}} (\text{HLT, } p_T > \text{Trigger Thresholds})}{L_{\text{eff}} (\text{HLT, run})} \quad (5.5)$$

where L_{eff} is given as:

$$L_{\text{eff}}(\text{HLT}, \text{run}) = \frac{L_{\text{eff}}(\text{run})}{P(\text{HLT}, \text{run})} \quad (5.6)$$

$L_{\text{eff}}(\text{run})$ is the total integrated luminosity as a function of run and $P(\text{HLT}, \text{run})$ is the prescale factor which corresponds to each run for each trigger ($L1_{\text{prescale}} * \text{HLT}_{\text{prescale}}$).

Figs. 5.29-5.33 show the normalized rate distribution for each jet trigger region in five rapidity region. It can be seen from the figures that the rates are stable within a few percent.

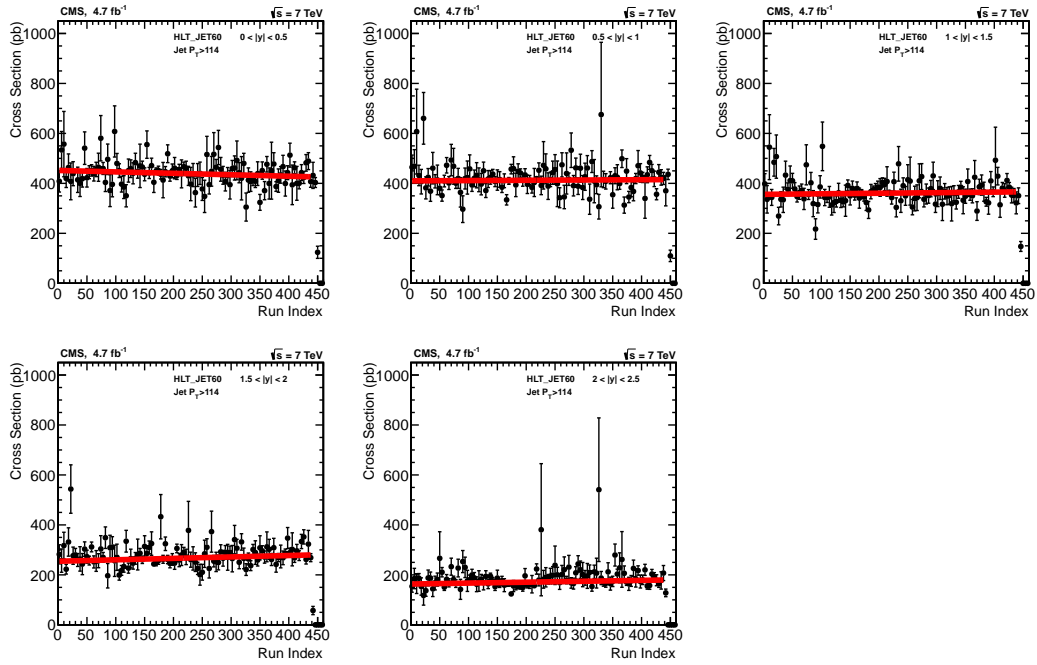


Figure 5.29: The normalized rate distribution of JetHLT60 trigger jet p_T for five rapidity regions.

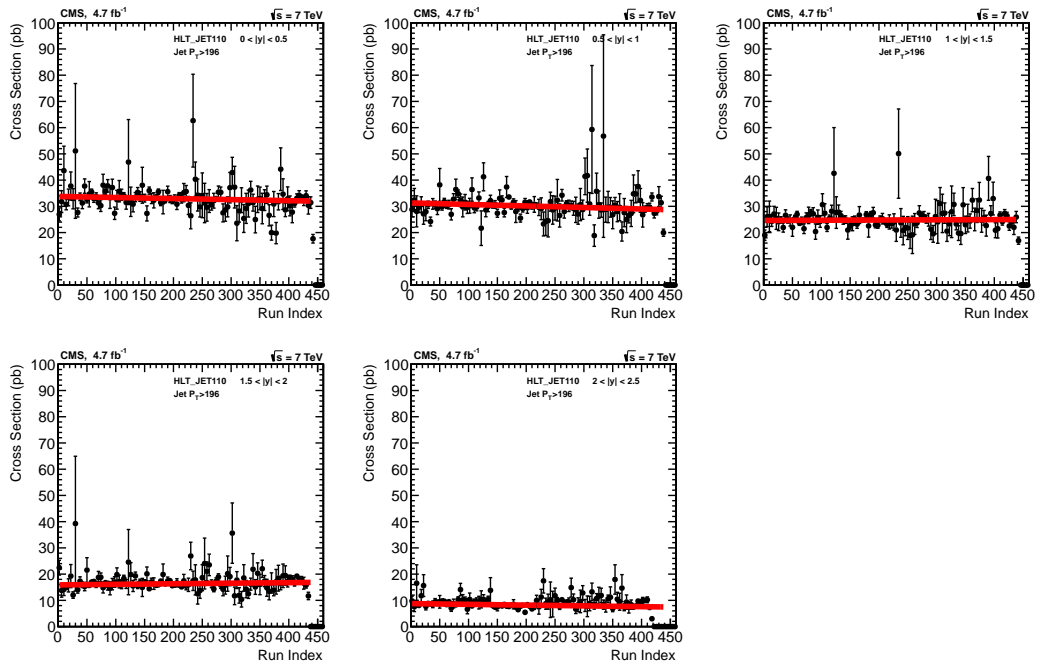


Figure 5.30: The normalized rate distribution of JetHLT110 trigger jet p_T for five rapidity regions.

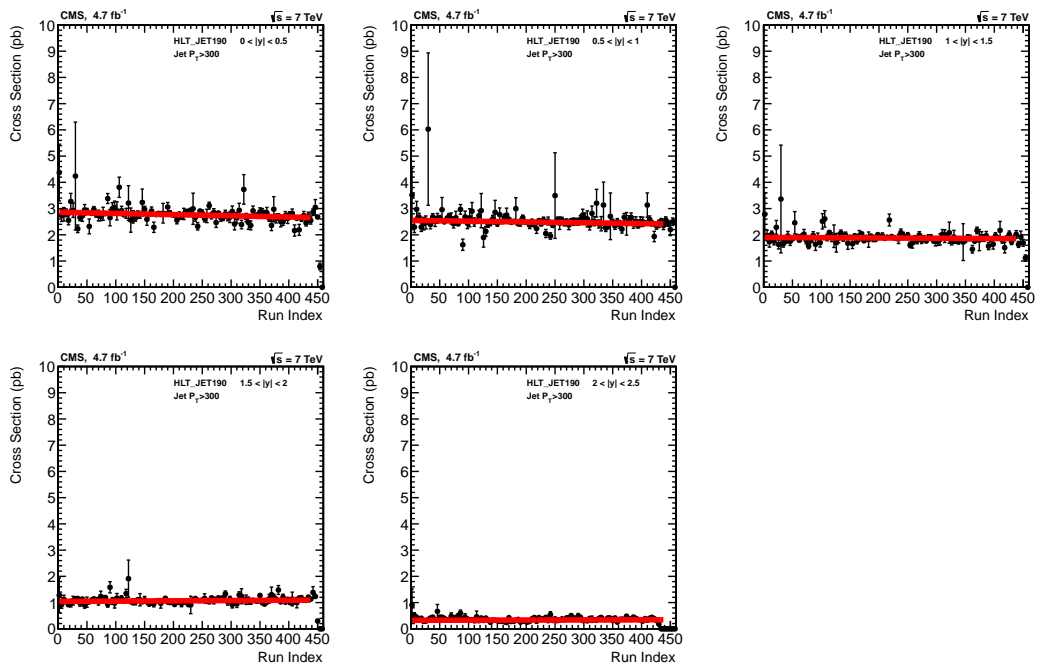


Figure 5.31: The normalized rate distribution of JetHLT190 trigger jet p_T for five rapidity regions.

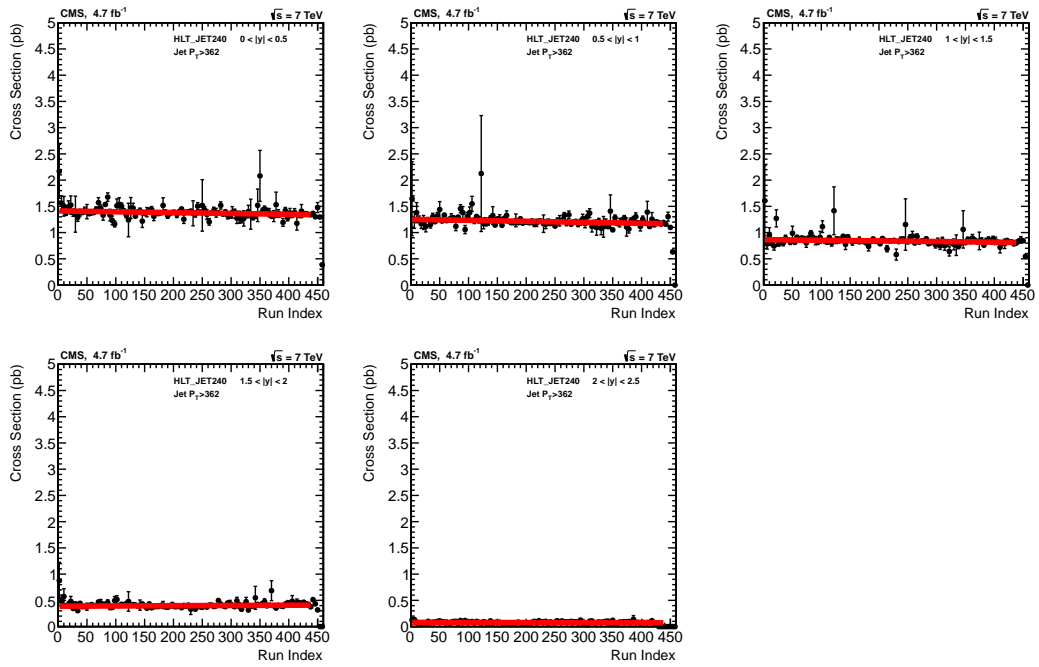


Figure 5.32: The normalized rate distribution of JetHLT240 trigger jet p_T for five rapidity regions.

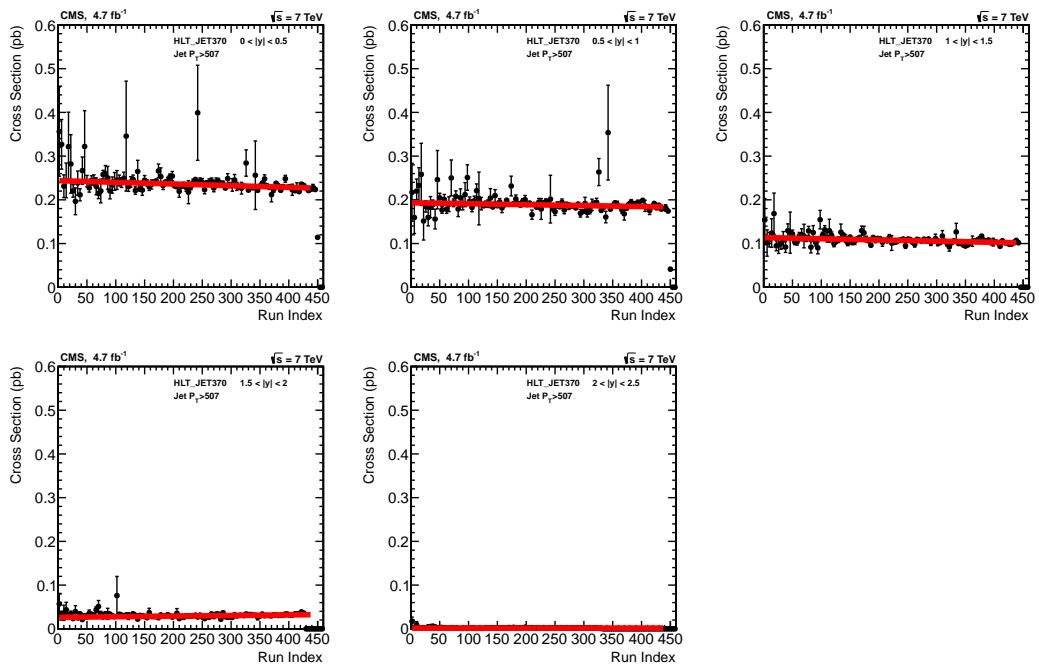


Figure 5.33: The normalized rate distribution of JetHLT370 trigger jet p_T for five rapidity regions.

5.4 Cross Section Normalization by Luminosity

After the cleaning cuts, the inclusive jet p_T reconstruction is achieved by combining the jet p_T spectra coming from individual trigger paths in five rapidity bins. Figure 5.34 shows inclusive jet p_T yields in different rapidity bins and each color represents a specific trigger paths[46].

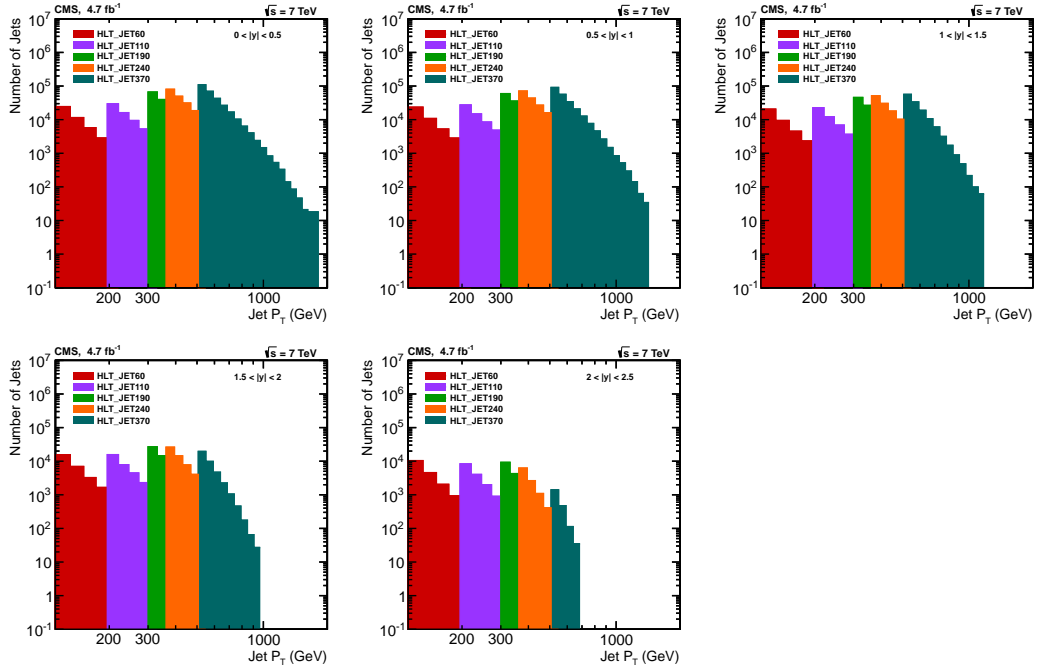


Figure 5.34: The distribution of the jet p_T yields vs number of events for five rapidity regions. Each color represents different trigger range with different p_T threshold.

In order to calculate inclusive jet p_T cross section measurements, the measured yields are transformed into double-differential cross section as:

$$\frac{\sigma^2}{dp_T d|y|} = \frac{1}{\epsilon \cdot \mathcal{L}_{eff}} \frac{N_{jets}}{\Delta p_T \Delta |y|}, \quad (5.7)$$

where N_{jets} is the number of jets in the bin, \mathcal{L}_{eff} is the integrated luminosity of the data samples from events which are recorded by the CMS detector during the 2011 and ϵ is the product of the trigger and event selection efficiencies (both of them are greater than 99%), Δp_T and $\Delta |y|$ are the transverse momentum and rapidity bin

widths, respectively[47]. Fig. 5.35 shows reconstructed spectrum for inclusive jet p_T cross section measurements for each rapidity bin and five different trigger paths. Each different color corresponds to different trigger paths and each mark represents five rapidity[46].

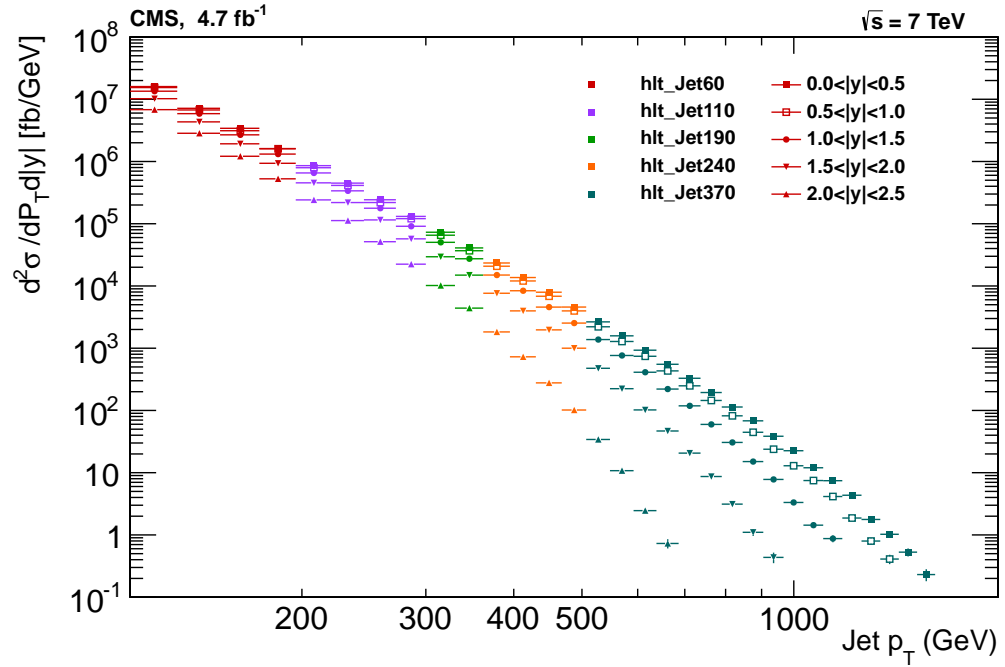


Figure 5.35: The spectrum construction from individual trigger paths for inclusive jet p_T spectrum in five rapidity regions[46].

5.5 Cross Section Unfolding

The measured distribution of observables collected by ideal detector has some distortions because of the limited resolution, response and performance of the detector. The procedure where the distortions are corrected in the measured distributions is called “unfolding”. The unfolding procedure removes the detector effects and reconstructs the measured distributions to get true distribution. Thus, the unfolded data are independent of detector affects, and compare measured spectrum with the theory and other experimental results.

In general, the measured values are different than the true values due to the limited detector resolution. Each observed event has two quantities, one is “measured” and the other is “true” value. Let’s suppose that T_j is the number of true values in the j bins and, M_i is the number of measured values in the i bins which correspond to true j bins. And also, assume that number of events in the j bin is equal to number of events in the i bin. Thus, expected number of events measured in the i bins are equal to sum of the convolution of true events and response matrix element:

$$v_i = \sum_{j=1}^M R_{ij} \mu_j, \quad (5.8)$$

where μ_j is expected number of the true events at the j bins and R_{ij} is response matrix element and gives fraction of given true values in the j bins that end up measured in the i bins. In the meantime, response matrix element R_{ij} gives the probability of finding the observed value in the i bin that corresponds to the true value in the j bin[56].

$$R_{ij} = P(\text{the observed value in the } i \text{ bin} \mid \text{the true value in the } j \text{ bin}).$$

First the true distribution is folded by using response function then this true value is used to unfold the measured distribution.

The “Response Matrix” for the unfolding method can be calculated by using various calculators. In this thesis, the response matrix is calculated by RooUnfold

package[57]. The RooUnfold package provides a framework to compare different unfolding methods such as Iterative Bayes, Singular Value Decomposition (SVD), TUnfold and bin-by-bin correction factors, etc. This package calculates covariance matrix and multidimensional unfolding with the common tools and also it has interfaces for matrix inversion references. On the other hand, the package uses existing ROOT classes. Response matrix can be calculated by using existing histograms or matrices, which are located under the library of this package.

In order to get response matrix element in this analysis, the following approximation in equation has to be made:

$$p_T^{\text{Reco}} \approx \text{Gaus} \left(p_T^{\text{Gen}}, \sigma \left(p_T^{\text{Gen}} \right) \right). \quad (5.9)$$

This approximation is a Gaussian distribution with a mean value of the p_T^{Gen} and sigma of the resolution as a function p_T^{Gen} . p_T^{Gen} represents generated inclusive jet p_T distribution of the true values and p_T^{Reco} represents reconstructed inclusive jet p_T distribution coming from true values but it has some detector effects due to the limited resolution.

The response matrix requires variables of the true and measured sets. In general, the true values are obtained from MC simulations, which contain physical processes and detector information. However, MC simulations do not have a perfect calibration since our understanding of detector is not perfect. And also MC simulations do not take into account by default uncertainties in the response matrix due to finite statistic. When a gaussian distribution with p_T^{Gen} and p_T^{Reco} components is considered, the peak value or mean value of this gaussian is never at the real value due to miscalibration of MC simulation. In other words the response $\left(\frac{p_T^{\text{Reco}}}{p_T^{\text{Gen}}} \right)$ of the jet p_T is not equal to 1. This effect causes inaccurate response matrix calculation. For this reason, the response matrix is calculated by using the so called ‘‘ToyMC’’ for this analysis. The ToyMC means super fast simulation. It has some advantages over the other MC simulations. Basically it does not take into account detector imperfections. And also it is easy to generate as many events as possible thereby increasing the statistics..

The basic principles of ToyMC as follows: First the true values are randomly generated and an uniform jet p_T^{Gen} distribution is obtained. Then, a random reconstructed inclusive jet p_T is obtained by smearing the uniform p_T^{Gen} distribution. For example, let's assume that p_T^{Gen} with 90 GeV is randomly generated with ToyMC, when this p_T^{Gen} with 90 GeV hits the detector, p_T^{Reco} is measured as 89 GeV because of the detector effects. The energy differences between p_T^{Gen} and p_T^{Reco} comes from the resolution of detector. In order to obtain the spectrum, the ToyMC can be run billions of time getting randomly generated jet p_T and corresponding reconstructed jet p_T . There is an important point to emphasize in here; measured inclusive jet p_T spectrum is decreasing spectrum while the generated spectrum which is obtained with ToyMC is flat. In order to get decreasing spectrum from flat generated events, the generated jet p_T has to be weighted while it is generated by ToyMC. Here, the meaning of the "weight" is the probability of p_T^{Gen} occurrence in the measured jet p_T spectrum. This is a "smearing effect".

In this thesis, in order to obtain generated inclusive jet p_T spectrum with ToyMC, The NLO NNPDF[40] set is used to get continues function by fitting the function given below:

$$f(x) = NX^{-\alpha} (1 - X)^{\beta} \quad (5.10)$$

$$X = \frac{2p_T}{\sqrt{s}} \cosh(y_{\min}), \quad (5.11)$$

where X varies with $\cosh(y_{\min})$ parameter and has different values for each rapidity bins. For every pseudorapidity value, inclusive p_T^{Gen} flat distribution is obtained by using the fitted function values. Uniform generated distribution has to be larger then the expected unfolding spectrum. In other words, the uniform generated spectrum has to be beyond the limit. Then generated uniform inclusive jet p_T distribution is weighted to get decreasing spectrum by using resolution parameters. The resolution parameters that are used in this analysis are official JETMET[58] parameters which are calculated from response distribution for each rapidity bins. After this stage,

reconstructed inclusive jet p_T distribution is obtained from smeared generated inclusive jet p_T distribution to understand resolution effect of detector on the measured distribution. The number of reconstructed inclusive jet p_T events has to be equal to the number of generated events. And reconstructed jet p_T numbers correspond to mean value and sigma of the Gaussian distribution on the generated inclusive jet p_T as noted above in the approximation. These generated and reconstructed inclusive jet p_T distribution are used to calculate response matrix with the RooUnfoldPackage. Figure 5.36 shows response matrix which is calculated by Bayesian unfolding method of the D'Agostini implemented RooUnfoldPackage. And also response matrices must be square and orthogonal.

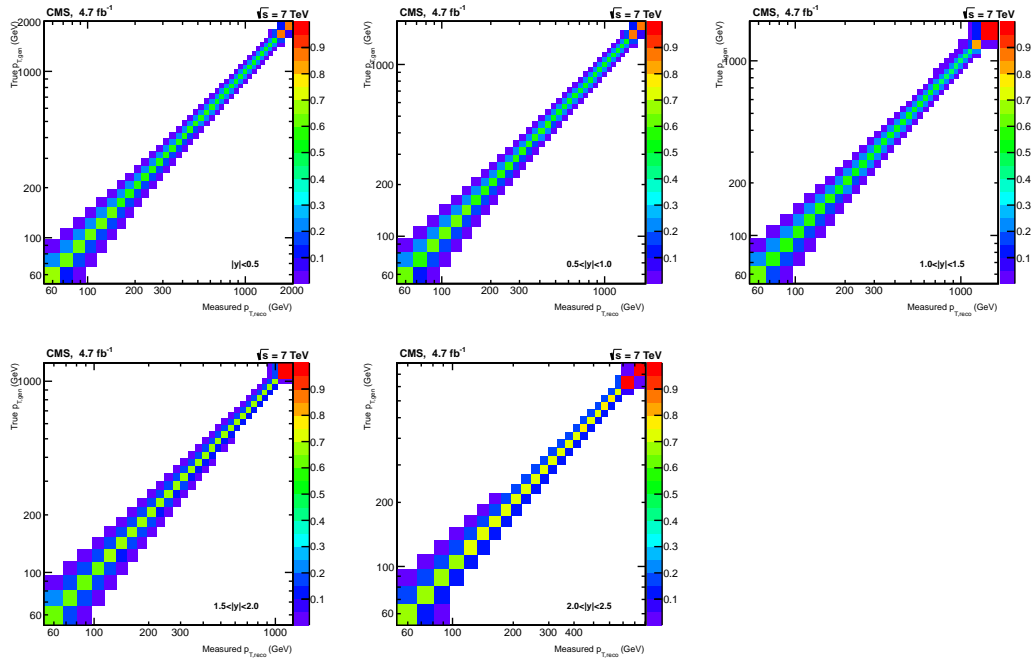


Figure 5.36: The Bayes's response matrices for inclusive jet p_T in five rapidity region.

There are three different unfolding methods considered for the analysis but only the best matching one is used for the final calculations. One of them is the bin-by-bin unfolding correction factor, which is used for the problems with one variable. This method considers taking a ratio for the number of reconstructed variable events at certain bin to number of true variable events in the same bin by using MC simulations. Then this ratio is used to calculate the number of true events coming from the number of observed events in this bin. On the other hand, this method does not take

into account bin event migration, which passes through from one bin to other bin. To solve this problem, the matrix is calculated to correlate number of generated events at a bin with number of observed events at the other bin. The calculated matrix is inverted and applied to the measured distribution. This method does not work in huge statistical fluctuations due to negative matrix elements which come from big value of the denominator[59]. This is undesirable for the experimental results. Bin-by-bin unfolding method does not give good results for multidimensional problems. RooUnfoldPackage defines RooUnfoldBinByBin algorithm also known as “unregularized algorithm” for bin-by-bin unfolding method to calculate correction factor, but this is not recommended by RooUnfoldPackage because of the large bin-by-bin correlations and huge statistical fluctuations [57].

The other unfolding correction method is Singular Value Decomposition (SVD). RooUnfoldPackage provides RooUnfoldSVD algorithm included by Tackman into ROOT by using Hocker and Kartvelishvili’s unfolding method for TSVDUnfold classes.

The Bayes’s unfolding theorem defined by G.D. Agostini is used for this analysis. The calculated unfolding results with the Bayes’s method on data samples are compared with the theory in this thesis. The Bayes’s theorem has some advantage when it is compared with other unfolding methods. It is based on strong theoretical background, and applied to multidimensional problems easily. It can also take into account of smearing events and migration events from true to observed values, and also provides matrix correlations of the results. Bayes’s theorem handles several independent states ($C_i, i = 1, 2, 3, \dots, n_C$) with E effect. Let’s assume that $P(C_i)$ represents initial probability of the states and $P(E|C_i)$ represents the dependent probability of the i th state which produces E effect. Bayes’s formula can be written as:

$$P(C_i|E) = \frac{P(E|C_i) P(C_i)}{\sum_{l=1}^{n_C} P(E|C_l) P(C_l)} \quad (5.12)$$

The Bayes’s formula shows that the probability of the i th state proportional to the initial probability of the state times the probability of the state with E effect produced. It seems that $P(C_i|E)$ depends on the initial probability of the state. If an event with

E effect is observed, the expected number of events appointed to each state can be expressed as:

$$\hat{n}(C_i) = n(E) \cdot P(C_i|E) \quad (5.13)$$

As a result of the measurement, for each given C_i states, there are E_j ($j = 1, 2, \dots, n_E$) effects with different probabilities. If the Bayes's formula is rewritten for each effect:

$$P(C_i|E_j) = \frac{P(E_j|C_i) P(C_i)}{\sum_{i=1}^{n_c} P(E_j|C_i) P(C_i)} \quad (5.14)$$

where, $P(C_i|E_j)$ is called as a “smearing matrix”, even if it is defined as a cell to cell migration. Briefly Bayes's unfolding method can be applied in the following steps. First step is to select expected initial number of events from initial distribution probability $P(C_i)$. The $P(C_i)$ has to be a uniform distribution. Second step is to calculate final expected number of events, $\hat{n}(C)$ and final probability of the states, $\hat{P}(C)$. The third step is to compare χ^2 between initial expected number of events and final expected number of events. And the last one is to replace $P(C_i)$ with $\hat{P}(C)$ and $n_0(C)$ with $\hat{n}(C)$, and to recalculate the probabilities of the states until χ^2 gets small enough. If χ^2 has a small enough value it stops the iteration, if not it recalculates the second step.

RooUnfoldPackage provides RooUnfoldBayes algorithm defined by D'Agostini. RooUnfoldBayes initially takes into account training truth instead of flat distribution as described in the D'Agostini method. The optimum values are obtained after about four iterations for RooUnfoldPackage in general. Basically for this analysis, four iterations are used to calculate unfolding parameters with Bayes's method by using RooUnfoldBayes algorithm.

For a sanity check, Bayes's, bin-by-bin and SVD unfolding methods are compared with the forward smearing process, which is a smeared function calculated by effective

σ resolution parameters due to detector effects into the true values coming from fitted NNPDF PDF sets. Figure 5.37 and 5.38 show comparison of the different unfolding method measurements and ratio of the correction factor to forward smearing calculated by using RooUnfoldPackage in five rapidity regions, respectively. It seems that each unfolding method is comparable with the forward smearing.

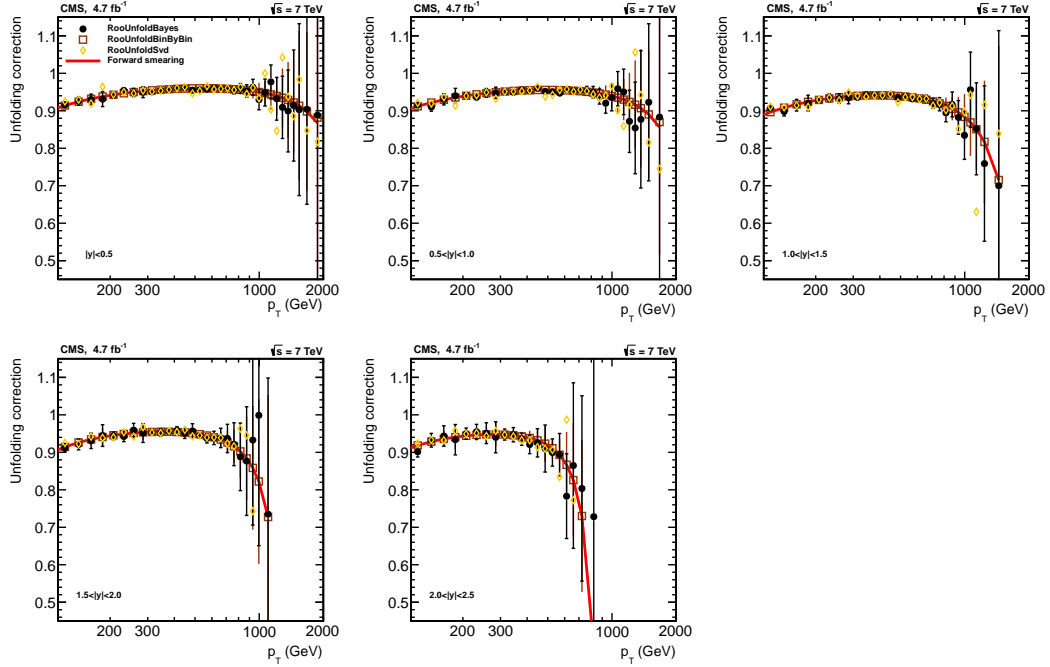


Figure 5.37: Different unfolding measurements calculated by using RooUnfoldPackage in five rapidity regions.

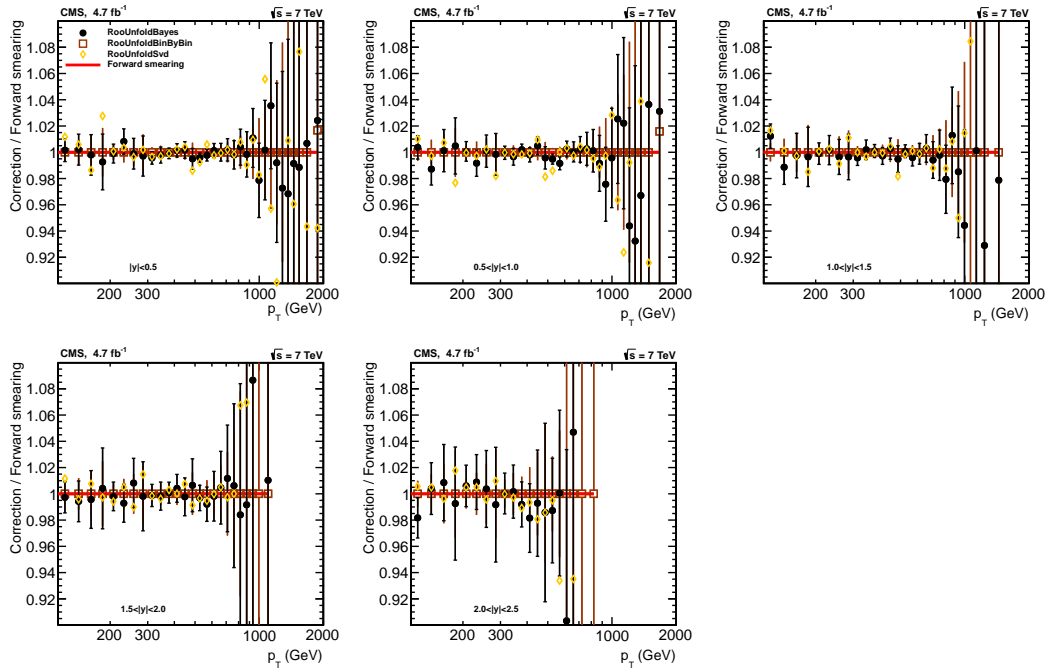


Figure 5.38: The ratio of the unfolding measurements to forward smearing in five rapidity regions.

5.6 Systematic Uncertainties

The systematic uncertainties on the inclusive jet p_T measurements consist of the uncertainty in JES, luminosity and jet p_T resolution. Those uncertainty sources are dominant on the measured inclusive jet p_T . Other uncertainty sources like jet angular resolution is negligible. The individual uncertainty sources will be discussed in the sections below.

5.6.1 Jet Energy Scale Uncertainty

The dominant uncertainty source for the inclusive jet p_T measurements is the JES. In this analysis, the individual JES uncertainty sources are collected under four main category defined by the CMS detector; pile-up effect, relative uncertainty dependent on η , absolute uncertainty dependent on p_T and differences in the quark and gluon originated jets. However, for inclusive jet p_T measurements in this thesis η and p_T dependent JES uncertainty sources are taken into account. In the inclusive jet p_T spectrum, small uncertainty values of the p_T scale transform to big uncertainty values for a given value of the p_T , because the inclusive jet p_T spectrum has a sharp decreasing spectrum.

p_T and η dependent uncertainties coming from JES on measured inclusive jet p_T are estimated by shifting upper and lower end of p_T for 16 individual JES sources which contribute to the total uncertainty. Each uncorrelated JES uncertainty source demonstrate 1σ variation from given systematic effect for each point at the (p_T, η) coordinates. Positive and negative variation on JES sources is processed separately as:

$$p_T^{\pm} = p_T \cdot (1 \pm \sigma) \text{ and } p_T^{\mp} = p_T \cdot (1 - \sigma), \quad (5.15)$$

where, p_T^{\pm} represents up and down variation of the inclusive p_T jet spectrum respectively and σ expresses variation on JES sources. Figure 5.39 displays η and p_T

dependent JES uncertainty effect on inclusive jet p_T measurements. This uncertainty has been estimated to be 2% - 2.5% [60] and translates 10% to 30% uncertainty on cross section.

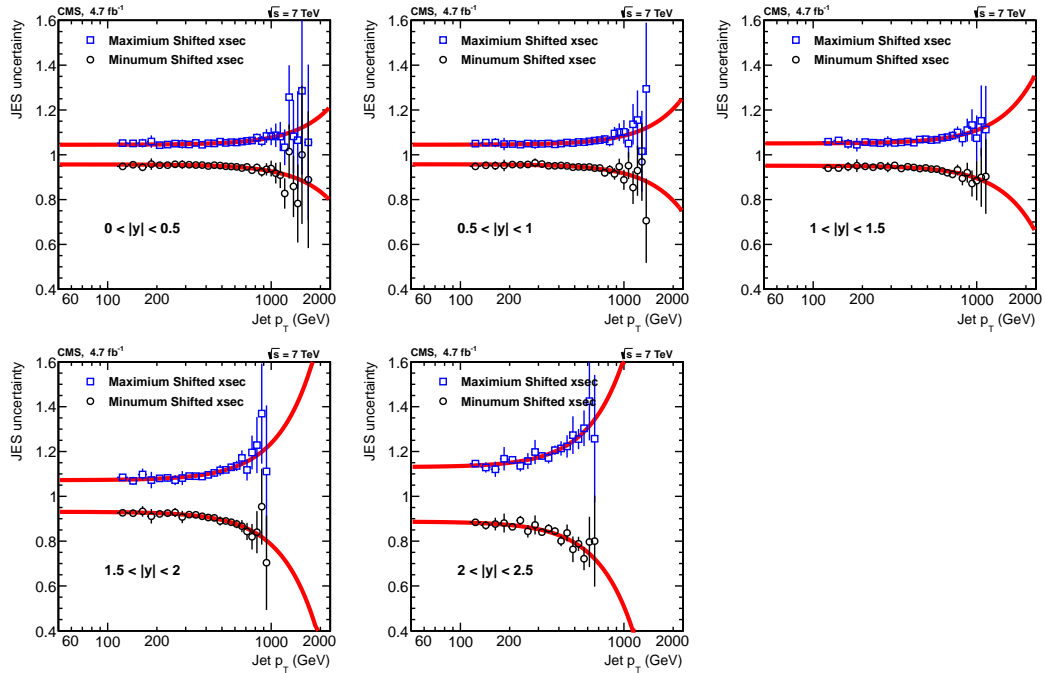


Figure 5.39: The JES uncertainties on inclusive jet p_T measurement in five rapidity regions.

5.6.2 Unfolding Uncertainty

The unfolding uncertainty correction is associated with jet p_T resolution in the simulation and sharp slope of the inclusive jet p_T spectrum. In order to calculate effect of the jet energy resolution parameters[55] on unfolding uncertainty, jet p_T resolution inputs are varied by $\pm 10\%$ while inclusive jet p_T spectrum stays constant. As seen Fig. 5.40, the middle line is the nominal value of the spectrum and the other up and down lines are the maximum and minimum values of the JER variation, respectively. On the other hand, unfolding correction on inclusive jet p_T spectrum changes between 5% and 10%. Figure 5.41 shows the max. and min. variation for the 5 η region. The uncertainty coming from the slope of the inclusive jet p_T spectrum adds 5% on unfolding uncertainties.

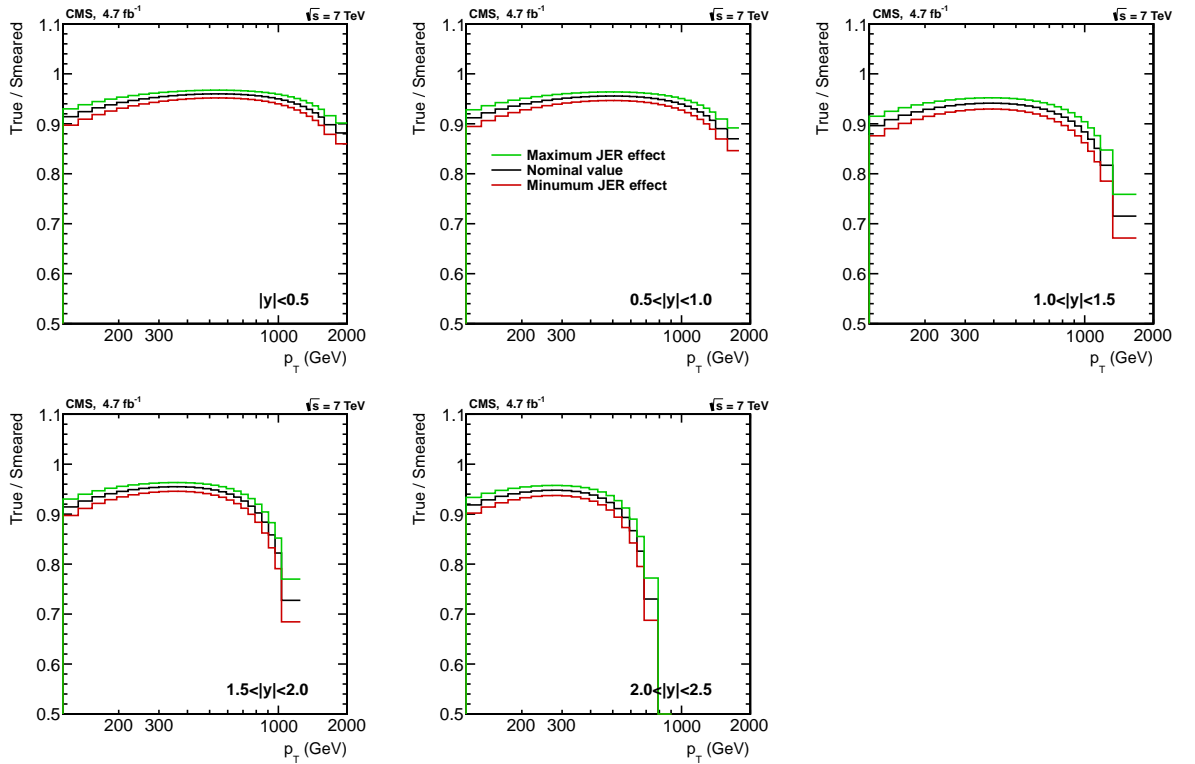


Figure 5.40: Unfolding uncertainty effect on jet p_T resolution.

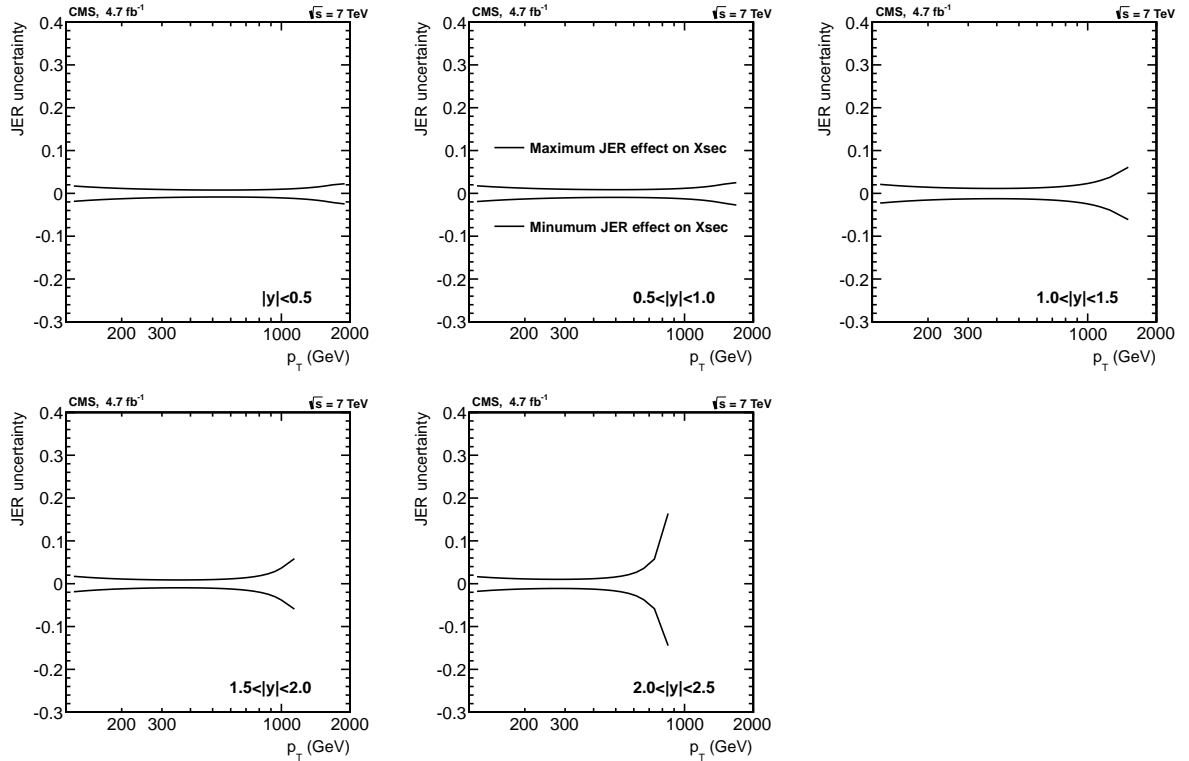


Figure 5.41: Unfolding uncertainty effect on the inclusive jet p_T spectrum.

5.6.3 Luminosity Uncertainty

The uncertainty of luminosity on the cross section normalization is 2.2% [61] that is correlated directly for all jet p_T bins.

5.6.4 Other Uncertainties

The contribution of the other experimental uncertainty sources on the inclusive jet p_T measurement are the trigger, jet identification inefficiency, time dependency of the jet p_T resolution and the trigger prescale factor that are estimated to be much smaller than 1%. This is assigned for each uncorrelated jet p_T bins.

5.6.5 Experimental Uncertainty Correlations

Figure 5.42 shows an illustration of all systematic uncertainties effect on inclusive jet p_T cross section measurements in five rapidity regions. As seen in Fig. 5.42, JES uncertainty that is shown with blue dash line is the dominant source of systematic uncertainties. It comes from p_T and η dependent jet energy calibration and is estimated as 2-2.5%. Another important uncertainty source is the unfolding uncertainty with colored green. The unfolding uncertainty comes from jet energy resolution and is 10% for unfolding measurement. Thus it introduces variations between 5% and 10% on inclusive jet cross section measurements. The luminosity uncertainty source with red dash line has a 2.2% effect on inclusive jet cross section measurements. Other trigger and jet identification uncertainties contribute less than 1% on cross section measurement. The total experimental uncertainty affect on cross section measurement is around 5% at low p_T up to $|\eta|=1.5$. On the other hand, total uncertainty increases to 10% and 30% in high η bins.

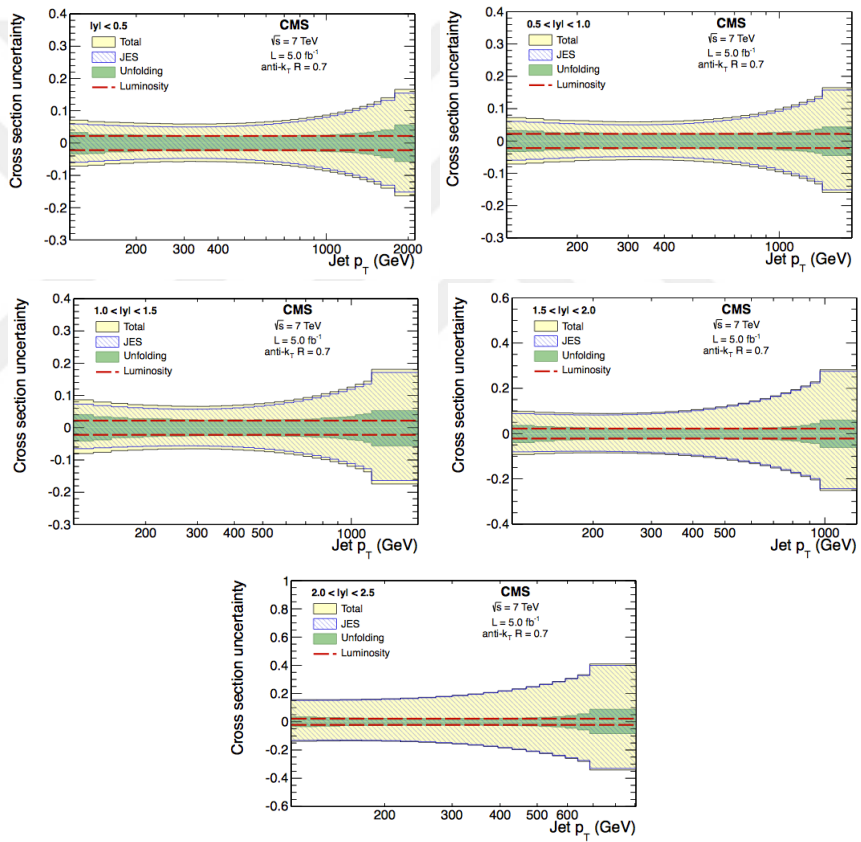


Figure 5.42: The Experimental uncertainties on inclusive jet p_T measurements in five rapidity regions.

6. RESULTS AND CONCLUSIONS

Double-differential inclusive jet cross section was measured as a function of jet p_T by the CMS experiment during 2011. The data with $\approx 5.0 \text{ fb}^{-1}$ comes from proton-proton collisions at $\sqrt{s} = 7 \text{ TeV}$. The jet p_T range from 114 GeV to 2000 GeV, in five rapidity bins of equal width up to $|\eta| = 2.5$, was used for the measurement. Experimental cross sections are compared with the pQCD predictions for five PDF sets as described before. The experimental uncertainties are comparable to PDF uncertainties in NNPDF2.1.

Figure 6.1 shows double differential inclusive jet cross section measurement as a function of jet p_T compared with theory predictions in five rapidity bins. The NNPDF set is corrected for NP correction factors and the experimental and theoretical data are in agreement. Cross section measurement conducted in 2011 with anti- $k_T = 0.7$ cone size on the left side is compared with 2010 cross section measurements[2] with anti- $k_T = 0.5$ cone size on the right side in Fig. 6.1. In general the spectra are in good agreement, when taking into account the jet energy scale uncertainties and different jet radius. The observed differences are fully compatible with the 2010 JEC uncertainty, which reached up to 4-5% at high p_T , corresponding to a cross section uncertainty of about about 30 % at high p_T (and up to 60 % at high rapidities).

In order to compare the measured data in the CMS detector and theoretical predictions, the ratio of them is calculated. Figure 6.2 shows the ratio of the measured data and theoretical predictions for all the different PDF sets, by using the central value of the NNPDF 2.1. All pQCD at NLO measurements are compatible with the experimental data within the theoretical and experimental uncertainties. Among the

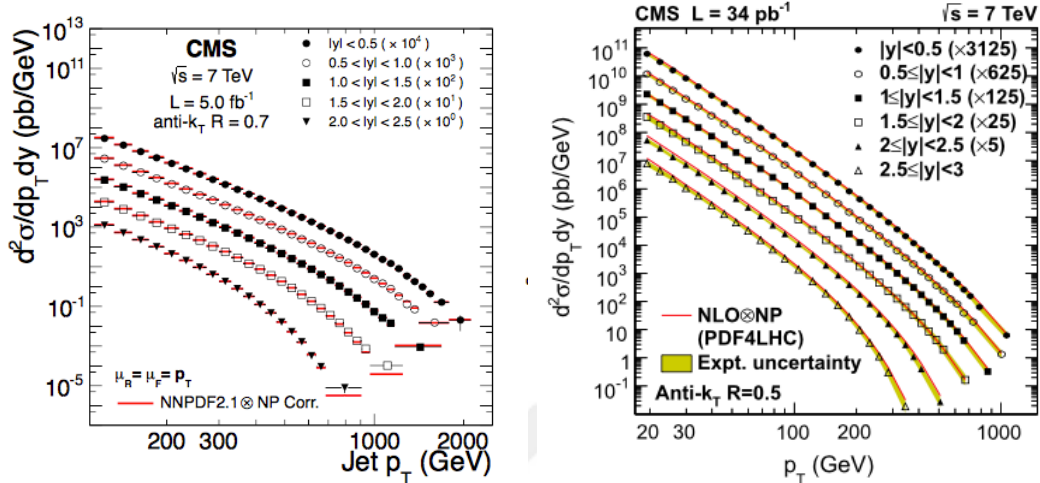


Figure 6.1: The comparison of the double differential inclusive jet p_T cross section measurements with theoretical prediction in five rapidity regions at 7 TeV. The left side represents inclusive jet cross section with anti- $k_T = 0.7$ cone size for approximately 5 fb^{-1} luminosity while the right side represents inclusive jet cross section with anti- $k_T = 0.5$ cone size for 34 pb^{-1} luminosity from previous results.

all PDFs, CT10, HERA1.5, and NNPDF2.1 has better agreement with the data, on the other hand ABKM09 has the largest discrepancy and MSTW2008 cross section predictions are too high in all $|y|$ bins at low momenta in all rapidity bins.

Results of this analysis are used in Ref.[62] to extract α_s and PDF constraints that are fundamental parameter of QCD. Using inclusive jet data also allowed to reduced the uncertainty in the gluon distribution for fractional parton momenta $x \geq 0.01$.

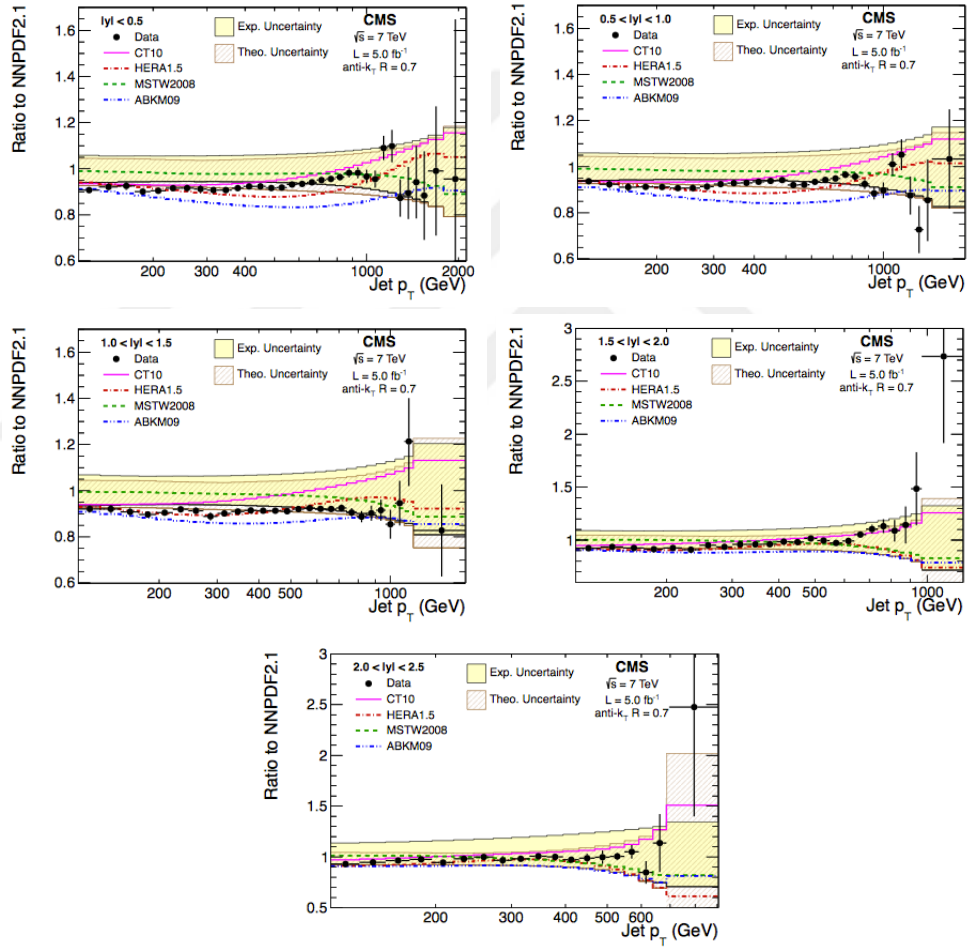


Figure 6.2: Comparison of inclusive jet p_T cross section measurements to theory for different PDF sets in five rapidity region.

Bibliography

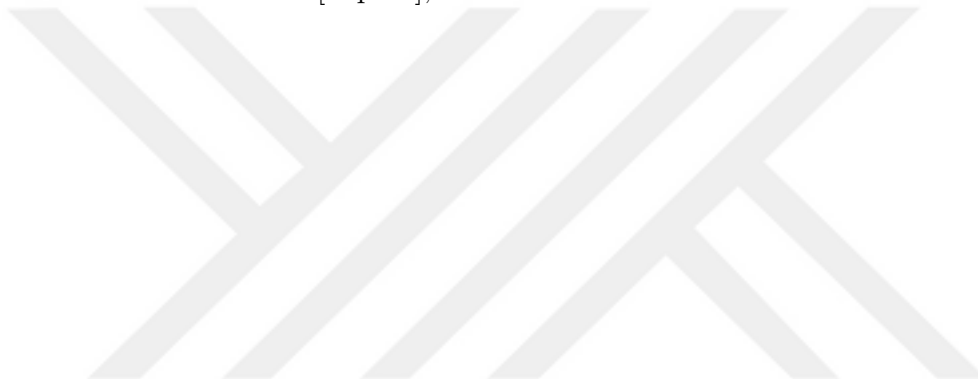
- [1] CMS Collaboration, “Measurement of the differential dijet production cross section in proton proton collisions at $\sqrt{s}=7$ TeV”, Phys. Lett. B 700 187, 2011.
- [2] CMS Collaboration, “Measurement of the Inclusive Jet Cross Section in pp Collisions at $\sqrt{s}=7$ TeV”, Phys. Rev. Lett. 107, 132001, 2011.
- [3] ATLAS Collaboration, “Measurement of inclusive jet and dijet production in pp collisions at $\sqrt{s}=7$ TeV using the ATLAS detector” Phys. Rev. D 86, 014022, 2012.
- [4] Lyndon Evans and Philip Bryant (editors), “The Cern Large Hadron Collider: Accelerator and Experiments” JINST 3 S08001, 2008.
- [5] CMS Collaboration, “The CMS experiment at the CERN LHC”, JINST 3 S08004, 2008.
- [6] The ATLAS Collaboration et al., “The ATLAS Experiment at the CERN Large Hadron Collider”, JINST 3 S08003, 2008.
- [7] LHCb Collaboration et al., “The LHCb Detector at the LHC” JINST 3 S08005, 2008.
- [8] The TOTEM Collaboration et al., “The TOTEM Experiment at the CERN Large Hadron Collider”, JINST 3 S08007, 2008.
- [9] Amos Breskin and Rudiger Voss The ALICE Collaboration et al. “The ALICE experiment at the CERN LHC”, JINST 3 S08002, 2008.
- [10] Breskin, Amos (ed.) ; Voss, Rdiger (ed.) (CERN), “The CERN Large Hadron Collider: Accelerator and Experiments”, Volume 1, 2009.
- [11] “CMS Detector Design”, url: <http://cms.web.cern.ch/news/cms-detector-design>, last visited September, 2015.

- [12] CMS Collaboration, “Detector Performance and Software”, CMS Physics Technical Design Report, Volume I(CMS TDR 8.1) 2, 2006.
- [13] Kiriakos Hilbert, “CMS Pixel Detector Noise Calibrations” Northside College Prep Quarknet Mentored by Dr. Marco Verzocchi, 2013.
- [14] CMS Collaboration, “The CMS experiment at the CERN LHC”, JINST 3 S08004, 2008.
- [15] Renker D., “Properties of avalanche photodiodes for applications in high energy physics, astrophysics and medical imaging”, Nucl. Instrum. Meth. A486 164169, 2002.
- [16] K. W. Bell et al., “Vacuum phototriodes for the CMS electromagnetic calorimeter endcap”, IEEE Trans. Nucl. Sci. 51 2284, 2004.
- [17] CMS Collaboration, “The TriDAS Project, Technical Design Report, Volume 1: The Trigger Systems”, CERN/LHCC 2000-38, CMS TDR 6.1, 2000.
- [18] CMS Collaboration, “The TriDAS Project, Technical Design Report, Volume 2: Data Acquisition and High-Level Trigger”, CERN/LHCC, CMS TDR 6.2, 2002.
- [19] CMS HCAL Collaboration (Abdullin, S. et al.), “Design, performance, and calibration of CMS hadron-barrel calorimeter wedges - CMS”, Eur.Phys.J.C55,159-171, 2008.
- [20] CMS Collaboration, “Technical Design Report Volume 1: Detector Performance and Software”, CERN/LHCC 2006-001, 2006.
- [21] P. Cushman, A. Heering and A. Ronzhin, “Custom HPD readout for the CMS HCAL”, Nucl. Instrum. Meth. A 442 289, 2000.
- [22] P. B. Cushman and A. H. Heering, “Problems and solutions in high-rate multichannel hybrid photodiode design: The CMS experience”, IEEE Trans. Nucl. Sci. 49 963, 2002.
- [23] CMS HCAL Collaboration (Baiatian, G. et al.), “Design, performance, and calibration of CMS hadron endcap calorimeters”, CERN-CMS-NOTE-2008-010, 2008.
- [24] CMS HCAL Collaboration, “Design, performance, and calibration of the CMS Hadron-outer calorimeter”, Eur.Phys.J. C57 653663, 2008.
- [25] J. Beringer et al., “2012 Review of Particle Physics - Gauge and Higgs Bosons”, Physical Review D 86: 1, 2012.
- [26] CMS Collaboration, “CMS, the Compact Muon Solenoid. Muon technical design report”, CERN-LHCC-97-32, 1997.

- [27] CMS Collaboration, “Performance of the CMS Cathode Strip Chambers with Cosmic Rays”, JINST 5 T03018, 2010.
- [28] The CMS Collaboration, “Performance Study of the CMS Barrel Resistive Plate Chambers with Cosmic Rays”, arXiv:0911.4045v2, 2010.
- [29] Halzen, Francis; Martin, Alan, “Quarks and Leptons: An Introductory Course in Modern Particle Physics”, John Wiley and Sons. ISBN 0-471-88741-2, 1984.
- [30] A. Pich, “The Standard Model of Electroweak Interactions” arXiv:hep-ph/0502010, 2010.
- [31] K.A. Olive et al., “Review Of Particle Physics”, (Particle Data Group), Chin. Phys. C, 38, 090001, 2014.
- [32] Vernon D. Barger, Roger J. N. Phillips, “Collider Physics”, ISBN-13: 978-0201149456.
- [33] Mikko Voutilainen, “Measurement of the Inclusive Jet Cross Section in p-anti-p Collisions at $\sqrt{s}=1.96$ TeV”, Fermilab, 2008.
- [34] G. Dissertori, G.P. Salam, “Quantum Chromodynamics”, 2009.
- [35] Sourav Sarkar(ed), Helmut Satz(ed), Bikash Sinha(ed), “The Physics of the Quark-Gluon Plasma: Introductory Lectures”, 2010.
- [36] Davison E. Soper, “Basics of QCD Perturbation Theory”, arXiv:hep-ph/9702203, 1997.
- [37] Zhen-Jun Xiao, “NLO contributions in the pQCD approach”, arXiv:0810.2199, 2008.
- [38] Z. Nagy, “Next-to-leading order calculation of three jet observables in hadron-hadron collisions”, Phys. Rev. D 68 094002, 2003.
- [39] T. Kluge, K. Rabbertz, and M. Wobisch, “fastNLO: Fast pQCD calculations for PDF fits”, arXiv:hep-ph/0609285v2, 2006.
- [40] R. D. Ball et al., “A first unbiased global NLO determination of parton distributions and their uncertainties”, Nucl. Phys. B 838 136, 2010.
- [41] H.-L. Lai et al., “New parton distributions for collider physics”, Phys. Rev. D 82 074024, 2010.
- [42] A. D. Martin et al., “Parton distributions for the LHC”, Eur. Phys. J. C 63 189, 2009.
- [43] H1 and Z. Collaborations, “Combined Measurement and QCD Analysis of the Inclusive ep Scattering Cross Sections at HERA”, JHEP 01 109, 2010.

- [44] S. Alekhin, J. Blumlein, and S. Klein, “The 3-, 4-, and 5-flavor NNLO Parton from Deep-Inelastic-Scattering Data and at Hadron Colliders”, *Phys. Rev. D* 81 014032, 2010.
- [45] M. Bahr et al., “Herwig++ Physics and Manual”, *Eur. Phys. J. C* 58 639, 2008.
- [46] CMS Collaboration, “Measurement of The Inclusive Jet Cross Section at $\sqrt{s}=7\text{TeV}$ ”, CMS AN-11-462, 2011.
- [47] S. Chatrchyan et al. (CMS Collaboration), “Measurements of differential jet cross sections in proton-proton collisions at $s = 7\text{ TeV}$ with the CMS detector”, *Phys. Rev. D* 87, 112002, 2013.
- [48] G. P. Salam, and G. Soyez, “A practical Seedless Infrared-Safe Cone jet algorithm”, *JHEP* arXiv:0704.0292, 2007.
- [49] M. Cacciari, G. P. Salam, and G. Soyez, “The anti-kt jet clustering algorithm”, *JHEP* 04 063, 2008.
- [50] M. Cacciari and G. Salam, “Dispelling the N3 myth for the kt jet-finder”, *Phys. Lett. B* 641 57, 2006.
- [51] CMS Collaboration, “Particle-Flow Event Reconstruction in CMS and Performance for Jets, Taus, and E/T”, CMS Physics Analysis Summary CMS-PAS-PFT-09-001, 2009.
- [52] CMS Collaboration, “Plans for Jet Energy Corrections at CMS”, CMS Physics Analysis Summary CMS-PAS-JME-07-002, 2008.
- [53] T. Sjostrand, S. Mrenna, and P. Skands, “PYTHIA 6.4 physics and manual”, *JHEP* 05 026, 2006.
- [54] S. Agostinelli et al., “Geant 4 A Simulation Toolkit”, *Nucl. Inst. Meth. A* 506 250, 2003.
- [55] CMS Collaboration, “Determination of Jet Energy Calibration and Transverse Momentum Resolution in CMS”, *JINST* 6 P11002, 2011.
- [56] Glen Cowan, “Statistical Data Analysis”, CLARENDON PRESS OXFORD, ISBN 0 19 850156 0 (Hbk), ISBN 0 19 850155 2 (Pbk), 1998.
- [57] T. Auye, “Unfolding Algorithms And Tests Using RooUnfold”, arXiv:physics.data-an/1105.1160, 2006.
- [58] CMS Collaboration, “Jet Energy Scale performance in 2011”, CMS Detector Performance Summary CMS DP-2012/006, 2012.
- [59] G. D. Agostini, “A multidimensional unfolding method based on Baye’s theorem”, *Nuclear Instruments Methods in Physics research* A362, 487-498, 1995.

- [60] CMS Collaboration, “Jet Energy Scale performance in 2011”, CMS Detector Performance Summary CMS DP-2012/006, 2012.
- [61] CMS Collaboration, “Absolute Calibration of the Luminosity Measurement at CMS:Winter 2012 Update”, CMS Physics Analysis Summary CMS-PAS-SMP-12-008, 2012.
- [62] CMS Collaborations, “Constraints on parton distribution functions and extraction of the strong coupling constant from the inclusive jet cross section in pp collisions at $\sqrt{s}=7\text{TeV}$ ”, CMS-SMP-12-028 ; CERN-PH-EP-2014-238, arXiv:1410.6765 [hep-ex], 2014.



Curriculum Vitae

Contact Details

Kafkas University, Faculty of Science and Letters, Physics Dpt.
36100 Kars, the Turkey
okaya@cern.ch



EDUCATIONAL BACKGROUND

- 2008 - 2015** PhD in Faculty of Science and Letters, **KAFKAS UNIVERSITY**, Kars, Turkey
PhD Thesis: Measurement of The Differential Inclusive Jet Cross Section at 7 TeV in the CMS Detector.
- 2004 - 2007** MA in Faculty of Science and Letters, **KAFKAS UNIVERSITY**, Kars, Turkey
MA Thesis: Hadronic End-cap Muon Calibration with 2006 Test Beam Data at CMS Experiment.
- 1999 - 2003** BA in Faculty of Science and Letters, **KAFKAS UNIVERSITY**, Turkey
BA Thesis: The Glass and Its Properties.

EXPERIENCE

- 2009 – current** Research Assistant in Physics Department, **KAFKAS UNIVERSITY**, Turkey
- 2005 – 2009** Research Assistant in The Science of Institute, **KAFKAS UNIVERSITY**, Turkey

SELECTED PUBLICATIONS

- CMS Collaboration, Measurements of differential jet cross sections in proton-proton collisions at $\sqrt{s} = 7$ TeV with the CMS detector, Phys. Rev. D 87, 112002, 2013.**
- CMS Collaboration, Measurement of the Inclusive Jet Cross Section in pp Collisions at $\sqrt{s} = 7$ TeV, Phys. Rev. Lett. 107, 132001, 2011.**
- CMS Collaboration, Determination of Jet Energy Calibration and Transverse Momentum Resolution in CMS, published JINST 6 (2011) 11002.**
- CMS HCAL/ECAL Collaborations, The CMS barrel calorimeter response to particle beams from 2 to 350 GeV/c. Eur. Phys. J. C (2009) 60: 359–373**
- CMS HCAL Collaborations, Design, performance, and calibration of the CMS Hadron-outer calorimeter. CERN-CMS-NOTE-2008-020, Jun 2008. 14pp. Eur.Phys.J.C57:653-663,2008.**

OTHER PUBLICATIONS

<https://inspirehep.net/author/profile/O.Kaya.1>

TALKS, LECTURES, TRAINING AND QUALIFICATIONS

13 March 2013 Presenter (Poster): Ozlem KAYA, "Measurement of The Cross Section at CMS"
LHCC Meeting Student Poster Session, Geneva, CERN, Switzerland.

26 March 2012 Presenter: Ozlem KAYA, "Jet Cross Section Measurements with CMS".
XX International Workshop on Deep-Inelastic-Scattering and Related Subjects, Bonn, Germany.

LANGUAGE SKILLS

Turkish Native speaker,
English Fluent.

ANALYSIS EXPERIENCES

2015 Hadronic ttH(bb) analysis, PAG, CMS, CERN.
2014 JetMET HCAL trigger pile-up study, POG, CMS, CERN.
2013 Jet energy resolution with 2012 CMS data under the JEC+JER group, POG, CMS, CERN.
2013 HF upgrade test studies, 2013, CMS detector under the FH upgrade group, DPG, CMS, CERN.
2011-2012 Measurement of the inclusive jet cross section with 2011 CMS data, PAG, CMS, CERN.
2009-2010 The jet matching studying under the JEC group, POG, CMS, CERN.
2007-2008 HCAL calibration study, CMS, CERN.
2006 HCAL upgrade test beam studies, CMS, CERN.
2005 HF PMT and light leak tests, CMS, CERN.

IT SKILLS

ROOT, C++, python, Linux, Windows

REFEREES

Prof. Dr. Erhan Gulmez, Faculty of Science and Letters, **BOGAZICI UNIVERSITY**, Istanbul, Turkey
gulmez@boun.edu.tr

Prof. Dr. Mithat KAYA, Faculty of Science and Letters, **MARMARA UNIVERSITY**, Kars, Turkey
mithat@cern.ch - +90 533 512 11 93.

Prof. Dr. Yasar ONEL, Physics and Astronomy Department, **IOWA UNIVERSITY**, Iowa, USA
yonel@newton.physics.uiowa.edu

Dr. Mikko Antero Voutilainen, Physics Department, **HELSINKI UNIVERSITY**, Helsinki, Finland.
Mikko.Voutilainen@cern.ch